RRS James Cook JC132

Cruise Report

The Role and Extent of Detachment Faulting at Slow-Spreading Mid-Ocean Ridges

Leg 3

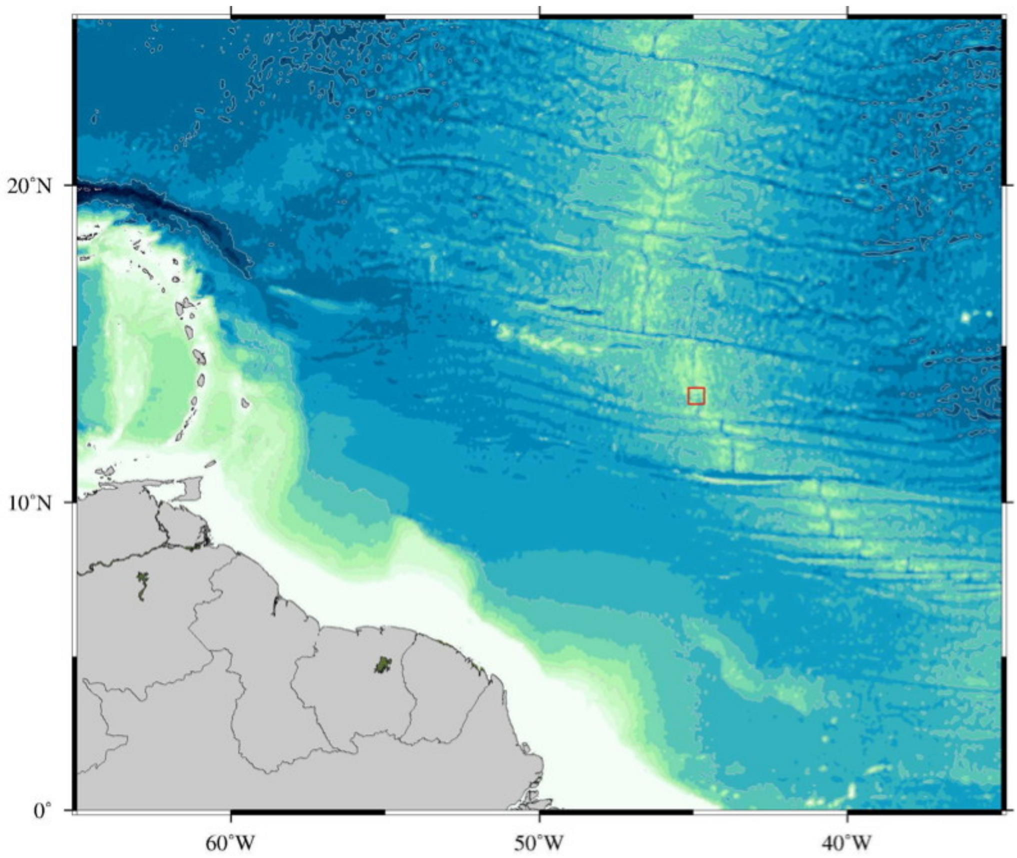

14th January – 24th February 2016

Mindelo (Cape Verde) - Port of Spain (Trinidad)

RRS James Cook JC132

Cruise Report

The Role and Extent of Detachment Faulting at Slow-Spreading Mid-Ocean Ridges

Leg 3

14th January – 24th February 2016
Mindelo (Cape Verde) - Port of Spain (Trinidad)

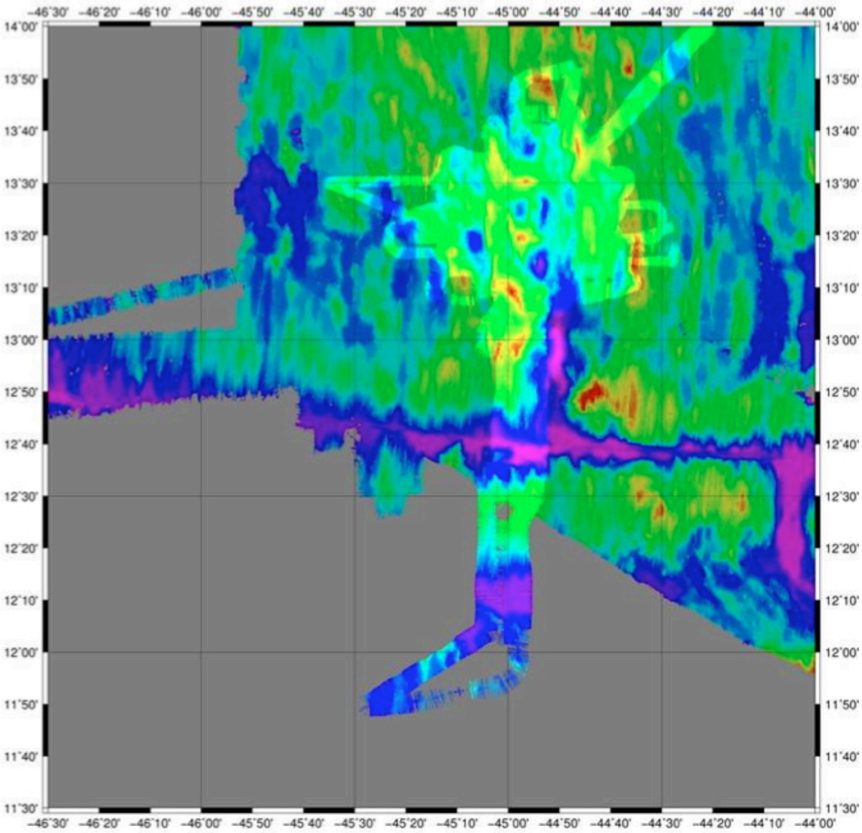

Prof Tim Reston
School of Geography, Earth and Environmental Sciences,
University of Birmingham
Birmingham, B11 2TT
t.j.reston@bham.ac.uk

Prof Christine Peirce
Department of Earth Sciences
University of Durham
South Road
Durham, DH1 3LE
christine.peirce@durham.ac.uk

February 2016

Table of Contents

Summary

The primary objective of *RRS James Cook* cruise JC132 was to acquire the active-source geophysical data and seafloor imagery to complement the passive recordings of microseisms made by 25 ocean-bottom seismographs (OBS), deployed at the 13°20'N oceanic core complex on the Mid-Atlantic Ridge during JC102 and recovered during JC109.

Five main data types were collected during JC132: wide-angle recordings of airgun shots by up to 58 OBSs; multichannel seismic (MCS) reflection data acquired using a 3 km streamer and airgun sources; near-seabed and towed magnetic data; seafloor imagery acquired using both Autosub and a hull-mounted swath system; and gravity data. The gravity data were tied to absolute base stations in Southampton and Mindelo, and a new absolute base station in Port of Spain, established as part of this project. The swath bathymetry data were calibrated against a sound velocity dip undertaken at the lateral centre of the ocean-bottom seismograph grid, and co-located with the sound velocity dip calibrations undertaken as part of JC102 and JC109.

Although both Autosub and the seismic airgun array source did not perform to specification throughout the cruise, the near-seabed bathymetry and magnetic data, and wide-angle refraction and normal incidence reflection multichannel seismic data acquired are usable to address the scientific objectives. As part of the OBS deployments, three new broadband sensor systems were also successfully tested, together with the NERC Ocean-Bottom Instrument Facility's new generation data-logger.

1. Background and scientific objectives

1.1 Background

Since the discovery of domal corrugated surfaces at slow-spreading mid-ocean ridges (Cann et al., 1997), our understanding of how seafloor spreading works has radically changed. These domal surfaces, termed oceanic core complexes, were believed to be the unroofed plutonic and partially serpentinized mantle footwalls of large-offset normal 'detachment' faults; structures apparently responsible for accommodating much of the plate separation. These detachment faults are believed to cross-cut the entire crust, exhuming in their footwalls first a crustal section (typically a non-corrugated blocky massif) and then, in the domal oceanic core complex (OCC - Fig. 1), mantle rocks intruded by plutonic gabbros (Tucholke and Lin, 1994; Cann et al., 1997; Tucholke et al., 1998). The OCC is commonly striated and corrugated in the spreading direction (Fig. 1) and interpreted to be a slip surface, exhumed from beneath median valley basalts.

Many aspects of this newly recognised mode of seafloor spreading remain unproven or controversial. For example, although it is likely that the corrugated upper surfaces of OCCs represent the exposure of steeply dipping detachments rooting at depth beneath the median valley, the link has not been clearly proven, though it is supported to some extent by palaeomagnetic studies (Morris et al., 2009; MacLeod et al., 2011) that show significant footwall rotation.

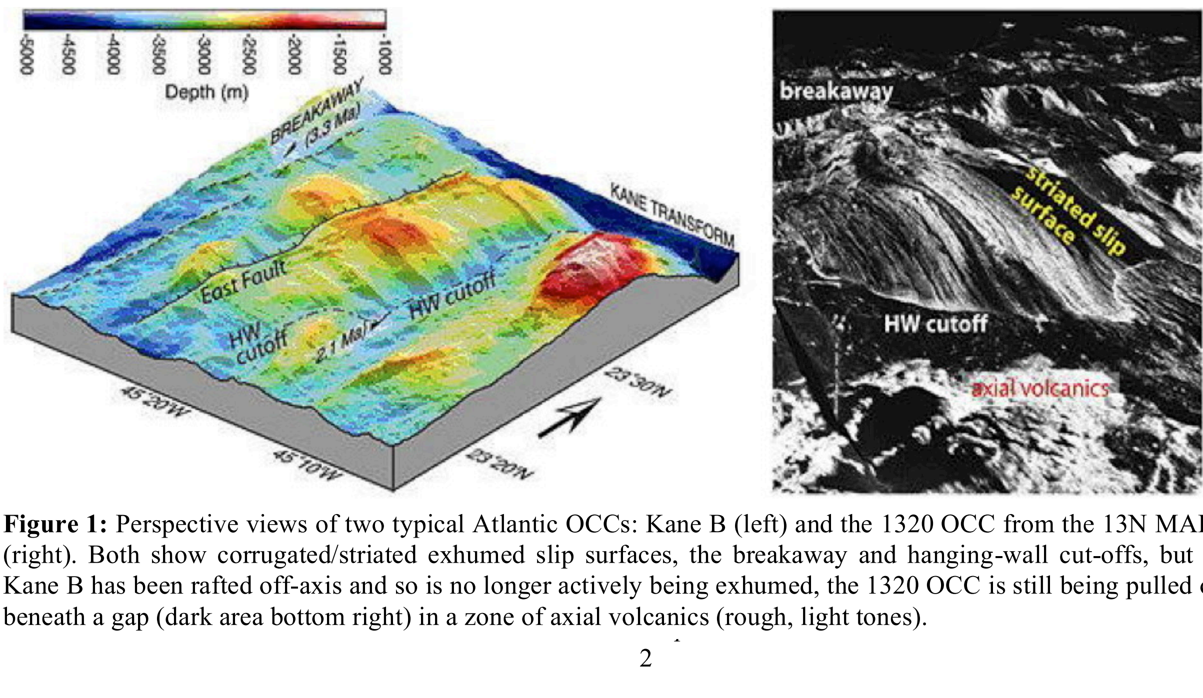

Figure 1: Perspective views of two typical Atlantic OCCs: Kane B (left) and the 1320 OCC from the 13N MAR region (right). Both show corrugated/striated exhumed slip surfaces, the breakaway and hanging-wall cut-offs, but whereas Kane B has been rafted off-axis and so is no longer actively being exhumed, the 1320 OCC is still being pulled out from beneath a gap (dark area bottom right) in a zone of axial volcanics (rough, light tones).

The only in situ evidence to date is based on P-wave travel-time tomographic inversion of two 2D wide-angle seismic profiles and passive micro-seismicity monitoring near the TAG hydrothermal field (Fig. 2 - deMartin et al., 2007). There, a steeply dipping band of hypocentres is inferred to mark a fault that flattens abruptly upwards to follow an unconnected, shallower, gently-dipping boundary between two velocity anomalies, one of which, reflecting a region of higher relative velocity, is located in the footwall. However, the TAG data does not directly image the detachment rollover, does not prove the continuity between steep and shallow zones, and does not show the lateral extent of the detachment.

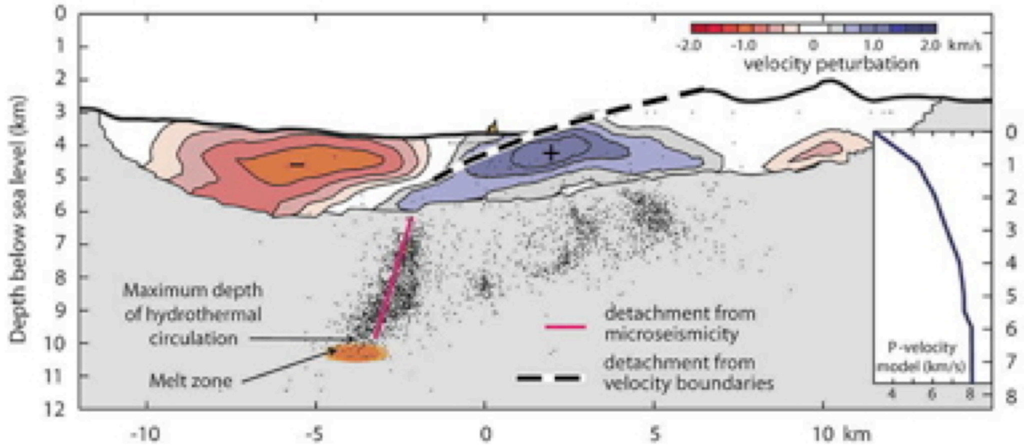

Figure 2: Section through the TAG area (deMartin et al., 2007), showing a possible detachment partly defined as a velocity boundary and partly as a zone of dipping micro-seismicity.

Escartín et al. (2008) and Reston & Ranero (2011) see oceanic detachment faults as essentially continuous, long-lasting features active on a segment scale (Fig. 3). Here, OCCs are simply places where a mega-detachment breaks surface, being covered in the intervening regions by thin-skinned rider blocks of volcanic seafloor. If so, as much as 50% of Mid-Atlantic Ridge (MAR) crust may be the result of asymmetric detachment faulting; it has even been suggested that mantle-derived material may dominate huge swathes of Atlantic ocean floor, potentially forming 20-25% of all seafloor produced at spreading rates <40mm/yr (Cannat et al., 2010).

Alternatively, MacLeod et al. (2009) see OCCs as spatially restricted, ephemeral features that are switched on and off by variations in local magma supply (Fig. 4). In this model OCC detachments are ordinary valley wall faults on which slip continues as a result of the progressive waning of magma supply to below half that needed to generate a continuous igneous crustal layer. Strain localisation would result in progressively more asymmetric plate separation, until more than half is partitioned onto the detachment itself.

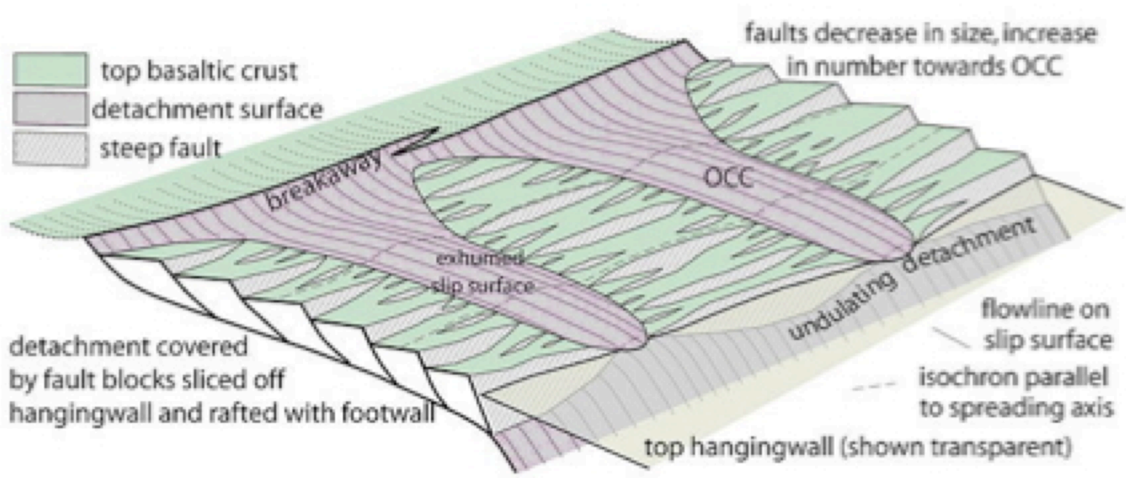

Figure 3: Perspective view of the segment scale detachment model: the detachment continues laterally beneath small fault blocks between adjacent OCCs, which represent the places where the detachment breaks the surface. In the alternative model, adjacent OCCs are unconnected.

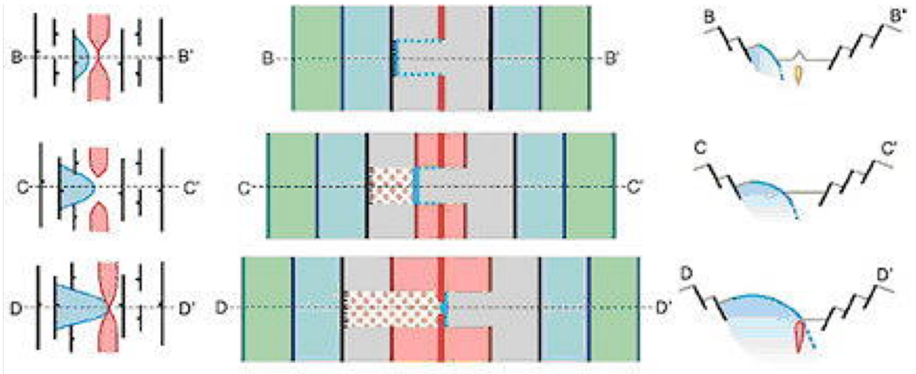

Figure 4: MacLeod et al. (2009) model for OCC formation: strain weakening concentrates deformation onto a single fault which accommodates more than half the total spreading, and so migrates toward and over the spreading axis, to be cut by renewed magmatism. Left: structural map; Middle: magnetic lineations; Right: schematic sections.

As this strain localisation occurs, the detachment migrates towards and across the axial valley, such that renewed magmatism is intruded into the detachment footwall and ultimately overwhelms it. Spreading becomes strongly asymmetric between a localised OCC and its immediate conjugate, but not across the whole of a spreading segment. The lateral change in spreading asymmetry and the limited dimensions of the detachment fault in this model require spatially restricted transfer zones (dominated by magmatism and ductile shear at depth and faulting near surface) to accommodate the along-strike variations in strain distribution.

There are, therefore, two conflicting hypotheses:

1) detachments continue laterally between OCCs which are linked (Reston and Ranero, 2011);

and

2) detachments are temporally and spatially restricted and not linked (MacLeod et al., 2009).

The two conflicting hypotheses (**1. linked vs. 2. restricted**) make testable predictions:

1a: Detachments continue in the sub-surface between OCCs and so control divergence at a whole spreading segment for extensive periods of time;
1b: Asymmetric spreading affects the whole segment, not just OCCs and their conjugates;
1c: By controlling spreading of an entire segment, the detachment drives mantle upwelling and location of the spreading axis;

2a: Detachments are restricted to individual OCCs and are thus localised in time and space;
2b: OCCs produce spatially restricted spreading asymmetry that does not extend segment-wide; strain is transferred laterally by magma injection and brittle deformation;
2c: Gabbros are only incorporated into the footwall late as it migrates across the median valley.

The 13N MAR project aims to test the above hypotheses by determining:

(a) the sub-surface geometry of detachment faults at active OCCs, and how this changes in extent both along- and across-strike beneath adjoining volcanic-dominated seafloor;
(b) the local degree of asymmetry of plate separation adjacent to an OCC compared to the adjoining volcanic seafloor; and
(c) the amount and distribution of melt delivered to both hanging wall and footwall at an active OCC in comparison to that in the adjoining volcanic seafloor region.

The required data from an actively forming OCC did not exist, and we have now collected them during three cruises to the MAR between ~13°15' and 13°35'N – namely JC102, JC109 and JC132. This report describes the third and final of these cruises – the acquisition of active source seismic data, both reflection (MCS) and wide-angle (OBS), as well as the collection of near seafloor magnetics and seafloor imagery.

1.2 The study location - 13°N

An extensive region of OCCs exists at 13°N on the MAR, and includes one located at 13°20'N (henceforth known as 1320) that is actively developing and another at 13°30'N (1330) that may recently have become inactive, making this region the ideal target for this study. These OCCs have already been surveyed with shipboard multi-beam swath bathymetry (Smith et al., 2008), imaged with TOBI near-bottom side-scan sonar and sampled with dredges and a seabed rock drill (Searle et al., 2007; MacLeod et al., 2009; Mallows, 2011; Mallows and Searle, 2012).

Apart from the wealth of existing data, 13°N is the ideal location for this study because:

- unlike other fully-developed OCCs both 1320 and 1330 can be traced directly to the spreading axis, implying that both are either currently or very recently active;
- the typical, high reflectivity, untectonised hummocky terrain of the MAR neovolcanic zone (NVZ) is absent opposite 1320 and 1330 (Fig. 1), and is replaced by lower reflectivity terrain (suggesting older volcanics with several metres of sediment cover), often displaying small-scale faulting. This, and a concomitant increase in tectonic strain, is interpreted as evidence that the melt supply is reduced near the regions of active detachment faulting (MacLeod et al., 2009);
- the NVZs north and south of 1320 taper toward it, suggesting they are propagating towards this magmatic gap and may ultimately "switch off" the detachment faulting, as appears to have been the case for the off-axis OCC at 13°48'N; and finally and crucially
- the presence of two active OCCs that developed at similar times and which remain active implies either that the controlling detachment continues under the intervening basin or that the basin is a zone of magmatic soft linkage between two spatially limited detachment systems.

1.3 Scientific objectives

The primary objectives of this project are to test the different and contrasting hypotheses for the spatial and temporal evolution of OCCs. Using the geophysical data acquired during all three cruises (JC102, JC109 and JC132), we will determine:

1) the geometry of the detachments that have unroofed the 1320 and 1330 OCCs, (i) through direct imaging of the detachment surface with multichannel seismic (MCS) reflection data, and (ii) by imaging with ocean-bottom seismograph (OBS) wide-angle (WA) data any intra-crustal layering (refracting interfaces) and regions of mantle-derived material and melt accumulation (relative velocity anomalies), in both cases from the seabed down to sub-Moho, and (iii) from the distribution of seismicity down to the base of the brittle lithosphere, probably 7-8 km sub-seafloor (testing **Hypotheses 1a, 1c, 2a, 2c**);
2) the lateral extent of the 1320 and 1330 detachments, through a combination of direct (MCS reflection) and indirect (WA velocity structure) imaging, and distribution of seismicity (testing **Hypotheses 1a, 2a**);
3) the detailed spreading history and thus any along-segment variation in the asymmetry of spreading, through high-resolution Autosub magnetic imaging (testing **Hypotheses 1b, 2b**);
4) the detailed internal structure of the footwall of the detachment, both at the spreading axis and at an OCC, through a combined approach of 3D seismic velocity tomography and magnetic field inversion (testing **Hypothesis 1c, 2c**); and
5) the detailed structure of the OCC domes and the inferred exhumed Moho, and tectonic linkages between them using high-resolution bathymetry data simultaneously with magnetic field measurements. We will also determine locations of fluid outflow (fault scarps, hydrothermal systems and exposures on the corrugated surface – Connelly et al., 2011) and future sampling sites from the nephelometer, CTD, Eh and ADCP data collected contemporaneously with the high resolution bathymetry and magnetic data. These data will also constrain the precise geometry and extent of the hydrothermal discharge inferred at the toe of 1320 from the massive sulphides recovered there on JC007 (Searle et al., 2007), and thus inform our understanding of the thermal structure of the OCC and likely implications for controls on the larger-scale rheology.

Legs 1 and 2, JC102 and JC109, deployed and recovered an array of OBSs that recorded micro-seismicity for 6 months in the region of the 1320 OCC (Fig. 5) and its possible continuation to the north towards the 1330 OCC. The final cruise (Leg 3 - JC132) described here, aimed to complete the data acquisition with active-source MCS and WA seismic acquisition and Autosub 6000 surveying.

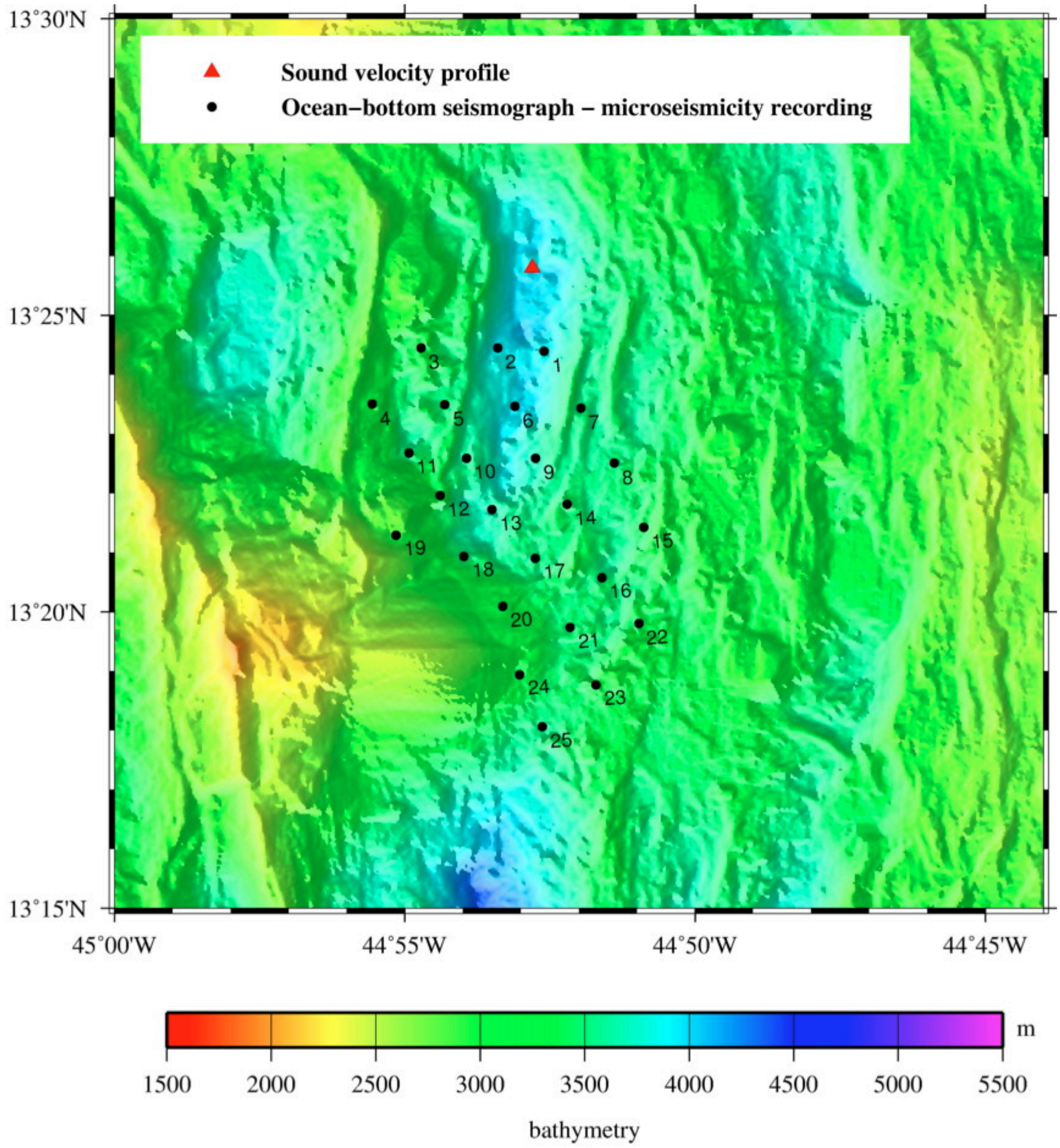

Figure 5: JC102 OBS deployment locations for passive micro-seismicity recording. All OBS were equipped with a three-component 4.5 Hz, gimballed geophone pack. OBSs 1, 3, 5, 7, 12, 14, 15, 17, 20 & 23 were equipped with differential pressure gauges. The remaining OBSs were equipped with a hydrophone. All instruments were successfully recovered during JC109.

The JC102 passive deployment followed the approach adopted by Project Partner Sohn at the TAG area (deMartin et al. 2007). Twenty-five OBSs were deployed in a tight network centred on the most ridge-ward limit of the 1320 OCC and extending to the north (Fig. 5). The deployment locations were concentrated over the northern half of the 1320 detachment, close to its hanging wall cut-off (where the detachment passes beneath the seafloor) and continue to the north approximately halfway towards the 1330 OCC, to map out the postulated lateral continuation of the master detachment between OCCs. Given the known amount of teleseismic activity from the study area, we estimated that ~50 locatable earthquakes would take place every day. By recording for 6 months, we expected to record ~9000 earthquakes and we expected these to be representative of the active faulting in the region. Preliminary indications are that close to 300,000 microseisms were recorded by all 25 OBSs each, with more events recorded by fewer instruments, which are in the process of being located within the study area. This same area was the focus of the active-source seismic and Autosub investigations during JC132.

2. Cruise preparation and mobilisation

2.1 Scientific plan

The port call at the start of the cruise was Mindelo (Cape Verde), which was ~5 days from the work area at a transit speed of 10 kn. The science programme was scheduled to last 32 days. The end of cruise port call was Port of Spain (Trinidad), about 4.5 days transit from the work area. The entire cruise was, thus, 42 days port-to-port. The framework waypoints for the cruise can be found in Appendix 1.

The plan was to transit from Mindelo to the work area, testing various pieces of equipment on the way (acoustic releases, Autosub), and on reaching the work area to interleave Autosub missions with OBS deployments, shoot the wide-angle survey to provide a velocity-depth crustal structure model in the region of the 1320 and 1330 OCCs, redeploy several OBSs in the vicinity of the 1320 OCC, again interleaved with Autosub missions, then deploy the streamer and acquire the MCS crustal image. On completion of that, OBS recoveries interleaved with further Autosub missions would complete the work programme. The cruise followed this general outline of activities.

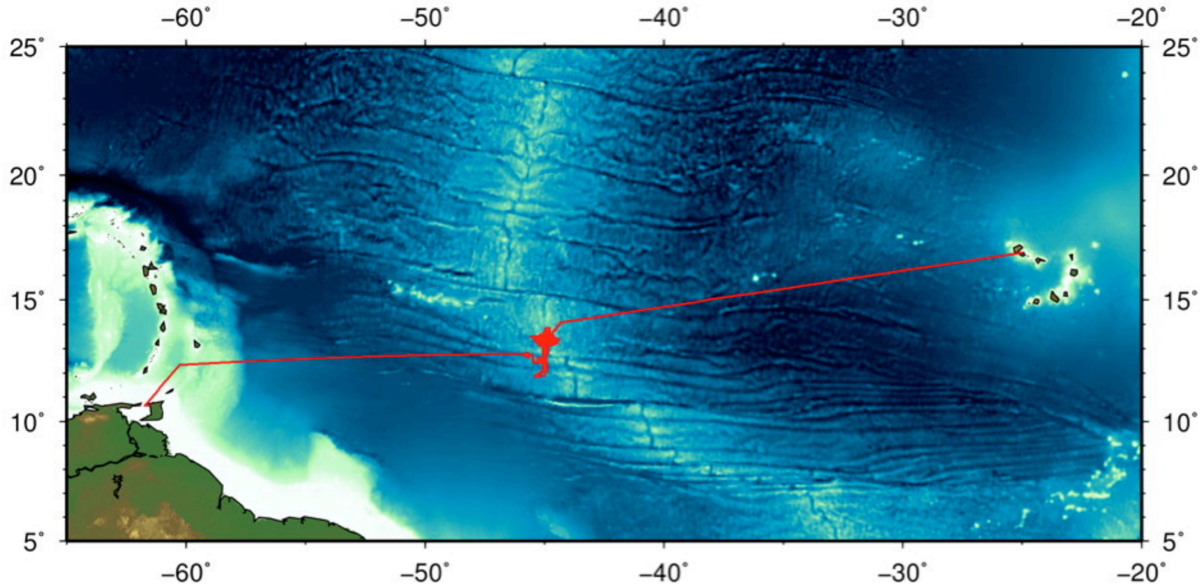

Figure 6: Transits to and from the work area.

2.2 Territorial waters and diplomatic clearances

Although the work area for this cruise lies entirely in international waters (Fig. 6), we planned to run the gravimeter and swath bathymetry acquisition port-to-port to enable start and end of cruise absolute base station ties for the gravity data acquired during this cruise and that for JC102 and JC109 as well. Consequently, diplomatic clearances from the Cape Verde and Trinidad & Tobago were required. The region between 200 nm and 350 nm to the east of Trinidad is also in dispute between Guyana, Suriname and Barbados and so clearances for these nations' waters were also sought to enable transit to port via any route.

The port calls for this cruise were selected by NERC Marine Planning, and in the case of Port of Spain in Trinidad, in the knowledge that there was no extant absolute gravity base station. Consequently the diplomatic clearance request also required seeking permission to re-establish such a station using a meter sourced by the PIs from the NERC's Space Geodesy Facility. In the cases of the Cape Verde, Guyana, Suriname and Barbados diplomatic clearances were received without issue or query from the nation state. However, despite completion of the paperwork to enable the clearance application to be submitted at least six months prior to arrival at the 200 nm limit of Trinidad & Tobago, and despite on-going and repeated communications via the Foreign and Commonwealth Office with the Ministry of Foreign Affairs of the Trinidad & Tobago Government, and repeated chasing for clearance in the days preceding arrival, permission was only granted on February 23rd, the day of planned entry into Trinidadian waters.

2.3 Mobilisation

All of the scientific party equipment was handled by the NERC Ocean-Bottom Instrumentation Facility (OBIF), accumulating all of the scientists' personal luggage at their lab in Durham and arranging its freight to Southampton where this, and all of the OBS-related equipment were loaded onto the *RRS James Cook* during the week of the 14th December, and the OBS lab areas set-up. All freight and customs export was handled by OBIF's shipping agent and preceded without issue. All of the NMEP-provided equipment was also mobilised in Southampton during the week of the 14th December to facilitate a seismic trials cruise (JC131) during the vessel's transit from the UK to the Cape Verde.

3. Work conducted and data collected

Fig. 7 shows the track chart from the point of arrival to point of departure from the work area, together with the route taken by the *RRS James Cook* from Southampton departure, throughout the trials cruise (JC131) to arrival in Mindelo, and from the JC132 work area to Port of Spain at the end of the cruise.

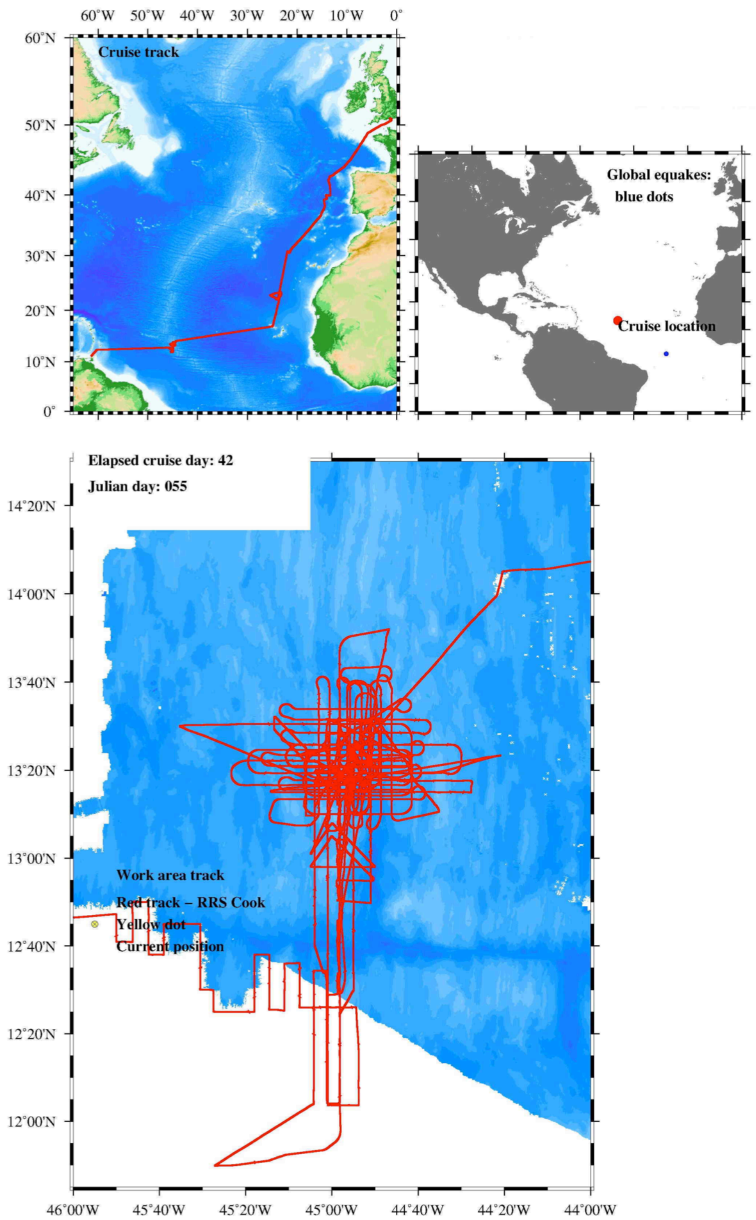

Figure 7: JC132 track chart with inset showing the entire track from departure from Southampton (UK) prior to the JC131 trials cruise to arrival in Port of Spain (Trinidad).

3.1 Wide-angle seismic acquisition

All seismic operations followed JNCC guidelines regarding marine mammals and other marine species considered species of concern, and in compliance with the recommendations made in the environmental impact assessment that reviewed all cruise-related activities. A team of JNCC-certified marine mammal observers undertook the observation process prior to any seismic operation, and documented that process according to the JNCC requirements. These observers also documented any marine mammal sightings regardless of on-going activities.

The OBS data acquisition comprised two main activities: a) the planned grid survey (Fig. 8); and b) an additional long transect (Profile R) making best use of remaining ship time. JC132 also provided an opportunity for the NERC's Ocean-Bottom Instrument Facility to undertake testing of: i) the prototype versions of its in-development broadband passive sensors and gimballing systems; and ii) the production roll-out version of its new generation data-logger.

For the main JC132 active-source seismic acquisition each OBS was set-up to record at 250 Hz sampling rate on each of four data channels, namely three-component (X, Y, Z) geophone and hydrophone (e.g. Fig. 9). OBS deployment locations are included in Appendix 2 and profile details in Appendix 3. Shots were fired every 60 s, which at a survey speed of 4.9 kn, results in a shot spacing of 150 m.

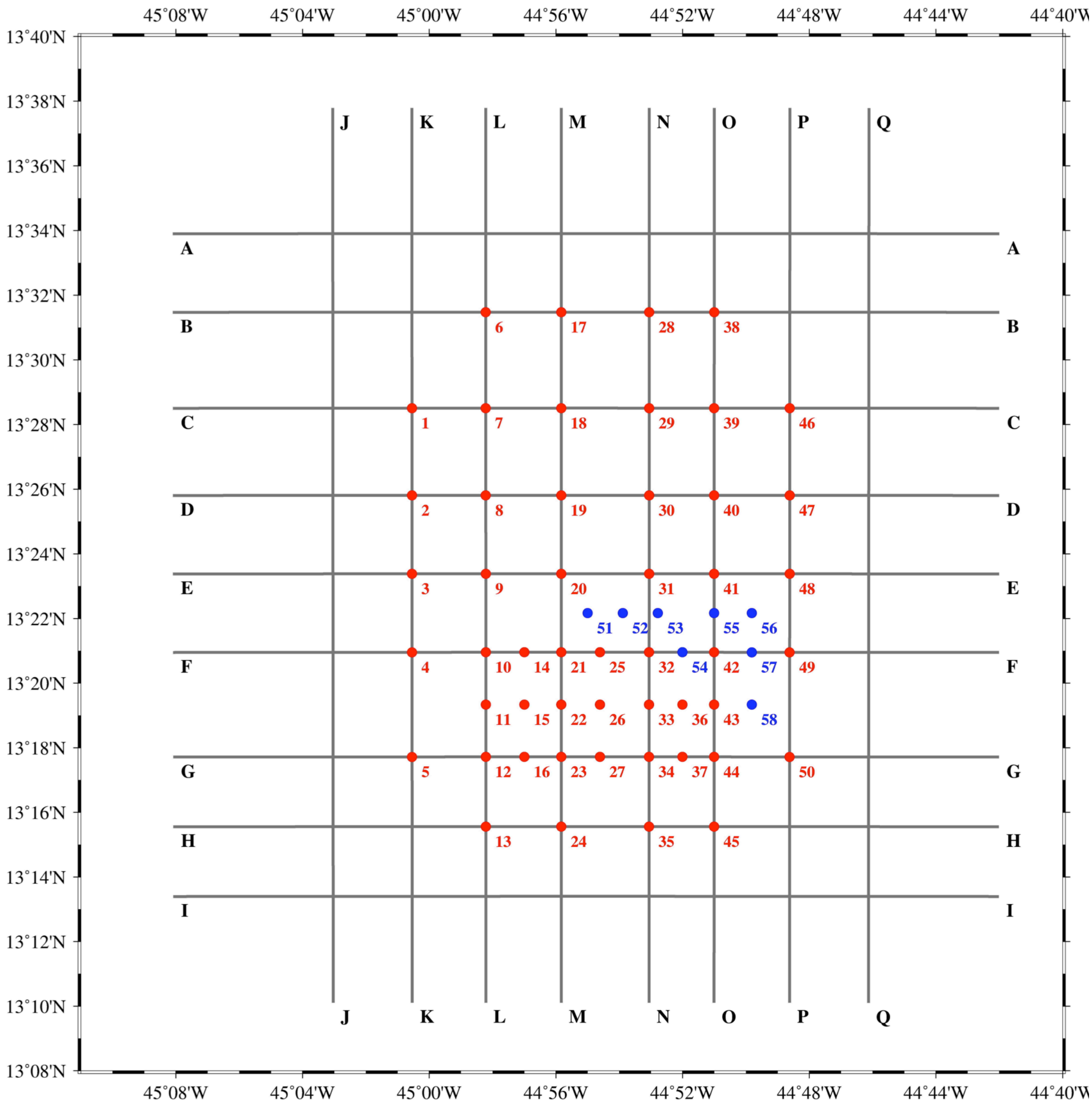

Figure 8: Planned wide-angle grid of profiles. The red dots show OBSs deployed for the wide-angle shooting and blue dots eight further OBSs deployed for the MCS shooting. These eight OBSs were originally test platforms deployed shortly after arrival in the work area which, when recovered and proven, were used to supplement the grid during MCS surveying.

Figure 9: Range of 58 ocean-bottom seismographs deployed during JC132. Top: standard platforms amassed in the water bottle annex ready for deployment. Left middle: standard OBS ready to be deployed over the starboard side. Right middle: broadband test platform variant ready for deployment. Bottom: the last deployment of the cruise.

3.1.1 Grid survey

For JC132 a grid of wide-angle seismic profiles were planned, comprising nine east-west and nine north-south running transects as shown in Fig. 8. These profiles were supplemented by an additional diagonal profile (Profile X) running from the west side of the grid towards the east end of Profile A; a consequence of the timing during the day of and time taken to deploy the airgun array versus daylight hours versus time of day of first shot (to keep to JNCC guidelines).

Within the towing restrictions of the approach adopted, and the PIs' experience of larger airgun failure during past surveys, a medium-sized array was designed to be symmetrical and provide the same source characteristics, although at lower power, even if one entire side were lost during shooting and unable to be repaired until daylight (to keep to JNCC guidelines). The 4800 in^3 volume array is shown in Fig. 10 and includes a 500 in^3 airgun towed as a single on a wire from the stern A-frame gantry to increase the array volume for deep crustal imaging.

Even factoring in the likely loss of the largest airguns in the array and already modifying the design from ideal to minimise likely time lost due to airgun failure and repair, multiple failures of the 500 in^3, 400 $in^3$and 300 in^3 airguns in the array occurred, mostly coming out of starboard turns and at night. Adherence to JNCC regulations meant that repairs/restarts could only be done at first light and so significant portions of, and in a number of instances entire profiles, were acquired with a source array not as specified.

In addition, depth sensors mounted on the individual sub-array towing beams showed that the front of each beam towed ~2 m shallower than the rear for the entire survey. In this respect, none of the seismic profiles were acquired according to specification.

Shot hydrophones were also mounted on each sub-array beam for the entirety of the JC132 airgun shooting (both WA and MCS). The output of these hydrophones were input into the auxiliary channels of the MCS acquisition system and recorded during both the WA and MCS shooting. In the case of the WA shooting, this recording was to determine the nature of the outward propagating source signature to be used during data processing and also as a calibration check on the as-designed source signature modelled prior to the cruise.

However, during MCS shooting (see Section 3.2) a number of profiles were shot using a flip-flop approach where each half of the airgun array was fired alternately. A consequence of this mode of shooting and having a hydrophone attached to each sub-array beam, meant that the lateral location of each sub-array component could be measured and monitored, as a means of determining how the entire airgun array towed behind the vessel and towed laterally with respect to the multichannel streamer. A preliminary review undertaken during surveying indicated that the individual components in the array did not tow at the locations specified laterally behind the vessel. Again, this amounts to no data being acquired with an array as specified.

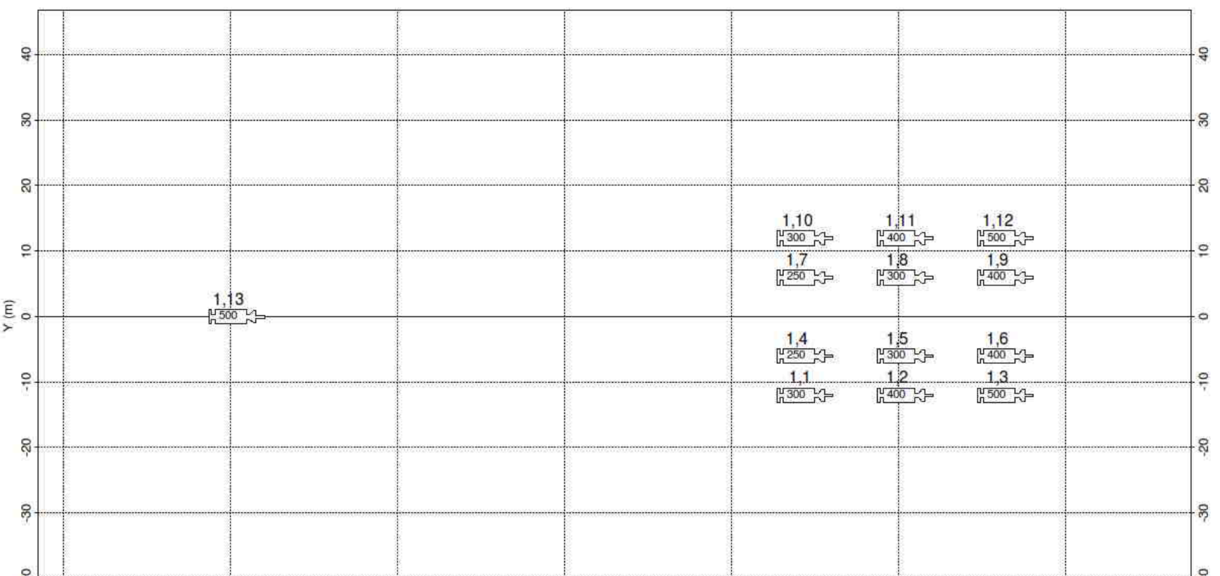

Figure 10: Planned airgun array used for wide-angle surveying. Specified tow depth 8 m.

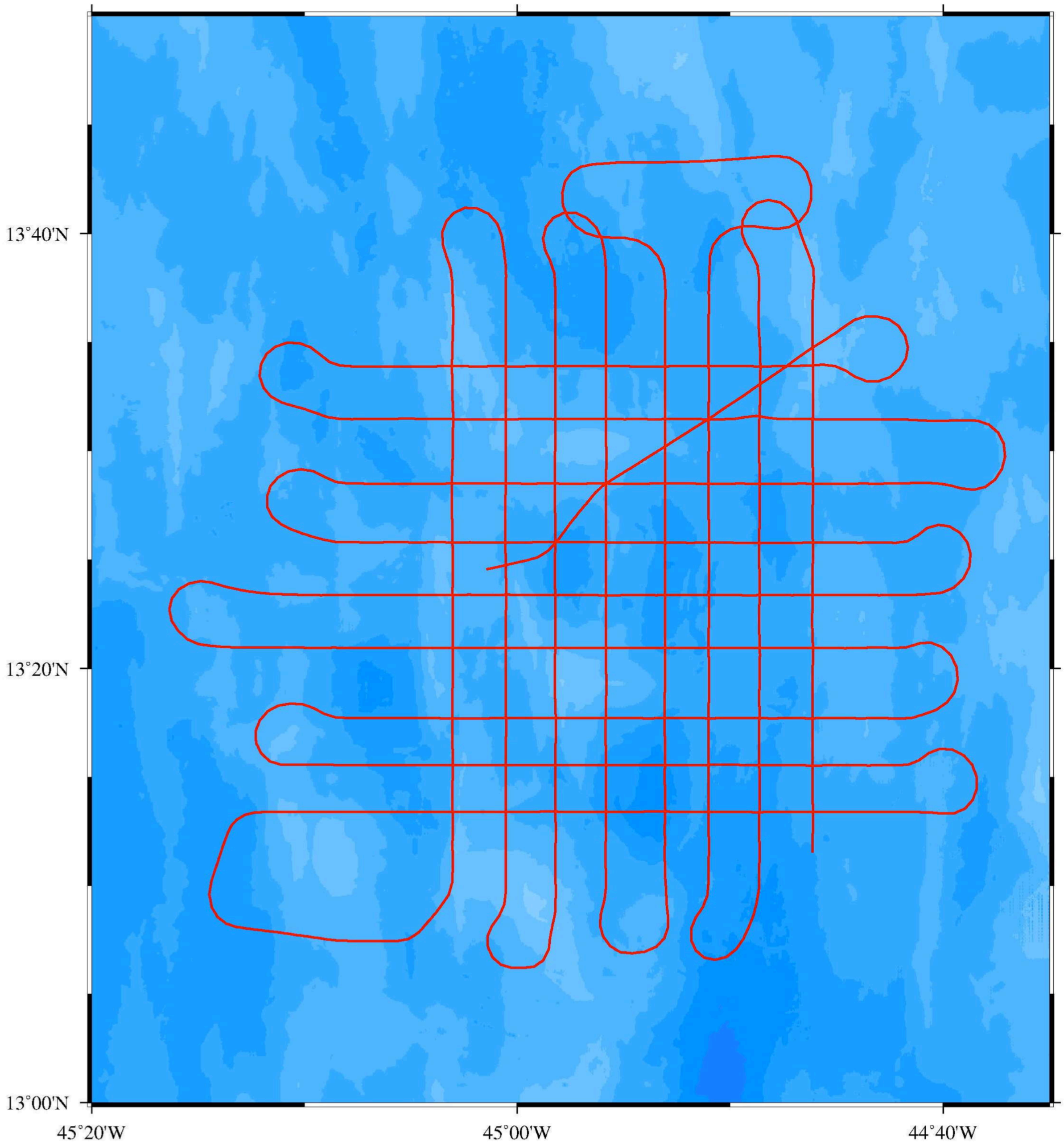

Figure 11: Acquired wide-angle grid of profiles, including the additional across-grid profile - Profile X – and the elongated turns associated with extended periods of airgun array repair. Although the profile spacing was greater than the minimum diameter 2°/min turn vessel criteria for airgun array towed turns, and possible in both the port and starboard directions given that no streamer was being towed during WA data acquisition, all turns resulted in part fish-tails.

A map showing the entire track line for the WA survey is shown in Fig. 11, and includes the periods of airgun array repair undertaken around turns, which were quite elongated in some instances to provide sufficient time to undertake the repairs. The waypoints for the start and end of each profile can be found in Appendix 3, together with the number of shots fired along each profile.

A comparison between the deployment and recovery locations of each OBS was made as recovery progressed, as a means of predicting where each OBS would surface and such that the vessel could be located a few hundred metres down wind for a speedy and efficient recovery. As Fig. 12 shows all of the OBSs drifted in approximately the same direction on deployment and recovery and were recovered some 200-400 m almost due west of their deployment location.

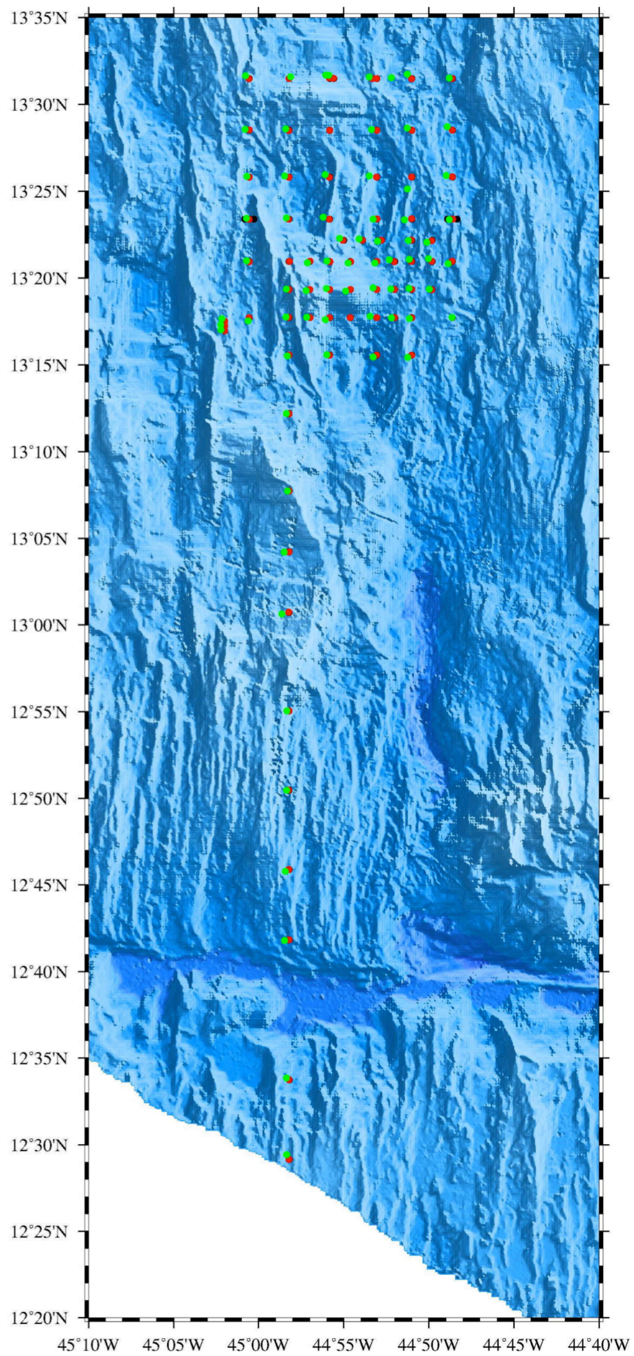

Figure 12: OBS planned (black dots) and actual (red dots) deployment and recovery (green dots) locations for the entire JC132 seismic survey.

A QC inspection of the data sections (e.g. Figs 13-14) on OBS recovery shows the work area to be quite asymmetrical in crustal velocity structure, not only across ridge, but also towards the north-west quadrant of the survey area, where significant signal attenuation is also observed.

Of the 58 OBSs deployed within the grid, all except four recorded all wide-angle and MCS shots on all channels, three had partial recordings and one was found, on recovery, to have exhausted its batteries very early on during deployment. The wide-angle data is of good quality with sub-seabed arrivals recorded out to offsets of up to 55 km on some instruments and 30-40 km on most instruments, sufficient to record upper mantle arrivals and thus map crustal thickness in 3D throughout the study area.

Inevitably, the consequences of multiple airgun failures can be readily observed in the data, as changes in signal amplitude and waveform characteristics. The inconsistent tow depth can also be readily observed in the frequency spectrum. Unfortunately, given the inconsistency in airgun array tow and airgun performance, determining which signal characteristics are a manifestation of the sub-seabed geology and which merely reflect seismic source output variation will be near impossible to resolve.

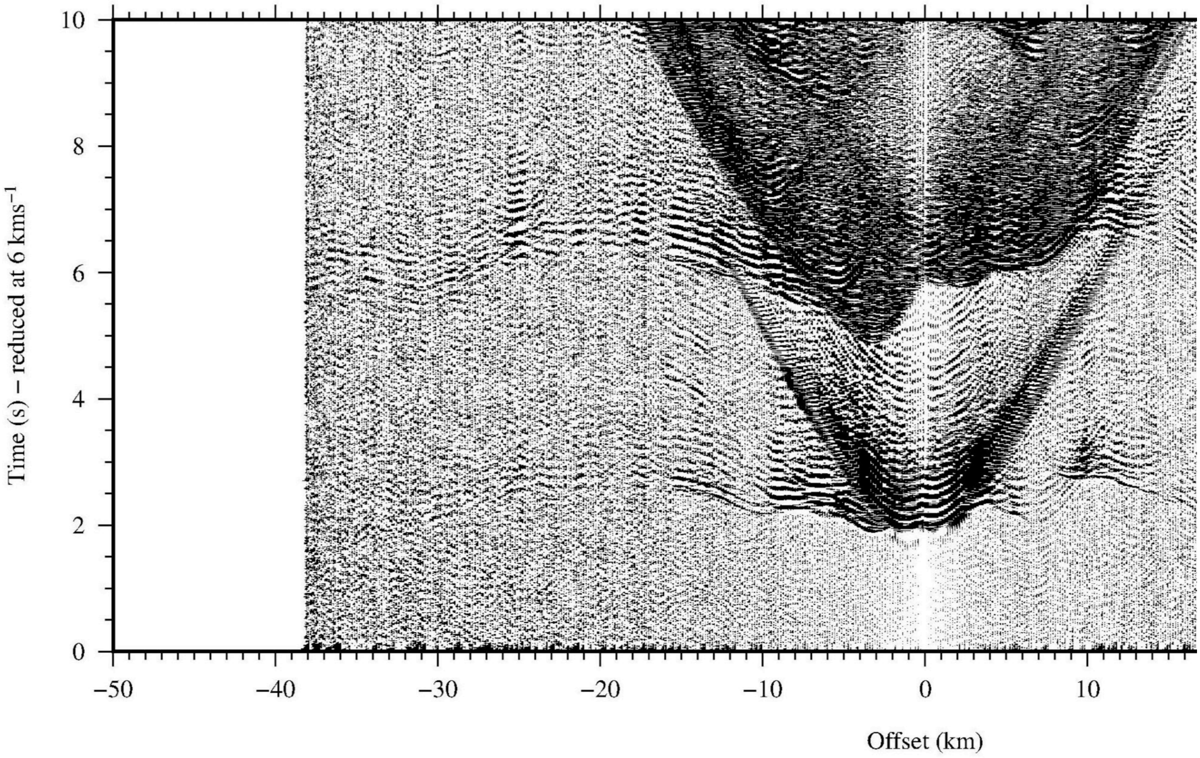

Figure 13: Hydrophone data from OBS 4 with shots fired along Profile F. The data have been band-pass filtered and are plotted reduced at 6 kms^{-1}.

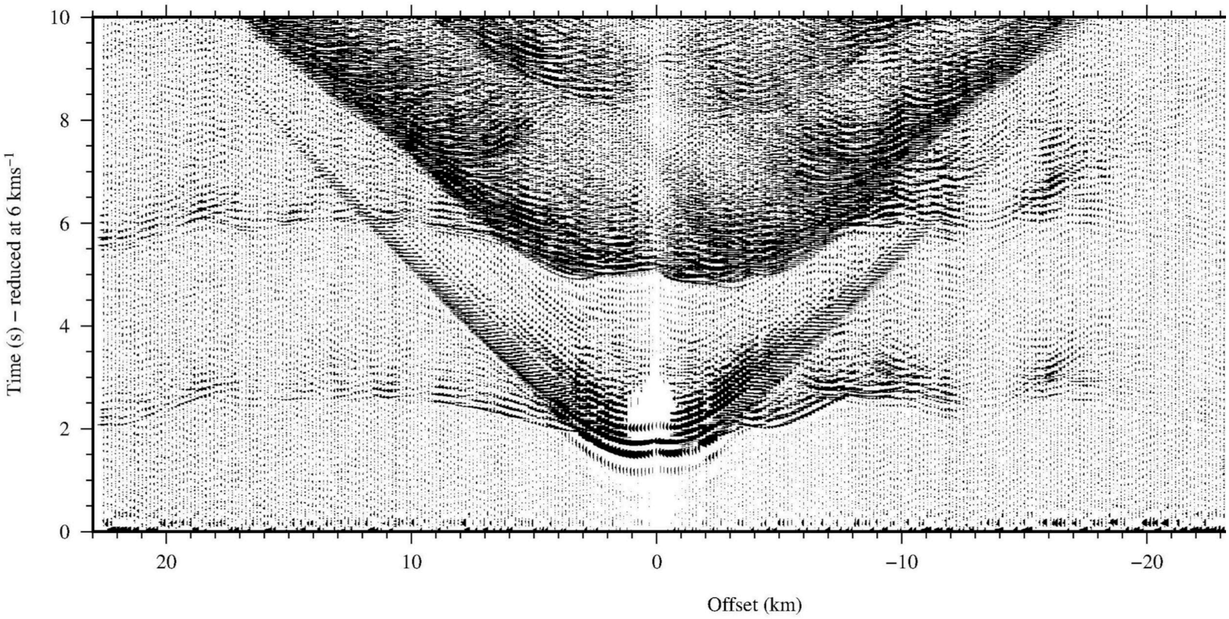

Figure 14: Hydrophone data from OBS 14 with shots fired along Profile F. The data have been band-pass filtered and are plotted reduced at 6 kms^{-1}.

3.1.2 Profile R

Profile R was shot as a supplementary profile using time gained from efficient and ahead of schedule OBS deployments and recoveries undertaken throughout the Grid survey. This profile was designed as a long offset OBS/MCS profile extending from the main work area around the 1320 OCC, south over the Ashadze Massif and the end-of-segment fracture zone to the south. Although 12 OBS deployments were initially planned, in the end only 10 OBSs were deployed in addition to the four remaining from the Grid survey due to time constraints, as shown in Fig. 15 – a total of 14 OBSs. Of these 14 OBSs, six were deployed with new generation data-loggers given the quality of data recorded by those deployed within the grid.

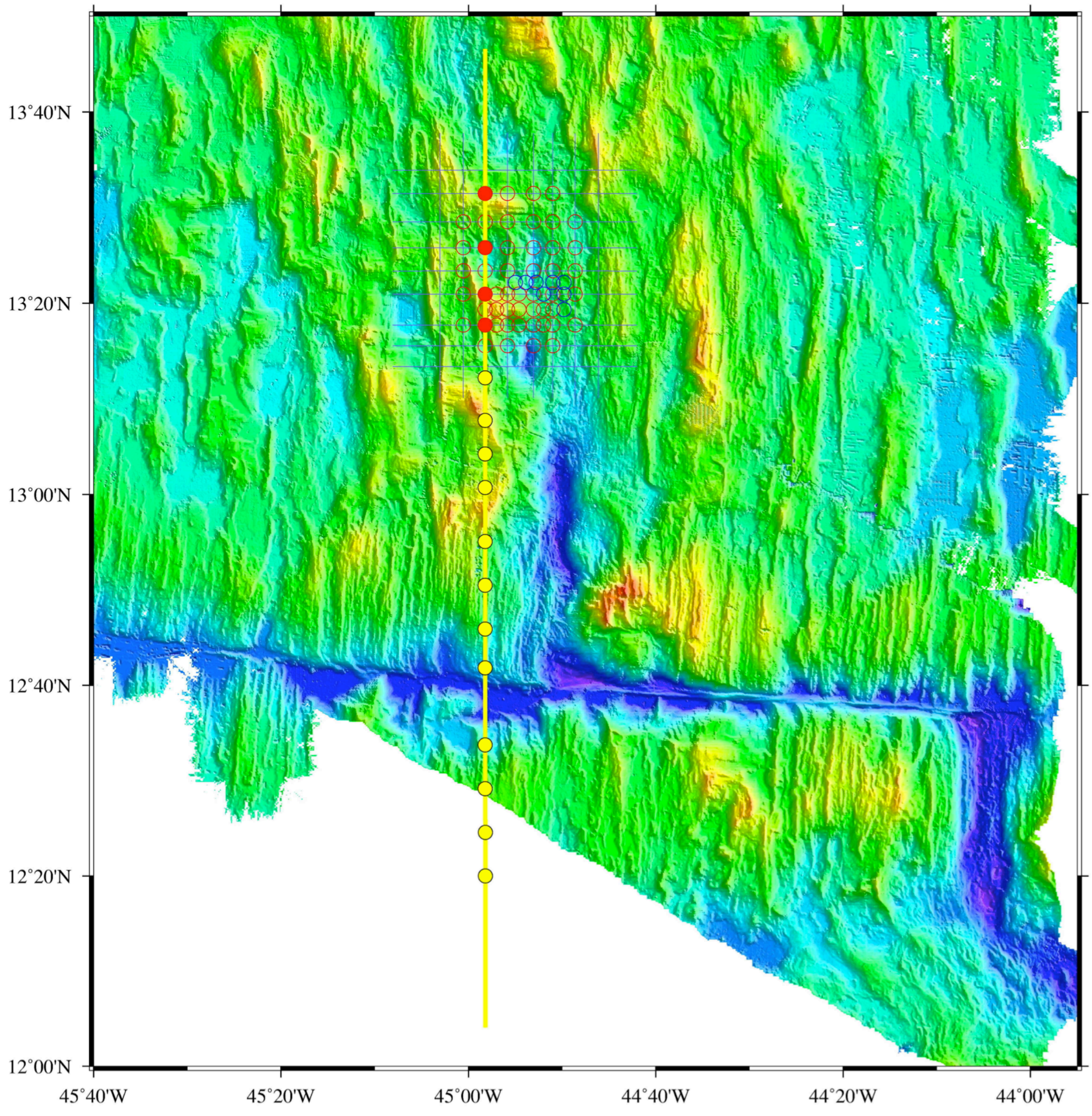

Figure 15: Profile R OBS locations (solid circles – red from the Grid survey; yellow this profile), and shot transect. Note the two most southerly of the planned OBSs (yellow dots) were not deployed due to time constraints.

All OBSs deployed along this transect recorded good quality data on all channels. All record sections are highly asymmetric as a consequence of the significant seabed topography along profile primarily. Water waves were recorded to in excess of 100 km and sub-seabed arrivals to >50 km, although highly attenuated. Example record sections from Profile R are shown in Figs 16-18.

The effect of airgun failure is particularly evident along Profile R when 30% of the array volume was lost in one instant when a hippo buoy beam float became detached from its sub-array beam during the hours of darkness about two-thirds of the way along the profile. Due to darkness and the consequences of the JNCC regulations, the rest of this profile had to be shot with only 70% of array volume.

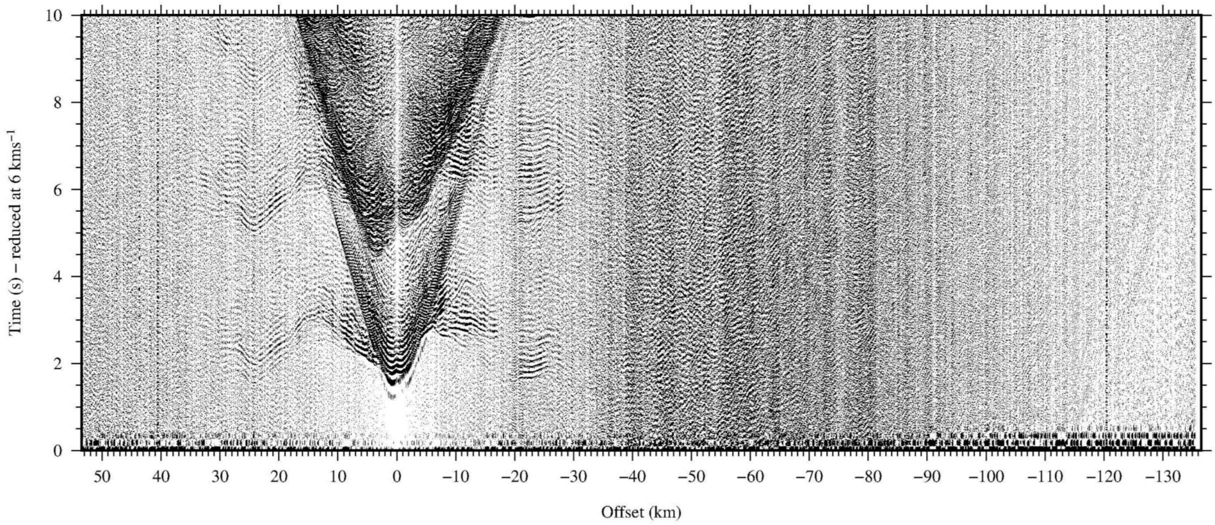

Figure 16: Hydrophone data from OBS 12 with shots fired along Profile R. The data are plotted reduced at 6 kms^{-1}.

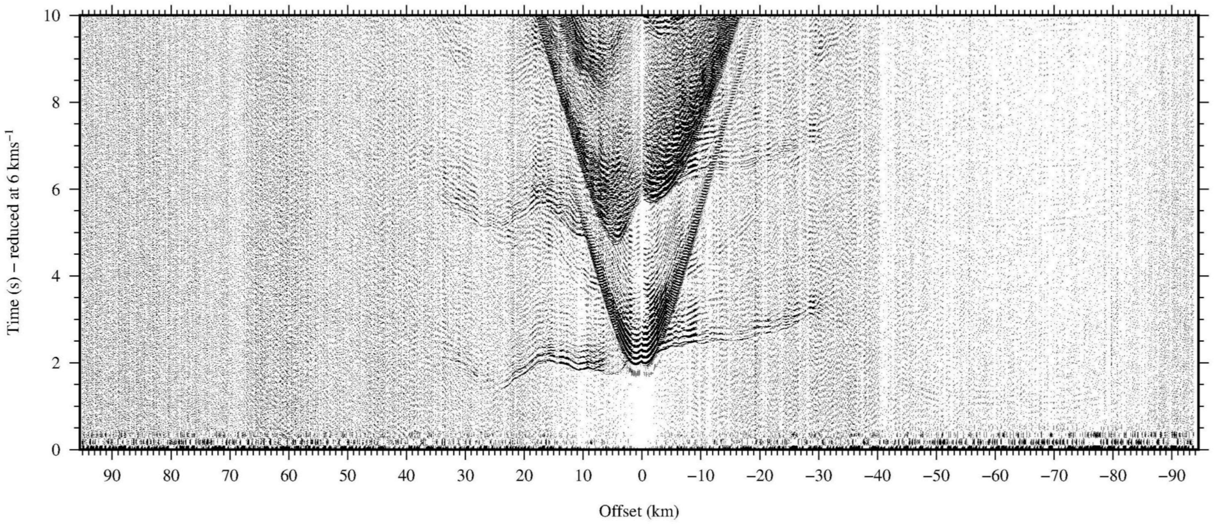

Figure 17: Hydrophone data from OBS 65 with shots fired along Profile R. The data are plotted reduced at 6 kms^{-1}.

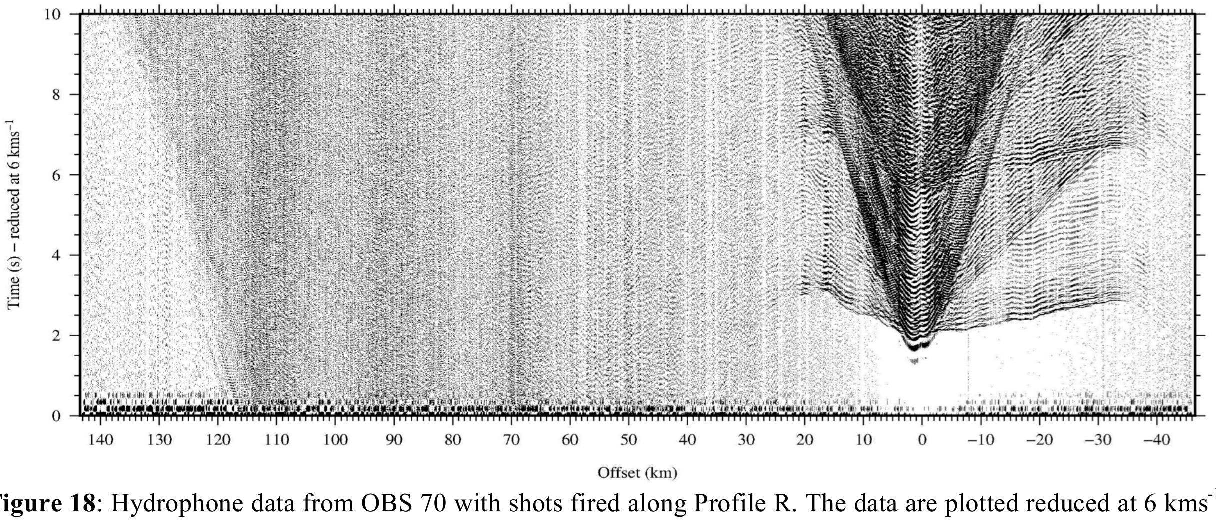

Figure 18: Hydrophone data from OBS 70 with shots fired along Profile R. The data are plotted reduced at 6 kms^{-1}. The consequence of losing 30% of the array volume is obvious in this record section.

3.1.3 Passive micro-seismicity

Although the primary goal of the JC132 cruise was to acquire active-source seismic data, there were periods of "seismic silence" when the OBSs were recording, but when the airgun array was either not being fired or not deployed. The passive data acquired during these periods were extracted from the active-source dataset and converted to MSEED format. These data will be included in the passive data analysis to add a wider footprint area to that study. A QC review of the data acquired during one of the test deployments (see Section 3.1.4) revealed a passive local microseismic event occurring approximately every minute (see Fig. 19).

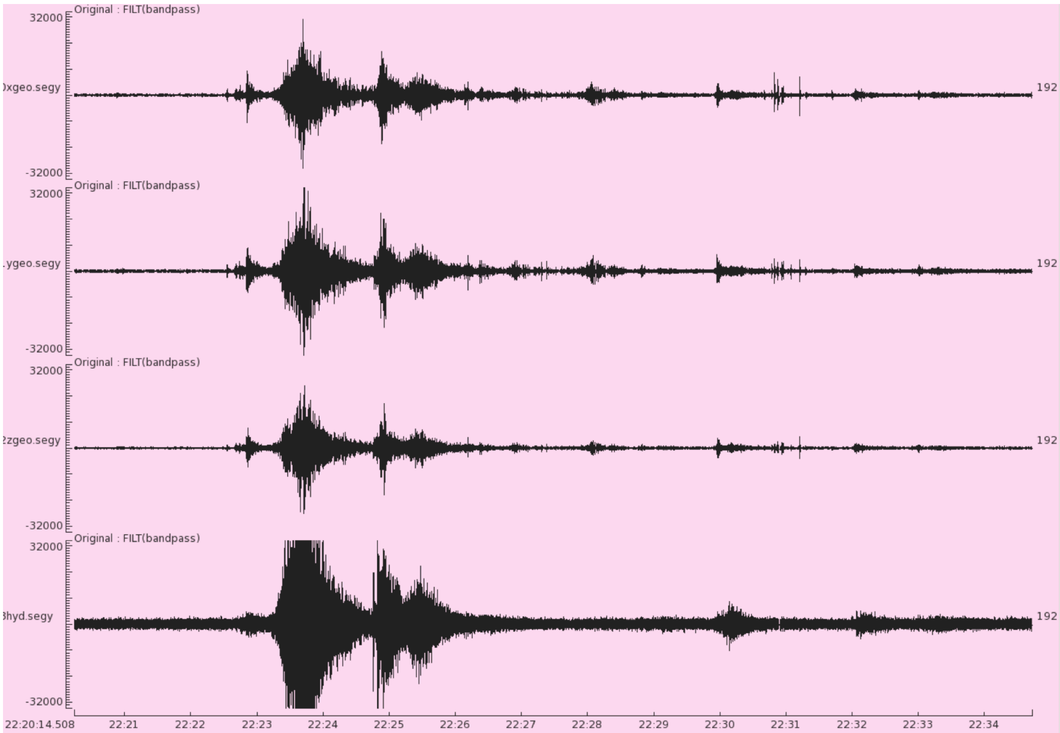

Figure 19: OBS data (top to bottom X, Y, Z geophone, hydrophone) from OBS test platform "Frank" showing local microseisic events occurring approximately every minute.

3.1.4 Instrumentation testing

During JC132 a set of prototype broadband sensor packs of different constructions was tested by the NERC's Ocean-Bottom Instrumentation Facility. Initially three systems were deployed and recovered during an Autosub dive as a test of the robustness of the high precision gimbal required to ensure the enclosed sensor package – a Nanometrics Trillium – deployed to the vertical position and locked there. These instruments were deployed again as part of the wide-angle Grid to record known-characteristic airgun shots as a means of testing the actual sensor output. These instrument platforms were subsequently recovered and redeployed as part of the supplement of eight OBSs for MCS surveying. An interesting side effect of this testing demonstrated, when the gimbal locking mechanisms were inspected post-deployment, that they landed on seabed dipping in excess of 30 degrees locally, and graphically demonstrating the severe topography of the seabed at mid-ocean ridges, that even the highest quality swath bathymetry data doesn't reveal.

3.2 Multichannel seismic reflection acquistion

Again all seismic operations followed JNCC guidelines as described in Section 3.1. The MCS data acquisition comprised primarily the Grid survey over the main OCC work area, coupled with an additional profile, Profile R, acquired to make best use of time remaining at the end of the cruise once the primary acquisition had been completed. A full list of the profiles collected and their parameters is given in the Appendix 4.

3.2.1 Grid survey

The MCS acquisition configuration is shown in Fig. 20. A 3 km-long Sercel Sentinel streamer with 240 groups each of 12.5 m active length (Fig. 20) was deployed, comprising twenty 150 m long sections. The first group was located 145 m behind the centre of the source array. Each section had attached a Digicourse bird to control and record streamer depth. Compasses in the birds also provided an indication of the bird orientation but there appears to be no way to record these orientations automatically and so this became a (laborious) job for the watch-keeper. However, the GPS location of the tail-buoy was recorded automatically using a system adhoc-developed by the Ocean-Bottom Instrumentation Facility on-board in between OBS deployments and recoveries, providing some knowledge of the feathering of the streamer.

The seismic acquisition system was a Sercel SEAL 428 which was set to record at 500 Hz over trace lengths equivalent to the shot repetition interval, including the output from a hydrophone mounted on each airgun sub-array tow beam that was input to the four auxiliary channels. The entire multichannel seismic recording system, including the streamer, birds and the Bigshot shot firing system (although all part of the NERC National Marine Equipment Pool), was operated by contractors from Exploration Electronics Ltd.

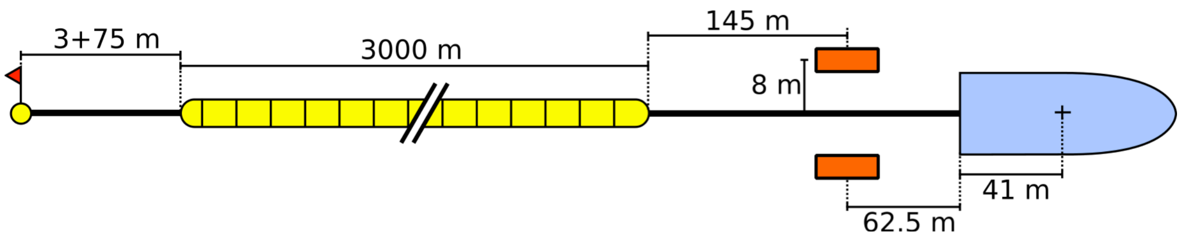

Figure 20: The acquisition configuration. Each sub-array had a width of ~6 m. Planned streamer tow depth 5 m.

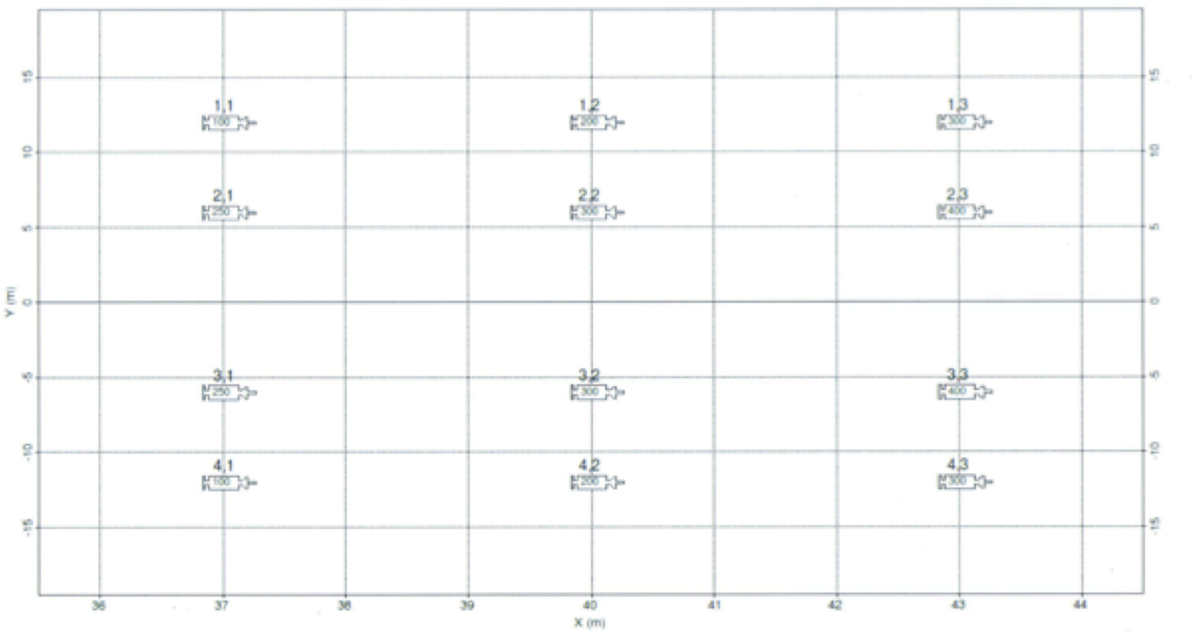

Figure 21: The airgun array used for MCS acquisition. The total volume was 3100 in^3, but for half the survey each sub-array (volume 1550 in^3) was shot separately at 10 s intervals.

For the MCS acquisition, the source again consisted of two symmetric sub-arrays of six airguns, each consisting of two beams carrying three airguns (Fig. 21). The central single 500 in^3 airgun deployed for the wide-angle survey could not be used, as the streamer is deployed centrally between the two sub-arrays. The airguns on each of the outer sub-arrays were also changed for the MCS surveying, using smaller airguns to increase the dominant frequency content of the seismic source signature.

The airgun array for the MCS acquisition was originally designed to include a 500 in^3 airgun on each of the outer beams. However, given the reliability issues experienced with the larger airguns in the array during the WA shooting, during the cruise we opted for smaller, but likely more reliable, airguns in the rear positions on the outer sub-array beams (Fig. 21). This decision was based on the repeated and multiple failure of air hoses. The potential exacerbation of the wear on the air hoses by shooting the MCS survey at a more frequent shot firing interval (20 s and 10 s as opposed to the 60 s shooting of the WA data acquisition) and the additional constraint of to-starboard-only turning whilst towing the streamer, apparently a result of the asymmetric wash characteristics of the two propeller'd *RRS James Cook* preferentially pushing near-stern towed elements to port, was considered too high a risk as the result would be not only protracted periods of downtime to repair the airguns themselves, but also significant amounts of time spent turning to get back on profile at a point before the failure occurred. As a consequence, adjustments were made to the array and the planned two 500 in^3 airguns were replaced with two 300 in^3 airguns.

Figure 22: Multichannel seismic streamer during deployment. The yellow Sercel Sentinel streamer is towed from the winch drum (foreground) astern over a fairlead suspended from the stern A-frame (centre of shot). Once deployed, the fairlead is raised to prevent streamer chaffing over the stern rails as the stern of the vessel heaves with the motion of the sea.

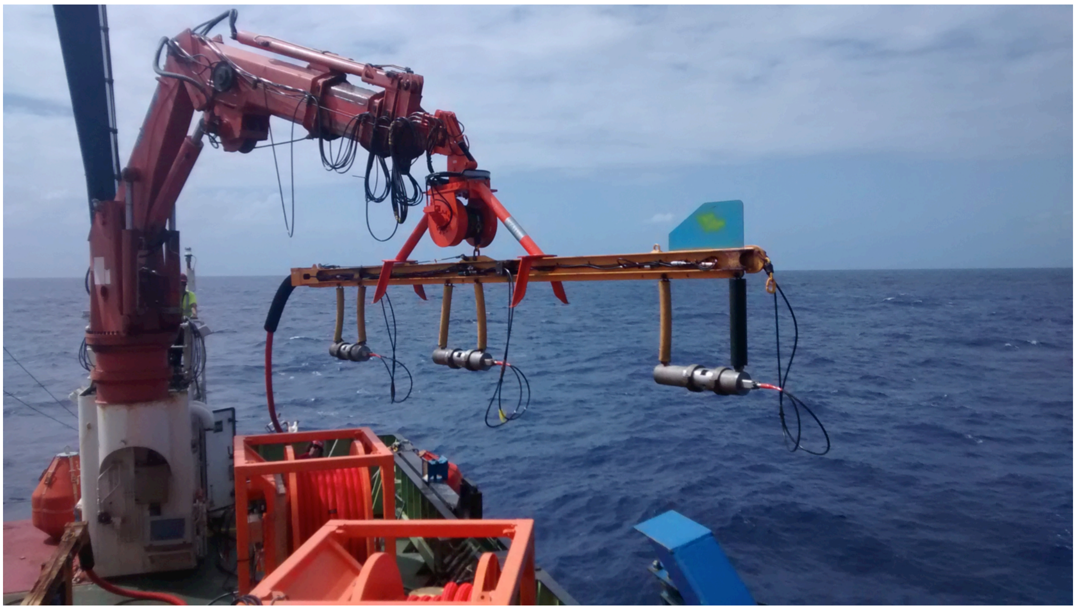

Figure 23: Inner beam of the port sub-array being deployed.

The resulting frequency spectrum (Fig. 24) shows a loss of power at low frequencies, prompting us to also have to tow the source array deeper at 8 m rather than at 5 m as planned. The emphasis on source reliability over optimum characteristics appears justified when the reliability of the array is considered: only once did an airgun hose fail (Profile 9 was shot without the 400 in^3 airgun on the inner port beam), requiring only one elongated turn (from Profile 9 onto 10) in almost 6 days of continuous shooting. The wavelet was acceptable (Fig. 25) and the amplitude spectrum, including both source and receiver ghosts, was fairly flat between 15 and 75 Hz, a range of over 2 octaves (Fig. 26). However, it was disappointing that carefully chosen acquisition specifications could not be followed due to reliability issues and limitations of the way airguns are towed from NERC' vessels. This cruise highlights once again, the urgent need for a better way of deploying and towing airguns.

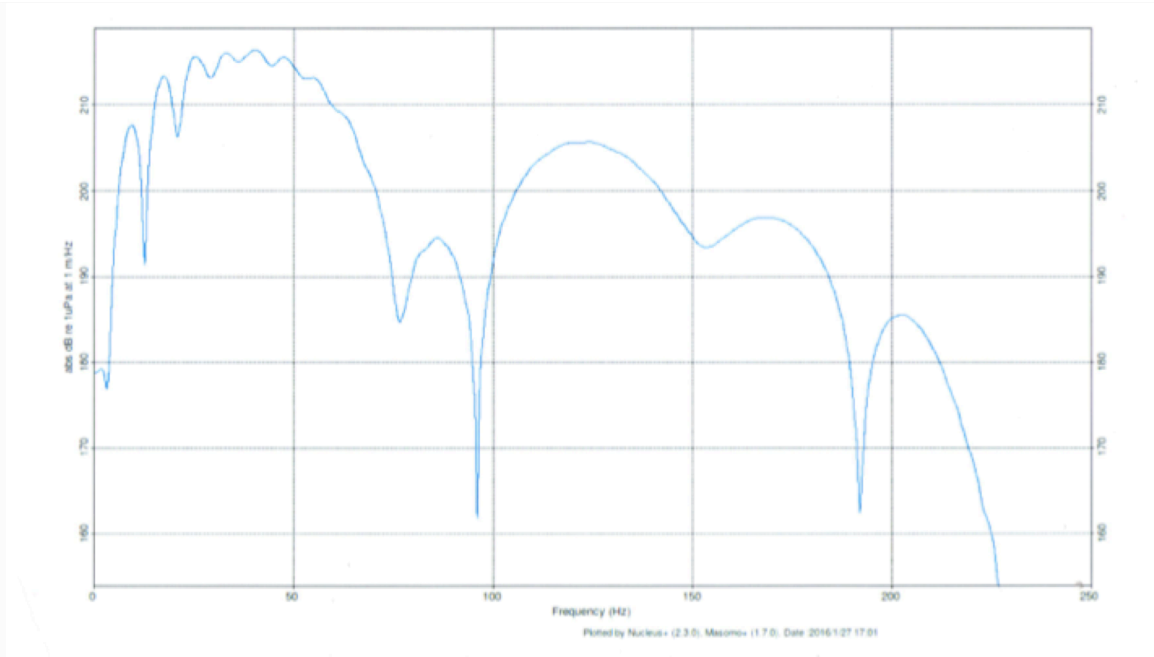

Figure 24: Predicted amplitude spectrum of the airgun array towed at 8 m depth, including both source and receiver ghosts (streamer at 10 m). Useful energy is found 10-70 Hz.

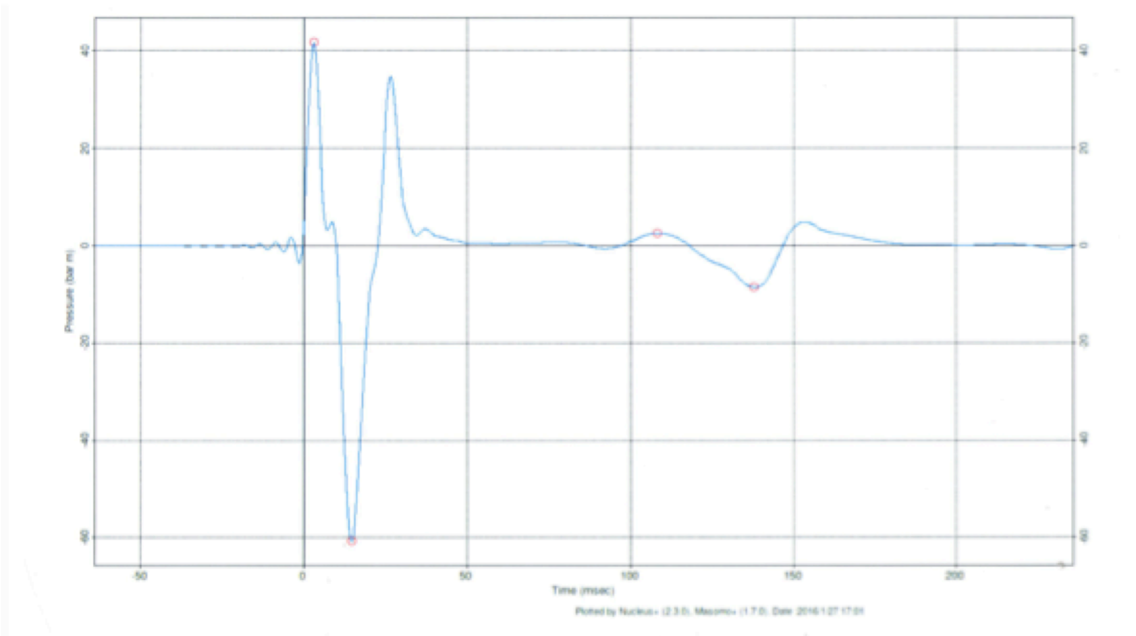

Figure 25: Far-field source signature of the MCS array, including source (8 m) and receiver (10 m) ghosts.

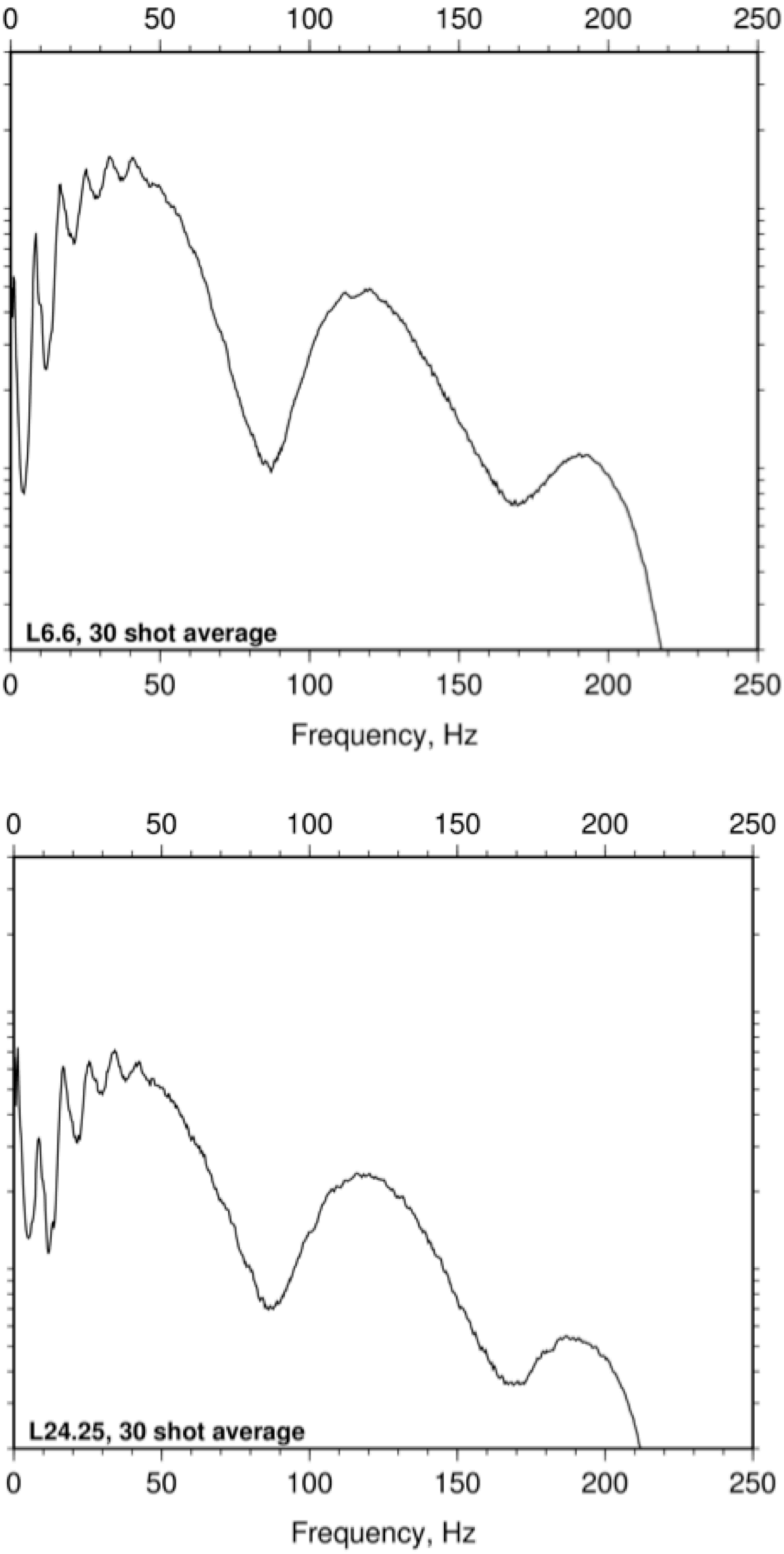

Figure 26: Actual amplitude spectrum of the airgun array towed at 8 m depth, including both source and receiver ghosts (average of 30 shots); differences with the predicted spectrum most likely reflects the variable depth of the airguns. Top: full array. Bottom: half array during flip-flop 10 s shooting, calibrated to same level as the full array. In both cases useful energy is found in the range 10-70 Hz.

During shooting it also became clear that the 8 m-tow depth was not being maintained: the rear airguns nearest the attached hippo flotation buoys were consistently ~2 m deeper than the front airguns. Given the 6 m length of the beams, it was clear that the beams were far from horizontal as in the specification, resulting in a far-field spectrum that is significantly different from the modelled one that underpins the array specification and experimental design.

Trials undertaken during JC131 had once again indicated that port turns with the streamer deployed carried too high a risk of significant equipment damage due to entanglement. The survey was consequently redesigned with entirely starboard turns at a maximum turn rate of 2°/min, corresponding to a turn radius of ~2.6 nm. Although the turns were generally made with little problem, they were once again unnecessarily fish-tailed.

Shooting started in the northwest of the work area (Fig. 27), with the streamer and the airguns being deployed on an easterly course into the wind and waves. Profile 1 continued to the east, crossing several fault blocks to the west of the 1330 OCC and then the entire length of the 1330 OCC and out across the spreading axis to the other plate. A 90° starboard turn was followed by a short north-south line segment (2), before another 90° starboard turn onto the east-west Profile 3 which skirted the northern edge of the 1320 OCC, then a 180° turn onto the west-east Profile 4 which crossed the deep basins between the 1320 and 1330 OCCs. The same pattern repeated, moving gradually southward in each cycle, building up a composite north-south profile east of the spreading axis through overlapping short line segments (Fig. 27).

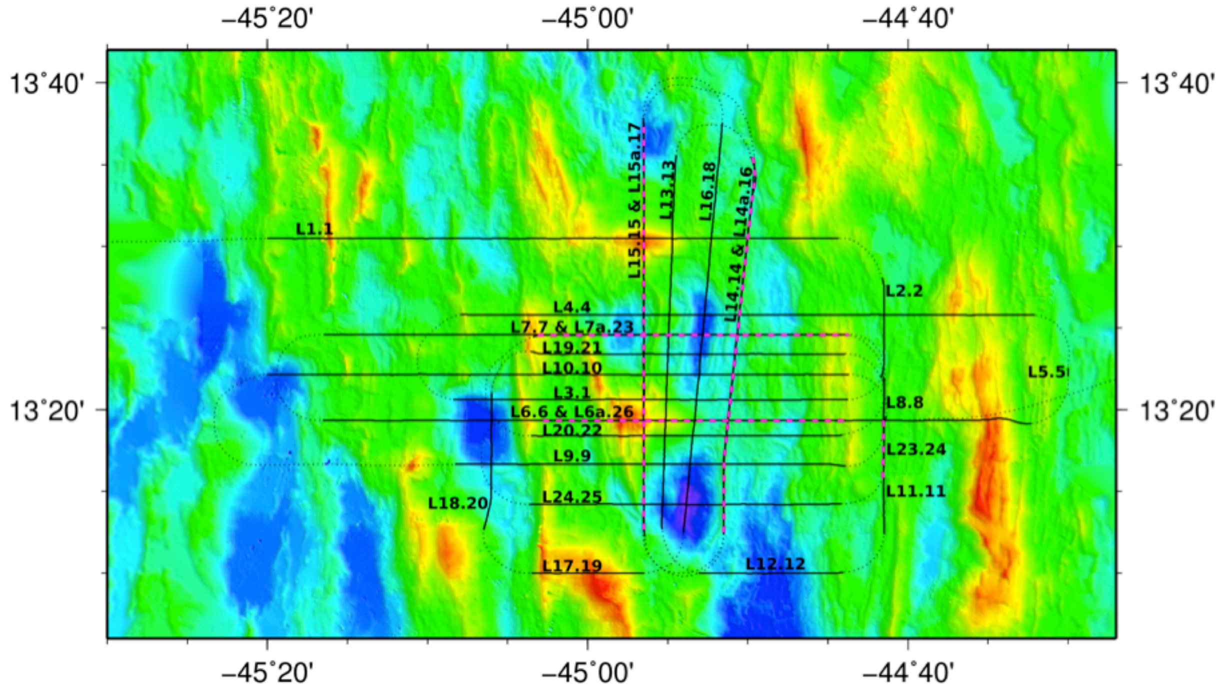

Figure 27: Map of the study area showing the MCS profiles acquired. Red lines show where a profile or part of a profile was shot twice using two different shot repetition intervals.

Initially, we decreased the shot interval to 60 s during the turns to provide better quality data for the OBSs recordings. However, we noticed that switching back to 20 s after a turn resulted in a loss of air pressure, hence power, for a substantial amount of time, as it took some time for the compressors to re-adjust to the increased firing rate (Figs 28-29). As a result, we reverted to the same shot interval around the turns as on profile, so that all shots were fired at the same pressure and, hence, with the same signature.

As expected, the raw MCS images are dominated by diffractive energy from the rough seafloor (Fig. 30), including those arising from out of the plane of the section. Simple quality control (QC) processing consisting of velocity analysis, NMO, stack and migration with a water velocity collapsed most of this energy to small bursts (Fig. 31), allowing some real reflections to be identified in the oceanic crust, but it is clear that considerable processing effort will be required to provide a clear image of the crustal structure.

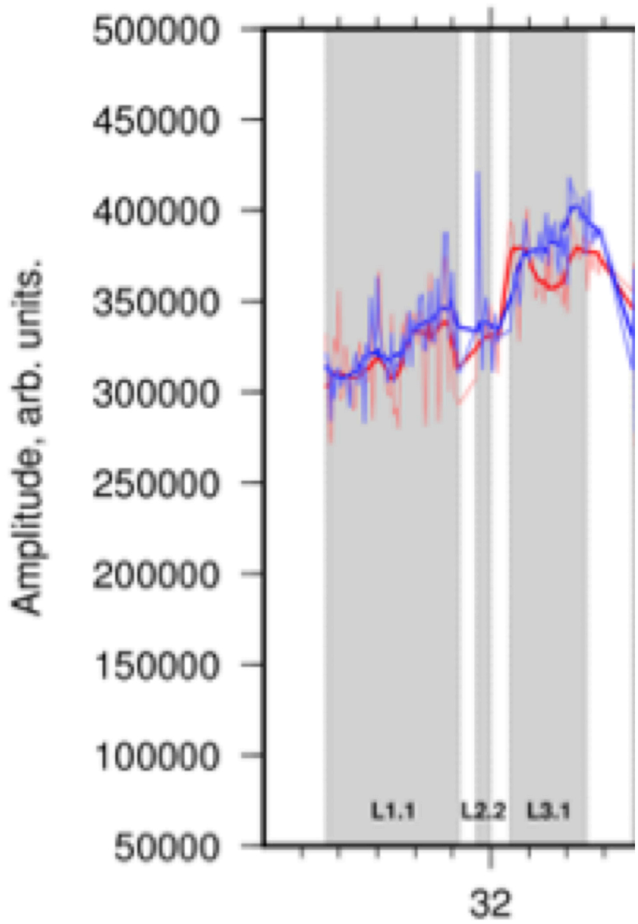

Figure 28: Plot of peak amplitude and average peak amplitude for MCS Profiles 1-3 plotted against Julian day. Red is the low frequency range (5-15 Hz), blue the higher frequency range (30-60 Hz). No signal amplitudes were recorded during the turns (white stripes). Note that on early profiles the signal amplitude ramps up with time and not immediately once the firing rate was increased from 60 s to that specified for the profile.

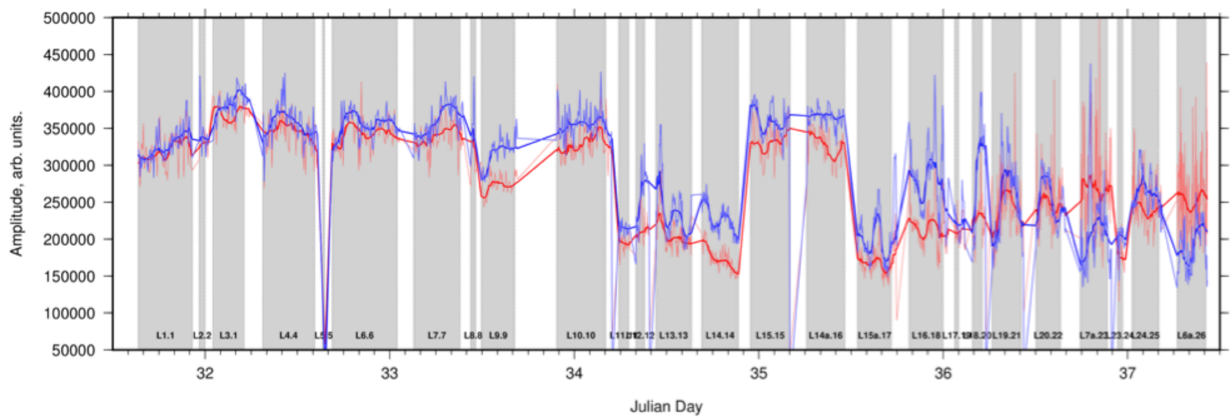

Figure 29: Plot of peak amplitude and average peak amplitude throughout MCS shooting. Red is the low frequency range (5-15 Hz), blue the higher frequency range (30-60 Hz). No signal amplitudes were recorded during the turns (white stripes). Note that on early profiles the signal amplitude ramps up with time and not immediately once the firing rate was increased from 60 s to that specified for the profile.

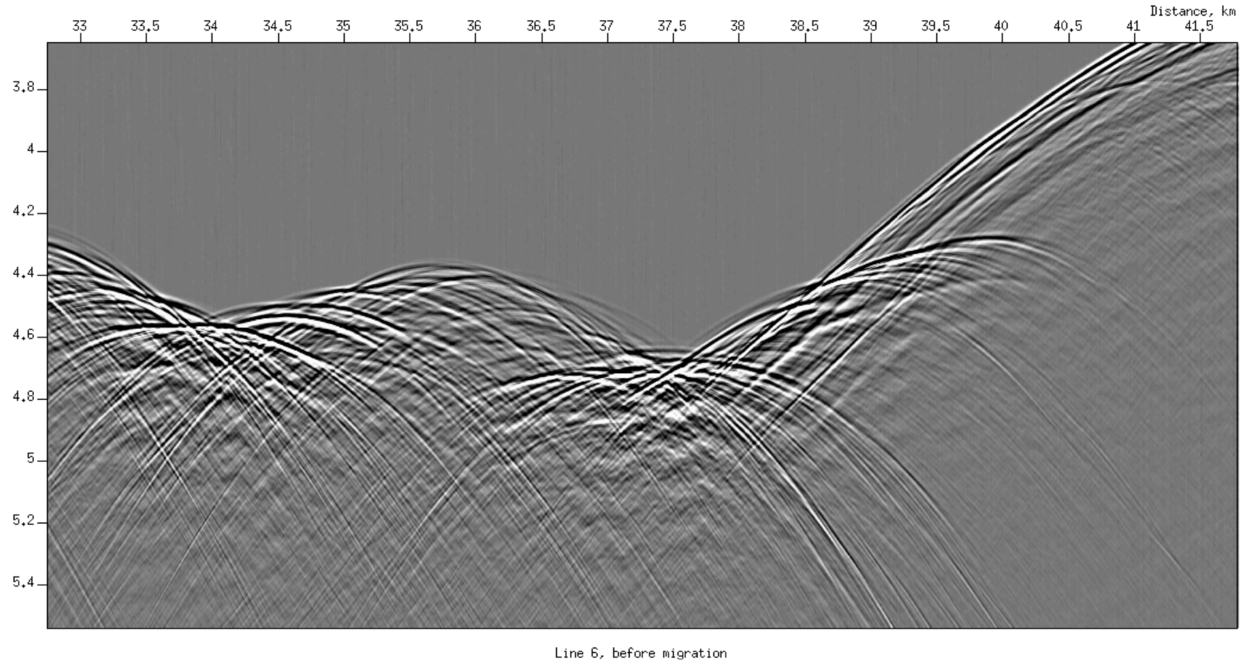

Figure 30: Detail of Profile 6 showing the diffractive nature of seafloor adjoining the smoother OCC.

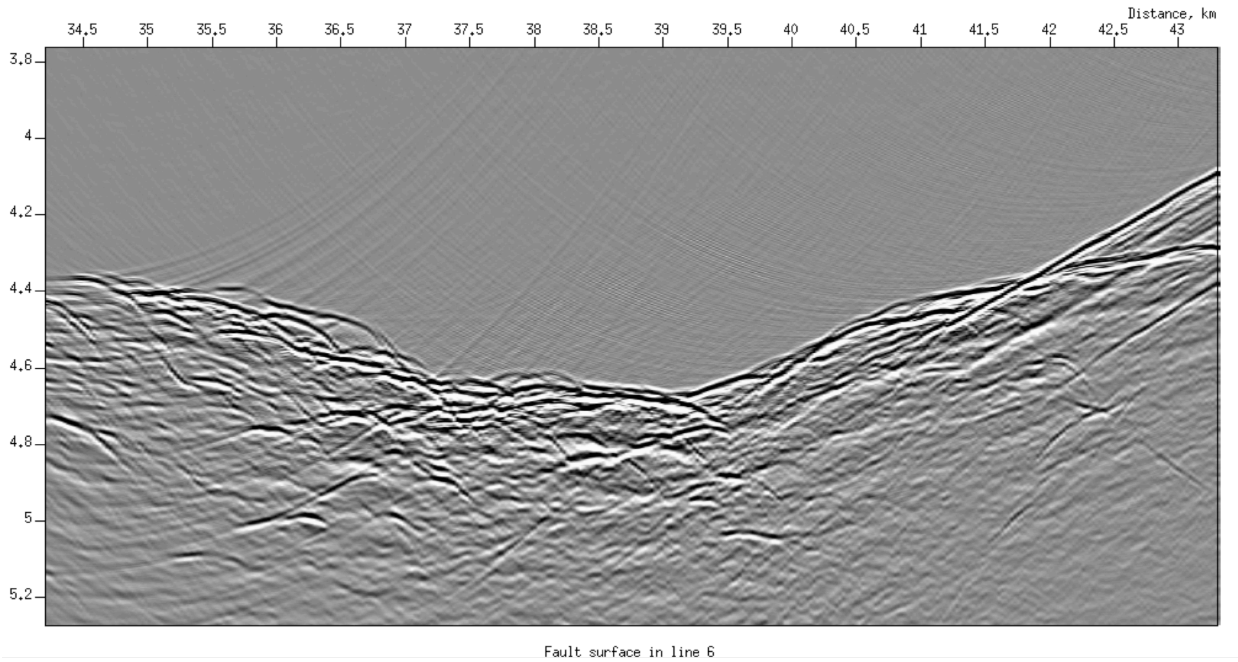

Figure 31: Image showing how water velocity migration of the stacked data collapses the scattered energy to small high amplitude bursts, allowing identification of real subsurface reflections.

A related issue to the amount of scattering is the degree of recorded reflections from out of the plane of the section. Using the bathymetry, it is possible to predict seafloor sideswipe and distinguish it from in plane reflections (Fig. 32). The data were shot on time rather than distance, meaning that the distance between shots varied as a function of the ship speed, with implications for subsequent processing, in particular CMP binning. For QC purposes, we explored two approaches: a standard marine geometry assuming a constant speed of 4.9 kn (20 s = 50 m) and binning taking into account ship speed. The later, unsurprisingly, produces a noticeably sharper image with more coherent real reflections (Fig. 33).

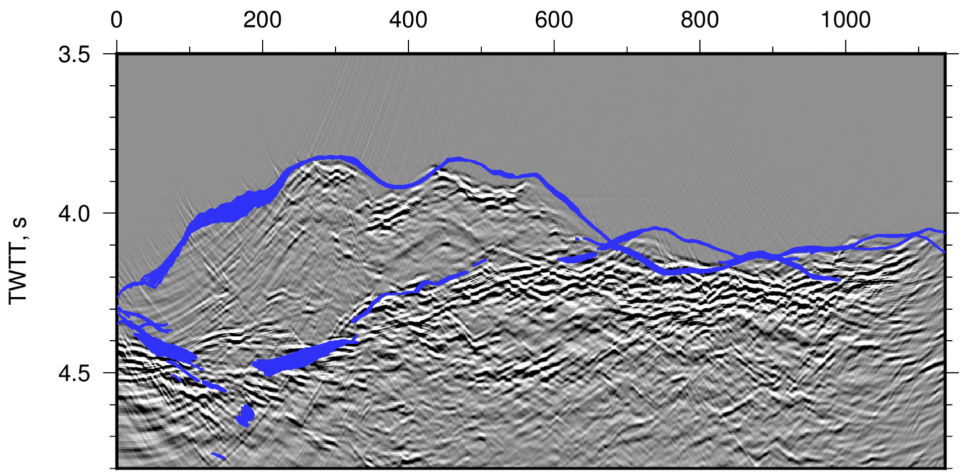

Figure 32: Predicted travel times of reflections from a 3D seafloor (blue) compared with the brute stack migrated with water velocity.

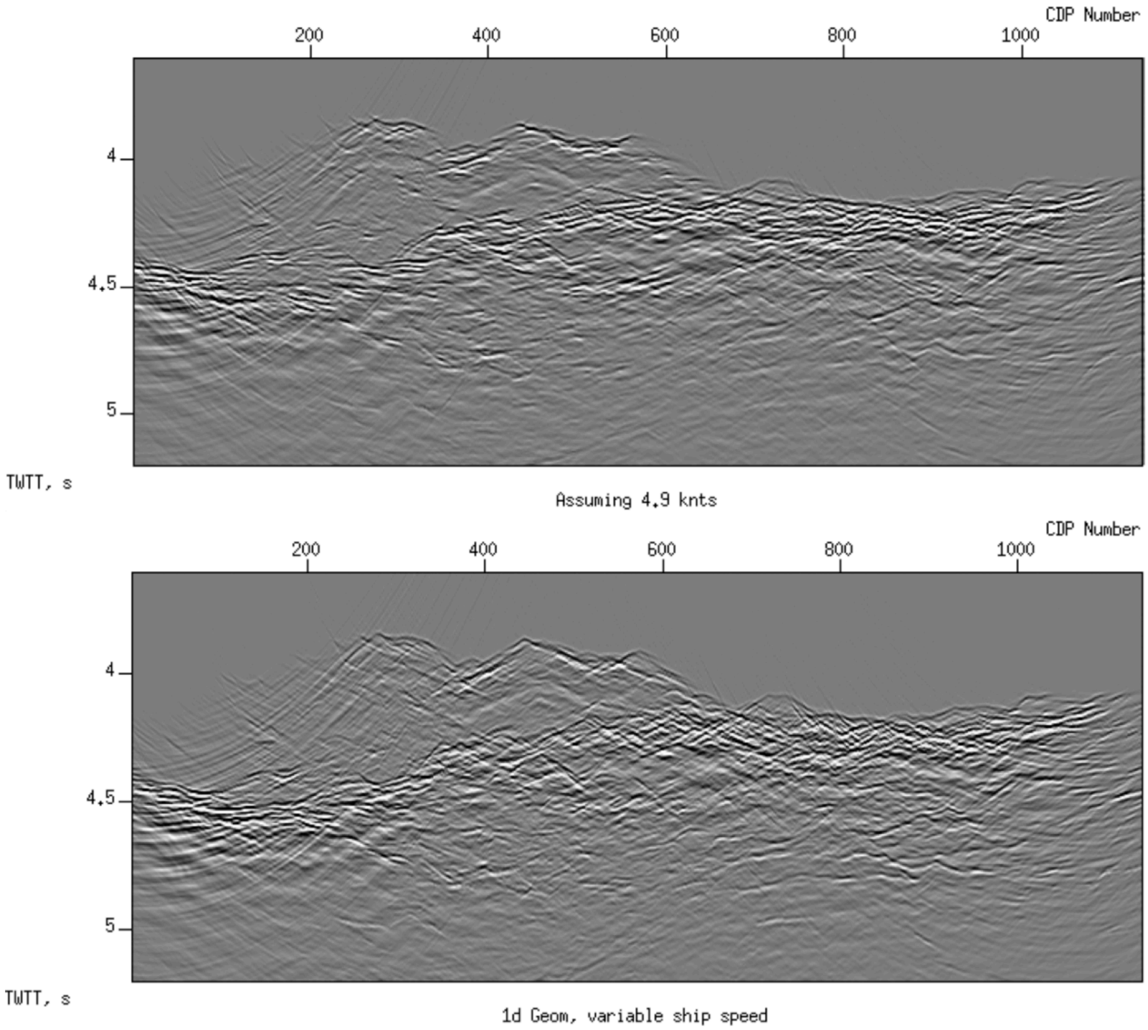

Figure 33: Top: processing assuming a constant ship speed, producing smeared out reflections. Bottom: processing in which the CMP locations are calculated from the ship speed, producing a far sharper image as expected.

After shooting of the initial profiles, the dominance of diffractions coming from the rough seafloor led to a change in acquisition strategy to 10 s shooting, starting on Profile 11. The aim was to reduce the shot spacing, increasing the fold and allowing more effective multi-trace processing in both receiver location gathers (trace spacing = shot spacing) and common midpoint gathers (trace spacing = 2 x that of shots), by reducing spatial aliasing of steep diffraction tails in both domains (Fig. 34). As the full array could barely be refilled in the 10 s between shots, we decided to alternate firing on the two sub-arrays, each firing once every 20 s in a flip-flop mode to give us the 10 s shot interval, equivalent to 25 m shot spacing at a speed of 4.86 kn.

In effect this retained the characteristics of the full source (as the array was designed to be symmetrical about the median line) but distributed the energy along the line: simply adding adjacent shots would thus create a synthetic array ~31 m long (shot spacing + beam length), although that particular processing strategy would limit our options. Four profiles were shot at both 20 s and 10 s flip-flop intervals – Profiles 6, 7, 14 and 15 – providing an opportunity for both comparison of the two shooting strategies with real data and potentially for combining each pair into a single line. The switch to flip-flop shooting with half the array size also led to a doubling of the fold, the nominal 30 fold, becoming a nominal 60 fold (Fig. 35).

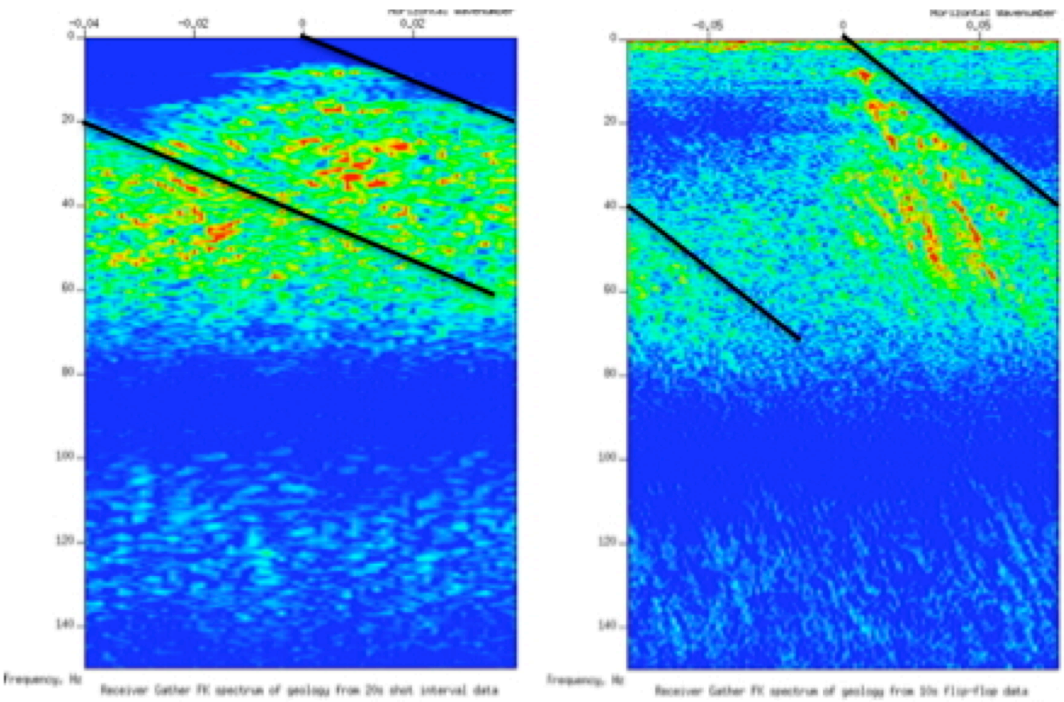

Figure 34: Comparison of the fk spectra of a receiver location gather with 20 s shooting (left) and 10 s shooting (right). Note how the closer shot spacing results in far less spatial aliasing (energy beneath the lower black line). Also note useful energy in the range 10-70 Hz.

The only break in acquisition during the Grid survey came at the end of Profile 9. Just before the start of this profile, the 400 in^3 airgun on the port side inner beam failed (the air hose had become disconnected), meaning that the rest of the profile was shot without this airgun. At the end of the profile, the beam was brought in and the hose repaired. Following the turn, shooting started on Profile 10 much further west than originally intended due to the length of time required to complete the repair (c. 4 hr) which was a consequence of an attempt being made to recover the inner beam of the array without first recovering the outer, which is the standard practise. Such a repair would have normally taken just 30 min if the standard practise approach had been taken. As an outer beam is normally recovered during a repair to an inner beam airgun, this also normally offers the opportunity to give those airguns and their hoses and firing cables a service review (e.g. hose and cable tightening and inspection) at the same time. This was not done in this case for reasons that remain unclear.

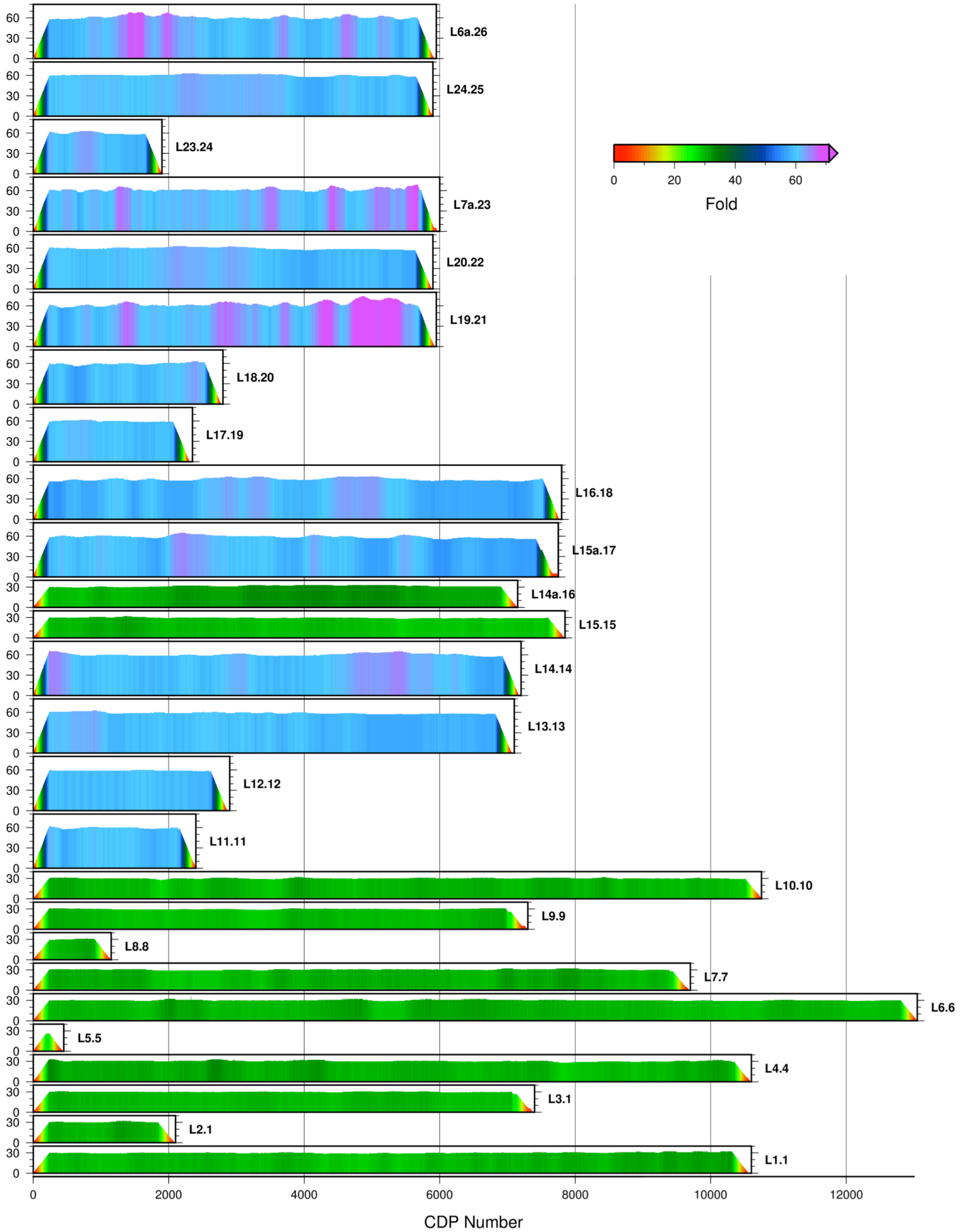

Figure 35: Length and fold of seismic profiles. The switch to flip-flop shooting resulted in a doubling of the fold. The other variation in fold is the effect of varying ship speed on CMP binning. Profile 5 was a straight segment on a turn used for a noise test.

3.2.2 Profile R

Profile R was shot mainly for wide-angle data acquisition into 14 OBSs deployed along a north-south transect, ridge-parallel and crossing a fracture zone to the south, and hence had a 60 s shot interval to push the water wave wrap-around out to longer offsets. The airgun array used was the same as during the dedicated 60 s shooting into the OBSs, but without the central, independently towed 500 in^3 airgun, as the streamer was also towed during this profile. During the profile, the loss of a hippo buoy required that the entire starboard outer beam of airguns be turned off, resulting in a marked drop in amplitude, clearly to be seen in the amplitude spectrum calculated for this profile (Fig. 36), and particularly so for the lower end of the frequency spectrum that is primarily used for deeper crustal WA data acquisition. The consequence of the instantaneous loss of 30% of the array by volume is quite evident in both the WA and MCS record sections (see Section 3.1.2 and Figs 37-38).

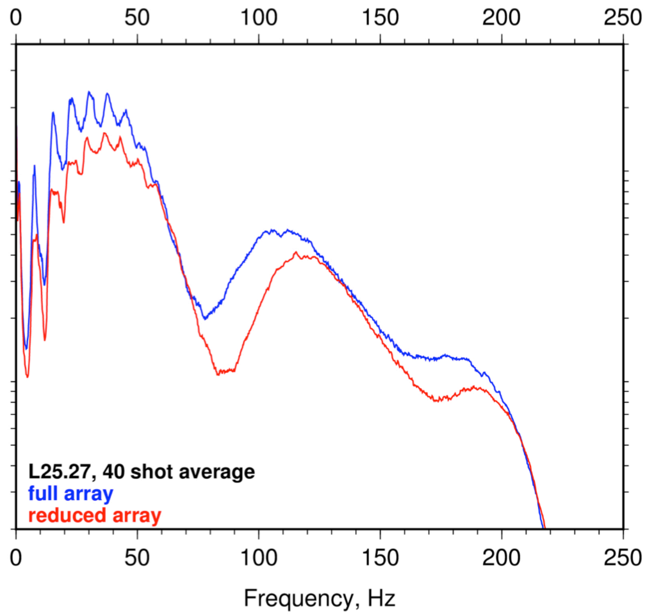

Figure 36: Amplitude spectrum of the full array used during Profile R, compared with the spectrum after the drop out of one beam containing the (500, 400 and 300 in^3 airguns) due to the loss of its depth-control flotation.

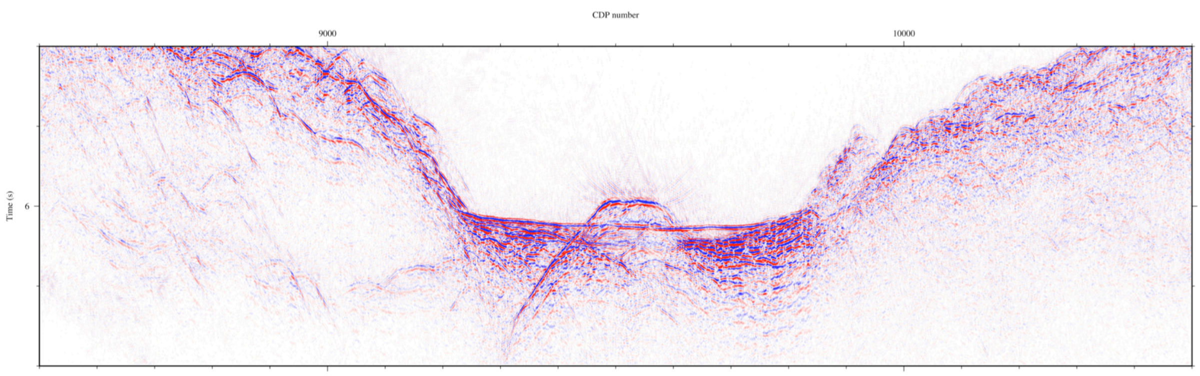

Figure 37: Brute stack of MCS data acquired along Profile R, south-to-north, showing sediment ponded in the bottom of the fracture zone marking the southern limit of the 13N MAR segment.

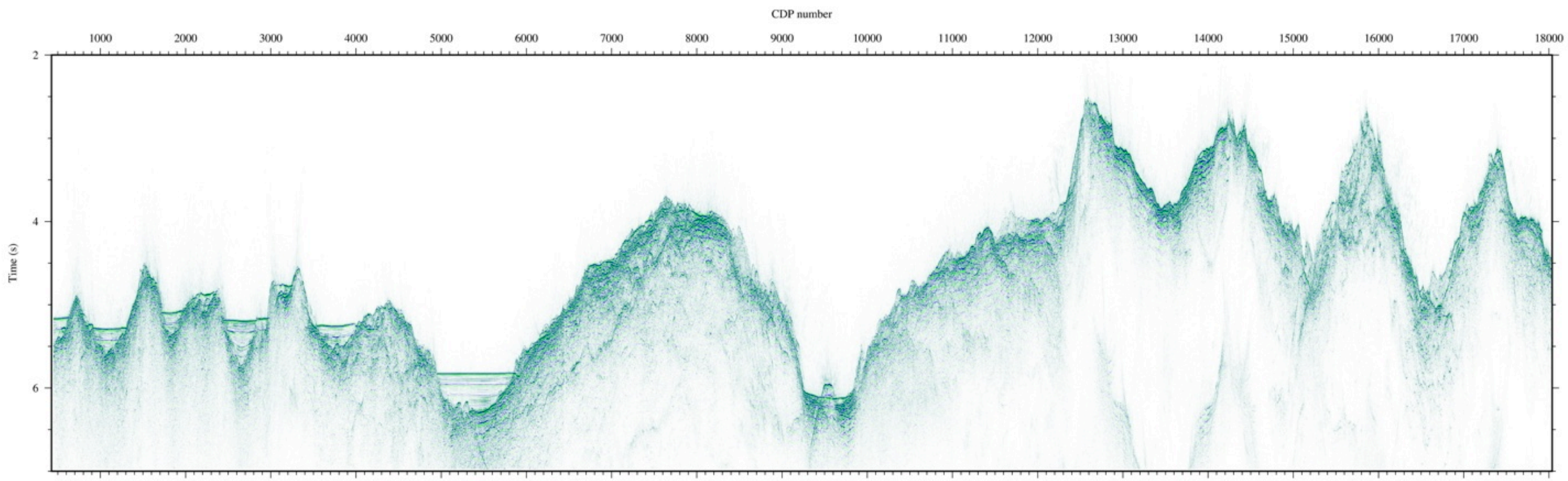

Figure 38: Brute stack of MCS data acquired along Profile R, south-to-north, showing sediment ponded in between the basement highs of the older lithospheric crust (left) and in the bottom of the fracture zone marking the southern limit of the 13N MAR segment (centre), and the severe topography of the zero-age lithospheric crust of the 13N MAR segment to the north (right). The 14 OBSs of Profile R were deployed along this topography.

3.3 Gravity

Gravity data were acquired port-to-port using a Micro-G Lacoste-Romberg air-sea gravimeter (S-40) mounted on a gyro-stabilised platform (Fig. 39). The gravimeter was "tied" to an absolute base station at the NOC, Southampton (UK), prior to departure for JC131, tied again to an absolute station in Mindelo (Cape Verde), and to a new absolute base station established in Port of Spain (Trinidad - organised by one of the PIs) as part of this project. Details of the gravity base station ties are provided in Appendix 6. An example processed (for QC purposes only) data profile from the cruise is shown in Fig 40.

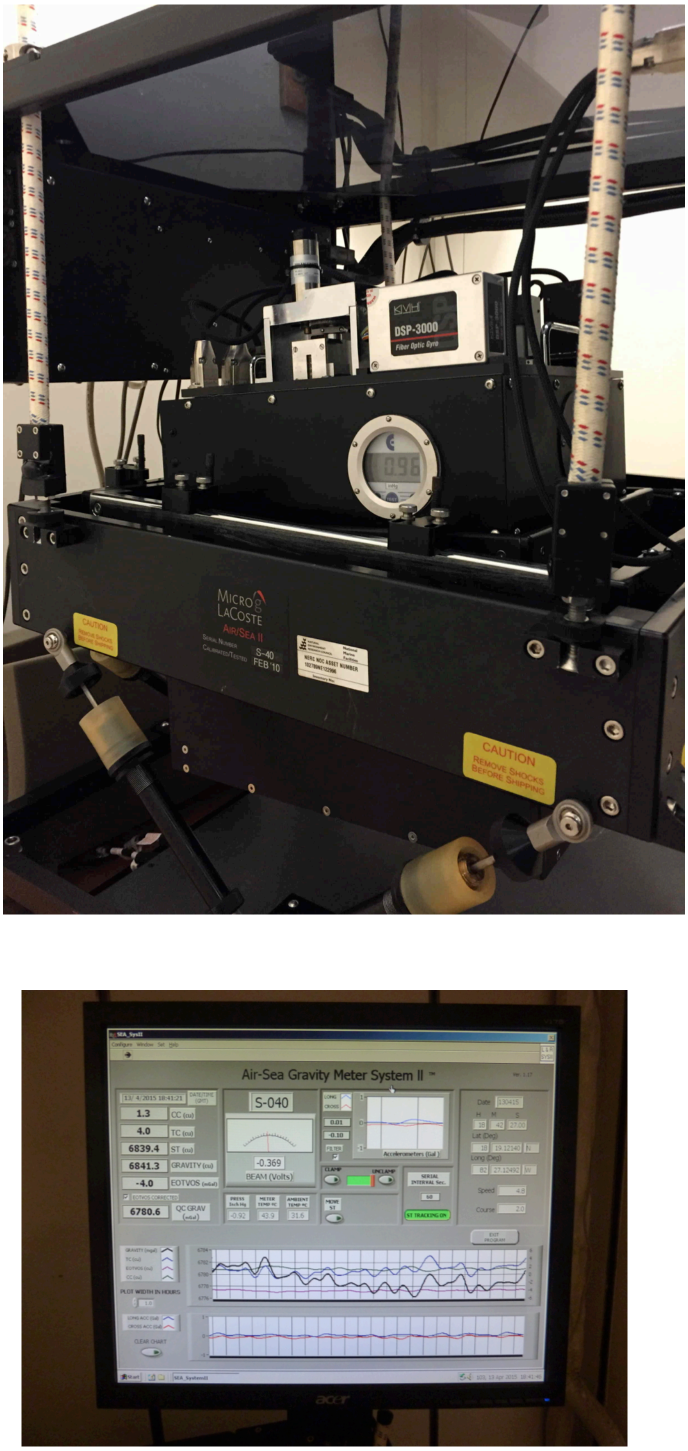

Figure 39: S-40 gravimeter on the *RRS James Cook*, showing blow-up of acquisition screen which is also mirrored in the main lab.

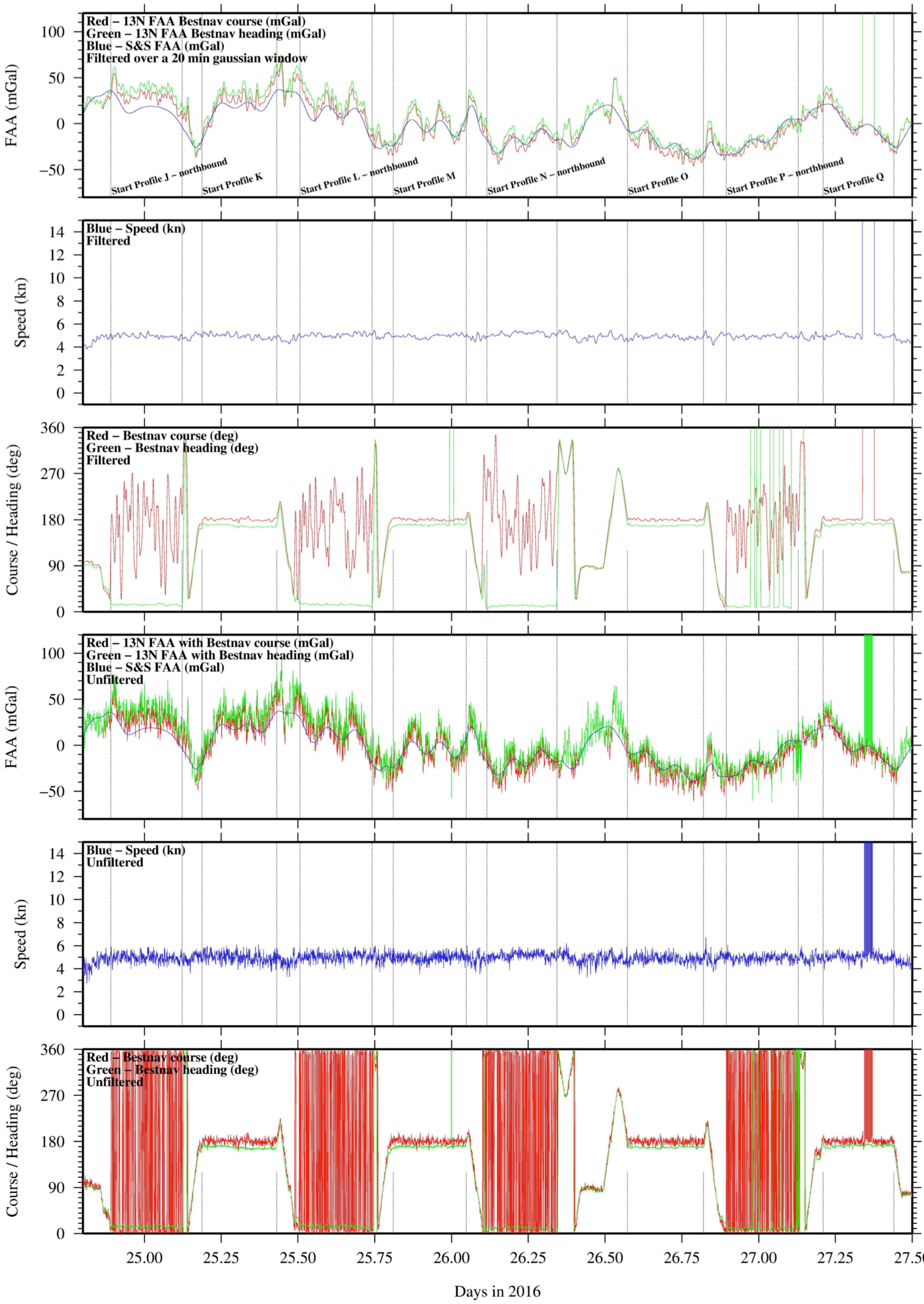

Figure 40: Example gravity data (top panel in each set) from WA Profiles J-Q running ridge-parallel along north-south courses, plotted against the speed, course and heading from the *bestnav*. Top set of plots are filtered versions of the bottom set. The Sandwell & Smith (v18) satellite FAA anomaly is also shown for comparison and as a check on meter operation. See labelling on each panel. The northbound legs have a course/heading that varies either side of 360/0° and so need special treatment before filtering/smoothing that has not been applied as part of the QC review. Note the large scale deviations in the *bestnav* (right hand side c. Day 27.35) that is not apparent in the raw navigation data stamping stream input into the gravimeter, and stored as part of those raw data files.

When JC132 was scheduled there was no extant absolute gravity base station remaining in Trinidad. Prior to JC132, JC102 and JC109 had already ported there (as legs 1 and 2 of the 13N project) and, as such, the gravity data acquired during those cruises was untied to an absolute reference framework which also meant that meter drift was also unknown, and the data unusable as a consequence. To enable all three cruises' worth of gravity data to be usable required an absolute gravity station to be reinstalled somewhere in Trinidad, and the meter on the *RRS James Cook* could not have its operation interrupted during JC132, so that the port ties in Southampton (UK) and Mindelo (Cape Verde) were maintained to the end tie in Port of Spain (Trinidad). Consequently, during JC132 the marine gravity the ship's Platform Systems technical staff and the watch-keeping team monitored the meter very carefully.

One of the PIs made arrangements to hire an absolute gravity meter from the NERC's Space Geodesy Facility (SGF), together with an operator, and for the meter to be shipped "hot" (under power and vacuum) on the *RRS James Cook* from its departure from the UK in December at the start of JC131. The vessel's Platform Systems technicians also monitored this instrument very carefully as it is extremely delicate.

On arrival in Port of Spain the absolute gravity meter was unloaded and transported to the site chosen by the Trinidad & Tobago Government, installed and tested. Found to be fully operational, a series of measurements were taken over the following two days, 24 hrs a day. The meter was regularly monitored during that period. On completion, the meter was disassembled and transported back to the *RRS James Cook* to be shipped back to the UK "cold". The absolute gravity meter installation is shown in Fig. 41.

The free-air anomaly (FAA) calculated from the ship-based measurements and underway navigation is shown in Fig. 42 to the work area, and Fig. 43 for the across-ridge-axis WA Profiles A-I, and are a good fit to the Sandwell & Smith satellite anomaly giving confidence in meter operation. To calculate the FAA requires knowledge of the location, speed and course of the vessel to apply the necessary latitude and Eotvos corrections. However, as Fig. 40 shows for the ridge-parallel WA Profiles J-Q, the *bestnav* used for this process has a number of issues, which will be discussed in Section 3.7.

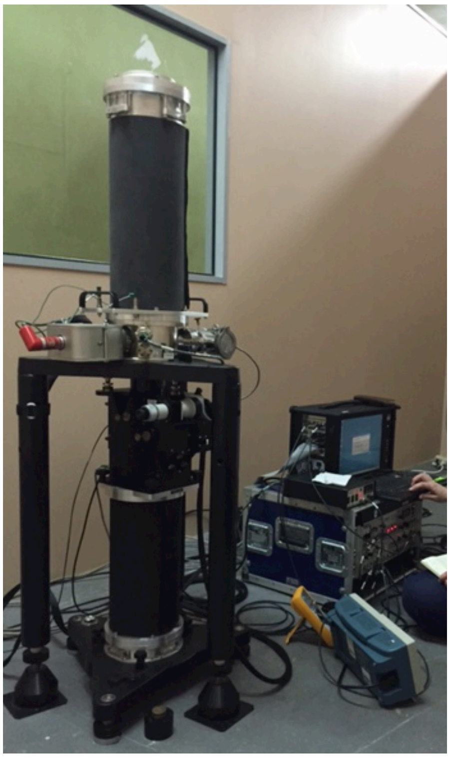

Figure 41: Absolute gravimeter taking measurements in Port of Spain (Trinidad).

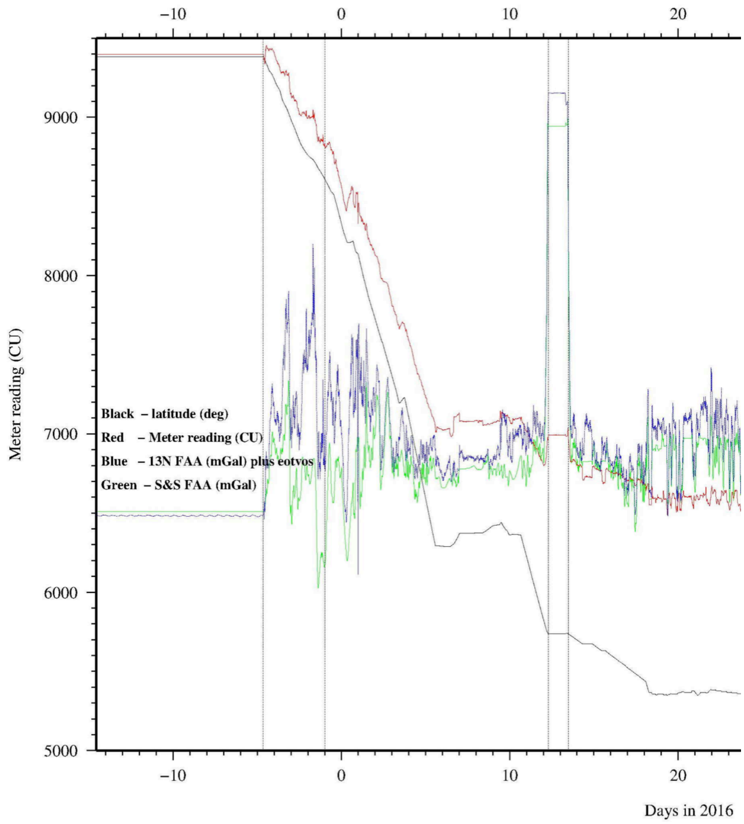

Figure 42: Gravimeter reading (red) compared to latitude (black), Sandwell & Smith satellite free-air anomaly (green) and that calculated for JC131 and JC132 to arrival in the work area. The effect of bad weather during the Biscay crossing during JC131 (days -4 to 2) can clearly be seen, as can the general correlation between meter reading and latitude during the transit south. The Mindelo (Cape Verdes) port call is evident during days 12-14.

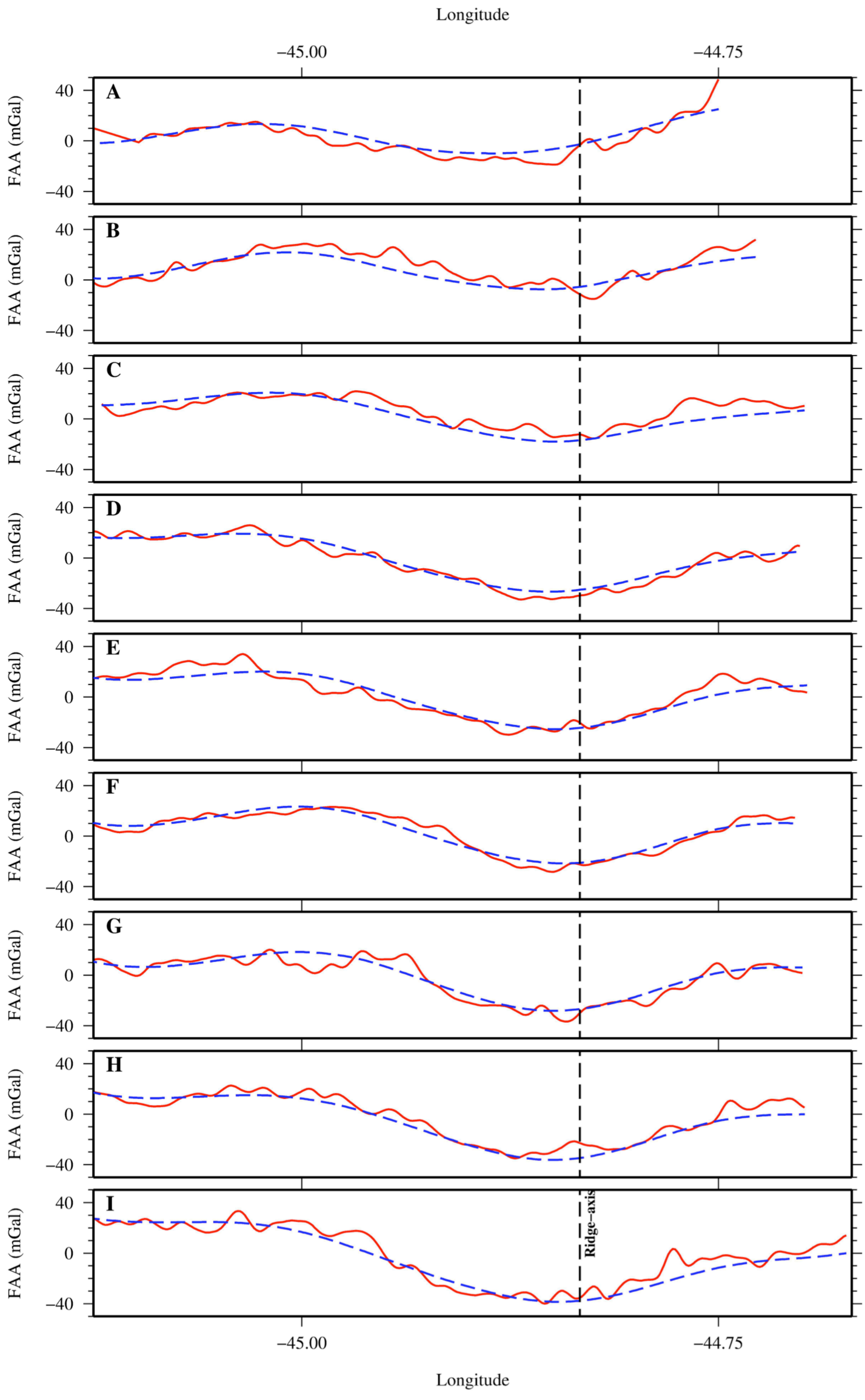

Figure 43: Example free-air gravity anomaly (red) from WA Profiles A-I crossing the ridge-axis, with the Sandwell & Smith (v18) free-air anomaly (blue dashed) extracted along the same profiles for comparison. Profiles F and G are located either side of the 1320 OCC. Note the good correlation between the ship data and satellite data.

3.4 Magnetics

A SeaSpy magnetometer (SN 13358) was deployed throughout all seismic surveying. The sensor lay-back from the ship's GPS reference point was input into the data acquisition “BOB” software and the correction applied during profiling. Fig. 44 shows the deck installation of the tow fish and winch, and the damage done to the tow cable, most likely by shark attack given the punctures and insulation stripping, during towing for the MCS survey. Example data profiles are shown in Fig. 45 for the east-west orientated WA Profiles A-I, corrected to the IGRF12 total magnetic field. Spikes are evident in the raw data and may be pick-up of ship-generated noise. Note also that the anomalies are offset, at approximately hourly intervals due to steps in the longitude of the navigation data stored in the raw magnetic data files.

Figure 44: Magnetometer installation, showing cable damage that occurred during towing. Puncture marks were also present.

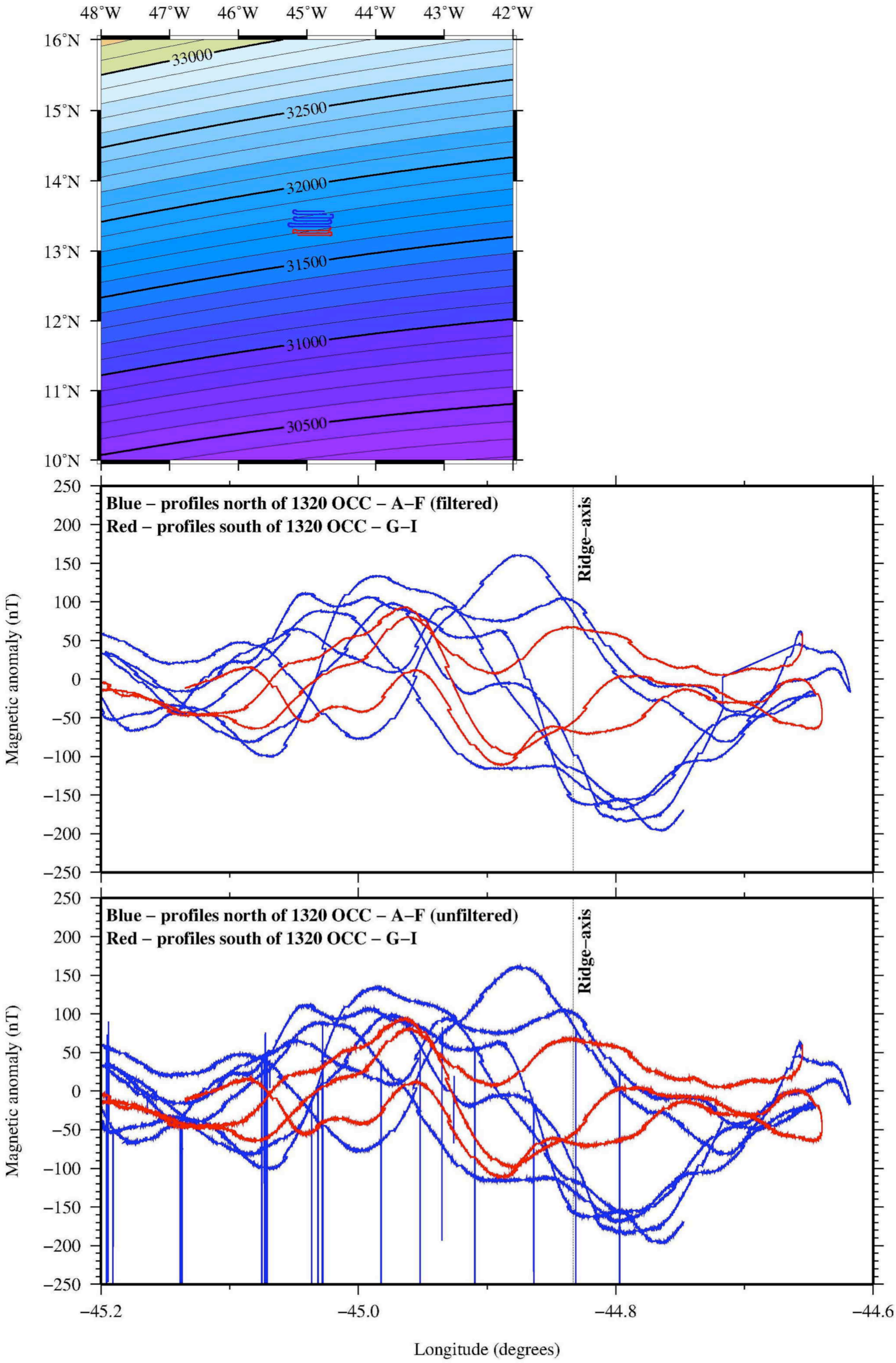

Figure 45: Example magnetic data for WA Profiles A-I, acquired across-axis, corrected to the IGRF12 total magnetic field. The spikes are possibly pick-up of ship-generated noise. Note the stepping in anomaly trend (middle plot) due to navigation issues in the stored raw data files. Top: IGRF calculated for the work area with ship tracks superimposed.

3.5 Sound velocity profiling

A sound velocity profile (SVP) was conducted in three places: one day out of Mindelo (January 15, 2016), in the north of the work area on arrival (January 19, 2016) and further south while waiting for an opportunity to deploy Autosub (see Appendix 7 for deployment locations) using a Valeport Midas sound velocity probe. The second profile was used to calibrate the EM120 swath bathymetry system, the third to check that that calibration was still valid and taking the opportunity to profile the entire water column in the deepest part of the study area. The resulting profiles are shown in Fig. 46. One of these SVPs was acquired in the same location as those undertaken during JC102 (April 2015) and JC109 (October 2015) and these are plotted for comparison in Fig. 47, together with an expendable bathymetric thermograph (XBT) also deployed during the cruise.

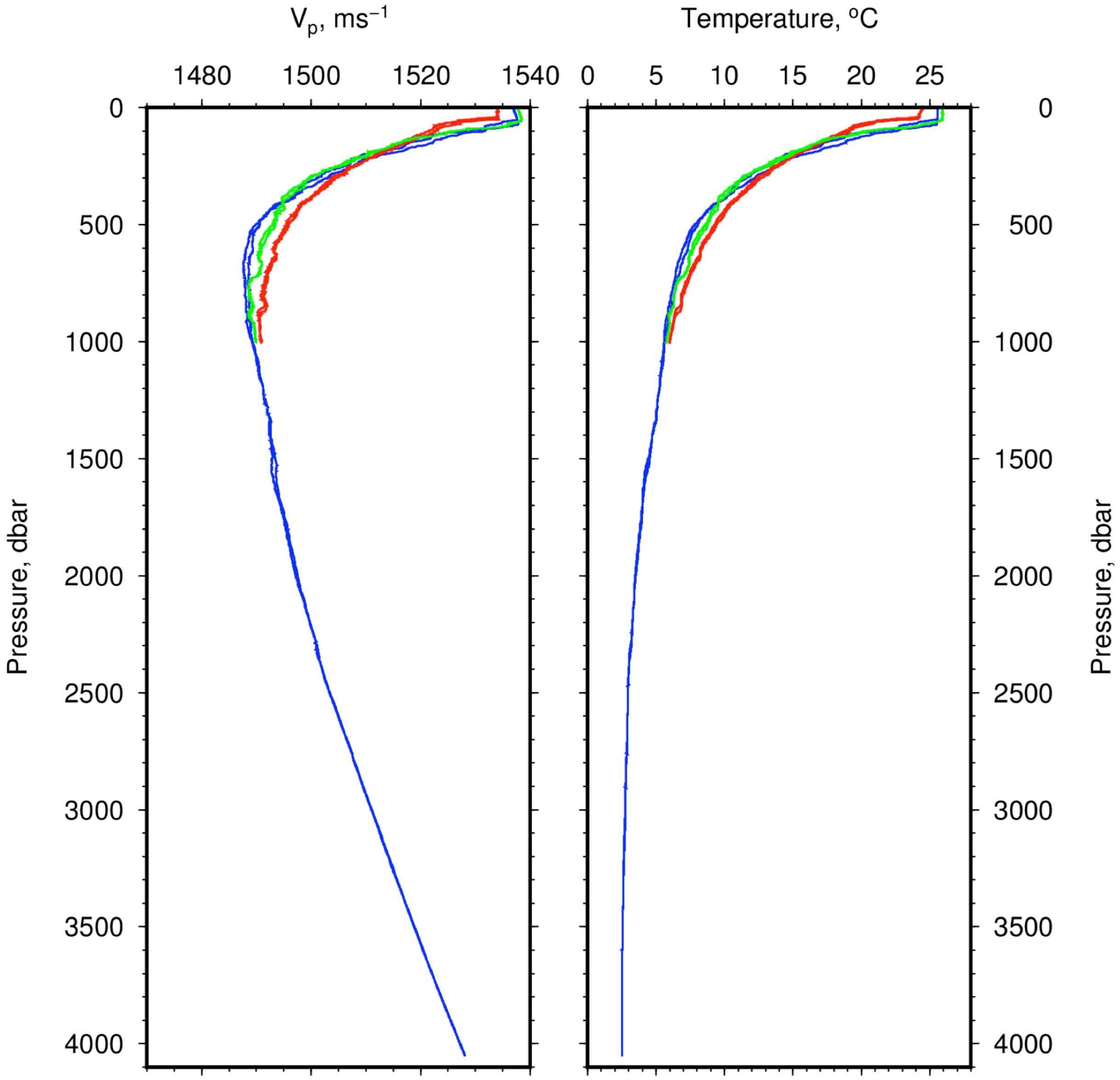

Figure 46: Comparison of velocity vs. depth and temperature vs. depth from the three SVP deployments undertaken during the cruise. The red curve was collected in transit (JD 15), the green one on arrival in the study area (JD 19) and the blue one towards the end of the programme (JD 42).

Comparison between the three SVPs undertaken at the same calibration point during all three cruises (Fig. 47) shows that there is a significant difference in water column velocity structure throughout the year and, more importantly, that a significant thermocline exists that varies from 50 m thick to 80 m depth between spring and winter.

Significant acoustic issues for vertically travelling communications signals were experienced throughout each of the three cruises as a result, including during the testing of the OBS acoustic releases undertaken using a bespoke carousel lowered from the starboard side gantry. All communications with the OBSs were undertaken from several nautical miles offset as a result.

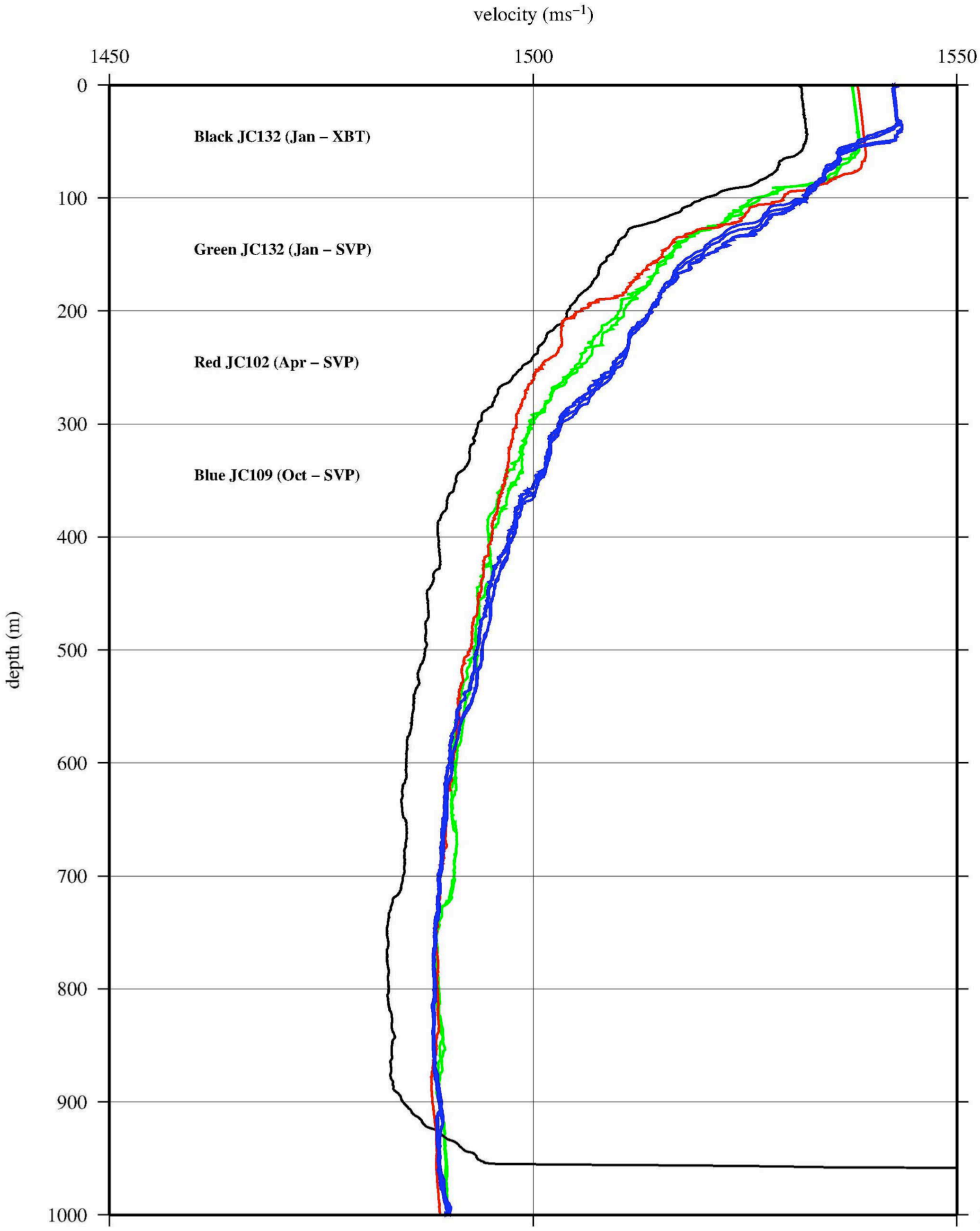

Figure 47: Comparison of velocity vs. depth for the three phases of SVP deployment undertaken during the 13N project co-located at the calibration site in the north of the 13N work area. The red curve was collected during April 2015 during JC102; the blue, two two-way (down and up) SVPs undertaken in October during JC109; and the green two-way SVPs undertaken in January during JC132. The JC132 XBT profile, undertaken at the same location to calibrate all further XBTs against, is also shown.

3.6 Swath bathymetry acquisition

The *RRS James Cook* is fitted with a Kongsberg Simrad EM120 multi-beam deep ocean echo sounder. Data acquisition is based on successive transmit-receive cycles with the beam width optimised to match the sea conditions. Seabed depth and reflectivity are recorded against UTC time and GPS location. All swath bathymetry data acquired in the work area are shown are Fig. 48.

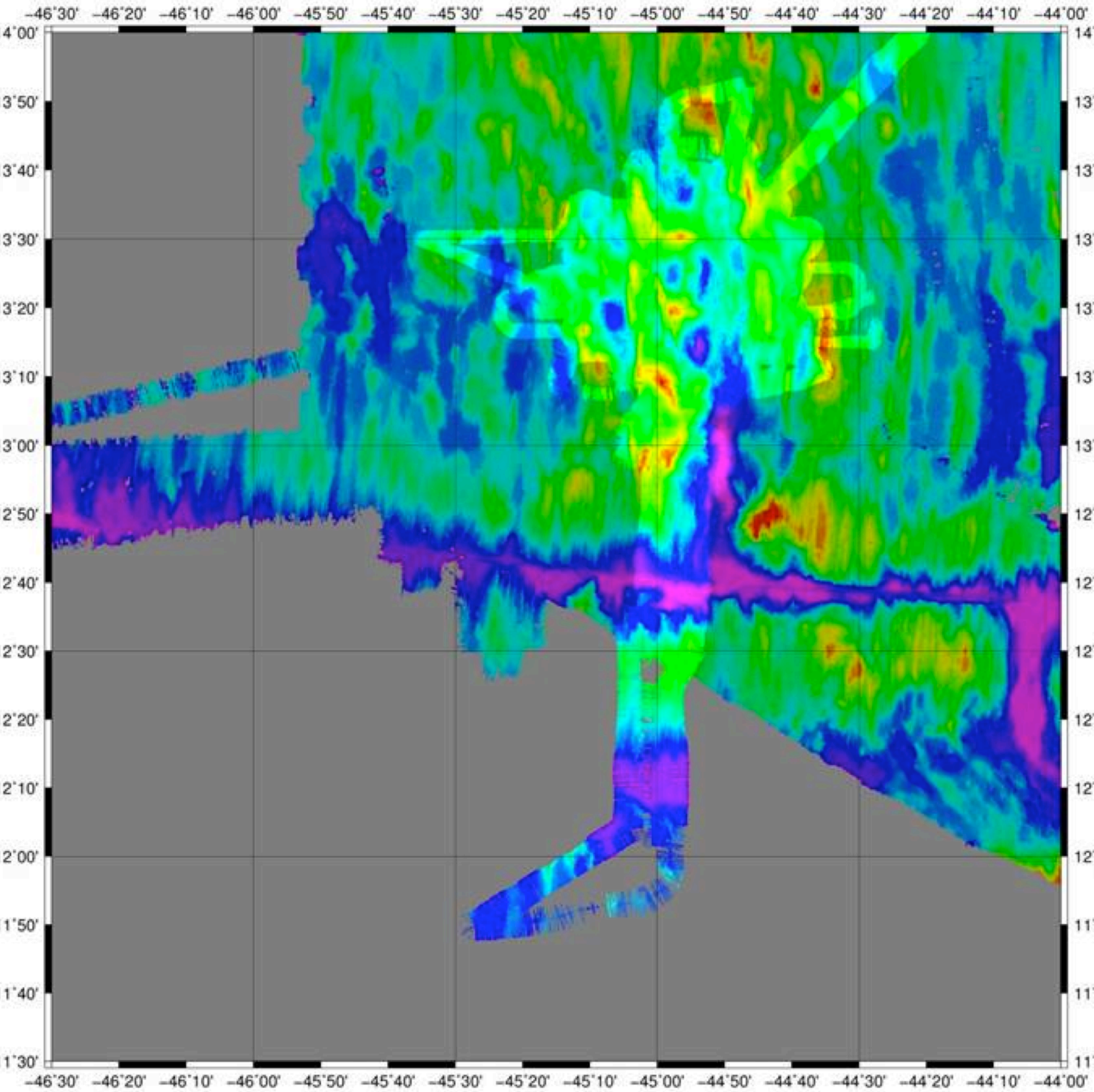

Figure 48: Swath bathymetry data coverage collected on JC132 in the study area (bright colours) superimposed on existing data, including that from JC102 and JC109.

Swath bathymetry data were acquired port-to-port, and for all seismic profiles acquisition was configured with beam angles of 45 degrees on either side, providing a swath width approximately twice the water depth. The multitude of track lines over the relatively small areal footprint of the work area resulted in extremely dense coverage in the centre of the study area (Figs 49 & 50). In addition, swath bathymetry data were collected during transits to each OBS and Autosub deployment and recovery positions, but not during OBS recovery itself or during Autosub deployment or recovery, as the 12 kHz outbound ping interferes with acoustic communications and monitoring of the subsurface instruments. The swath (EM120), sub-bottom profiler (SBP-120) and single beam echo sounder (EK-60) were turned off during these periods.

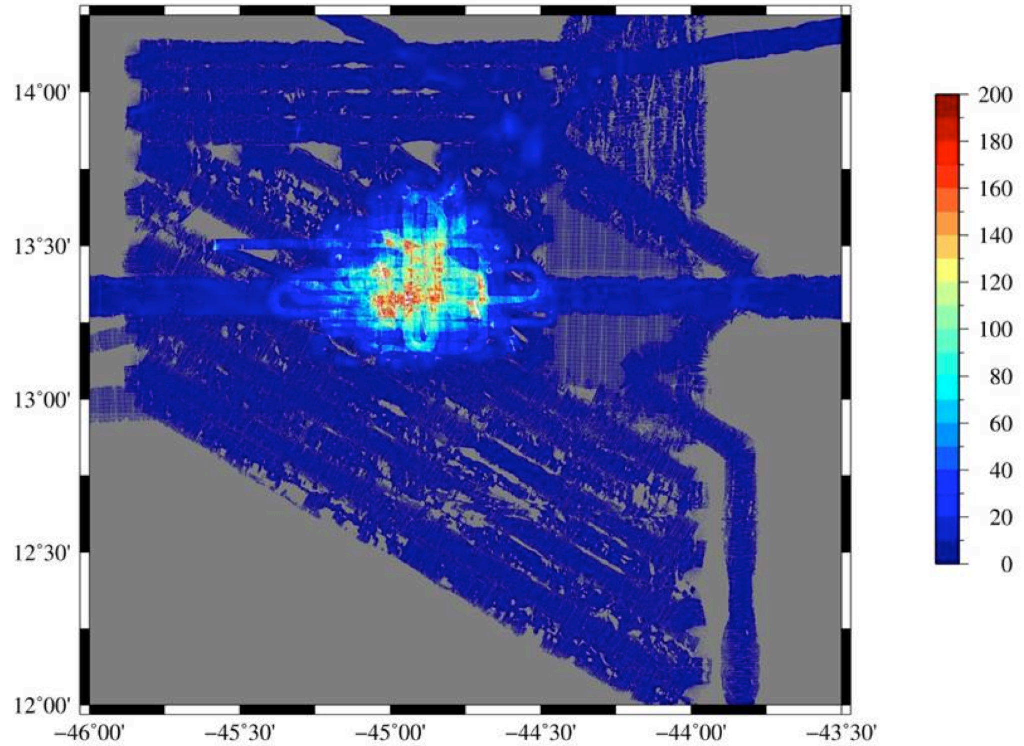

Figure 49: Comparison between swath ping density per 100 m bin in the main study area to the February 7, 2016 to that of previous datasets acquired before the series of three cruises associated with the 13N MAR project.

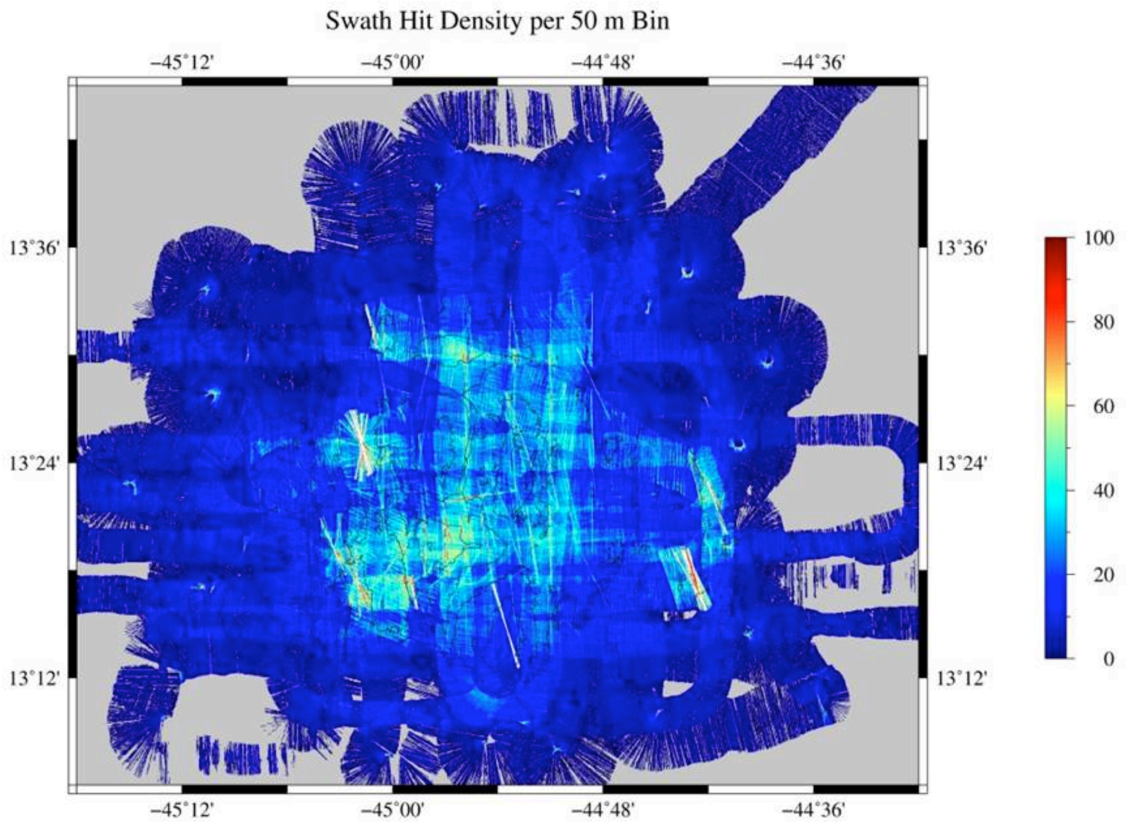

Figure 50: Swath density in the main study area. The high density of pings allows gridding at <50 m.

The high density coverage in the centre of the study area (Figs 49 & 50) results in greatly improved imaging of the seafloor (Fig. 51), allowing gridding at 40 m or less. As we used time during and between Autosub deployments and Autosub weather standby to prepare for an additional long-offset OBS/MCS profile extending south from our main area around the 1320 OCC, over the Ashadze Massif and fracture zone, we also used the transits to deploy and recover the OBSs to build up the swath coverage of the Ashadze Massif. Although not originally targeted in the proposal, this massif appears to exhibit two distinct breakaways but only one, now modified by mass-wasting, hanging-wall cut-off. The new bathymetry imaging revealed much more detail about the structure of this massif.

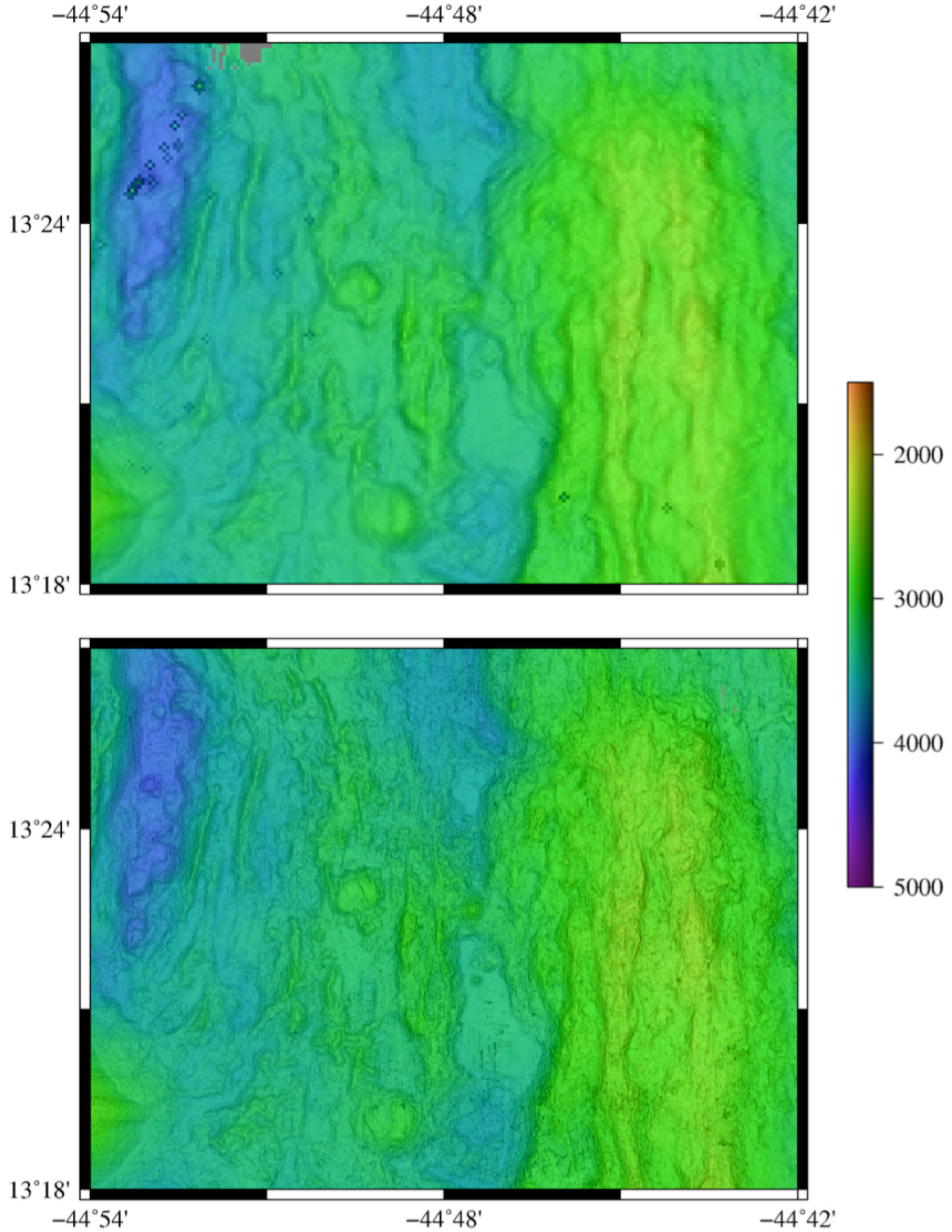

Figure 51: Comparison between old bathymetric data, gridded at 100 m (top), and new bathymetric data in the centre of the study area, gridded at 20 m (bottom), possible because of the dense and repeated ship track coverage.

3.7 Navigation

Navigation data acquired during JC132 was derived from a variety of GPS systems, both ship's fitted and attached to underpin specific instrumentation to be used during this cruise only. The data streams from the ship's fitted systems are stored in netCDF (binary) format. One of these streams is used to create the processed *bestnav*, which is supposed to be a smoothed and filtered version of a raw data stream and, thus, promoted as the navigation data to use. The data stream from the Appalanax receiver is also used as timing and position input to the gravimeter and magnetometer data-logging systems.

Although netCDF is the data format of ship's system choice, until one of the previous cruises in the 13N series (JC102) there was no on board means to unpack the netCDF to the more useful ASCII. The Ocean-Bottom Instrumentation Facility's (OBIF) software engineer wrote a conversion script during JC102, it was donated and remains in use, and was used during JC132.

During the cruise, QC of all data types was undertaken using ASCII conversions of data streams from individual GPS receivers primarily, and generally the Appalanax receiver as it is used to stamp the gravity and magnetic data. However, as the *bestnav* is cited as the best navigation product available it was used to QC first-pass process the multichannel seismic data, to create the geometry of the shot and receiver locations. The *bestnav* is also in binary format, and it is converted on board, on a daily basis, into ASCII.

During the cruise a small number of failures of the primary GPS system occurred, and this system has subsequently been replaced. The OBIF also recorded the time and position (the shot instant) of each shot fired against the reference clocks they use to set the time and measure the drift of the clocks in each OBS. Given the diversity in GPS systems on board, and the range of costs of those systems, an intellectual comparison exercise was undertaken to appraise their behaviour, and then compare them against the *bestnav* which was to be used for all post-cruise data processing.

Figs 52 & 53 show comparisons between the raw data stream from the Appalanax receiver, OBIF's three GPS reference clocks and the *bestnav*, and show that the *bestnav* has a number of issues, manifest in position, course, heading and speed. The blow-up in Fig. 53 shows the characteristics, which are essentially excursions to the numerical value 99999 and an offset of 90º between course and heading when the vessel is stationary.

A similar navigational issue with the magnetic data is demonstrated in Fig. 45, which appears to be a characteristic of the magnetic data-logging system rather than the navigational data input. In this case the magnetic data-logging system appears to free-run for a period of time, check its calculated position against a fix, and then when a threshold of mismatch is exceeded, a position reset occurs resulting in steps in the anomaly pattern if the navigation data stored in the magnetics data files is used. This data set will consequently require replacement of this navigation with whatever is created as the best navigation for JC132, as the *bestnav* is not considered usable as is.

A review of which raw navigation stream will be used to create the best navigation for JC132 will be undertaken post-cruise, and that navigation product (having been filtered and smoothed as necessary) will be used basis for processing of every data set acquired during JC132.

It would be helpful if a document outlining the specifications and characteristics of all ship's fitted systems, including the nature of what processing is applied to the data before storage, could be provided not only with the data product disk, but also stored online and made available throughout the cruise. A summary version of this document would be helpful to PI's to assist with cruise planning, and might be provided at that stage.

3.8 Autosub acquisition

The primary objective for Autosub during JC132 was to undertake a detailed micro-bathymetry survey over the 1320 OCC and its environs to aid in tectonic interpretation. In addition, detailed measurements of the near-bottom magnetic field were made in order to determine detailed spreading histories and, consequently, assess the degree of asymmetry in spreading between oceanic core complexes and inter-core-complex regions. Finally, geochemical sensors measured parameters such as Eh and turbidity to indicate the presence of any hydrothermal plumes, similar to the one observed, unusually on the 1320 OCC itself, during JC007. Prior to JC132 a French group carried out extensive AUV studies during the ODEMAR cruise in 2015. The bathymetry data produced high-quality images over parts of the 1320 OCC, and elsewhere in the local region but outside the study area of JC132. The magnetic data they recorded were disappointing.

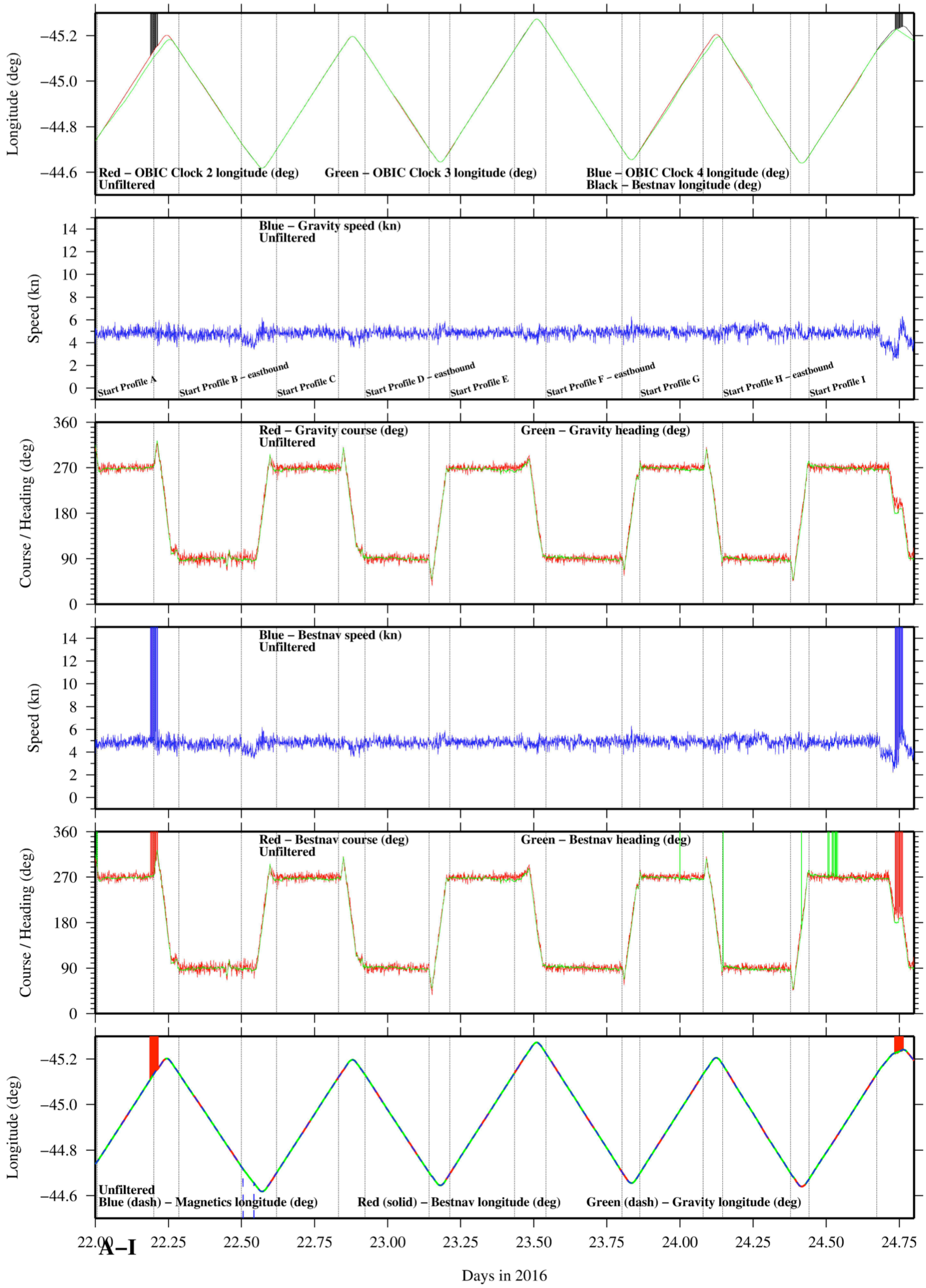

Figure 52: *Bestnav* navigation (2nd and 3rd panels up) compared with the output of the Appalanax receiver (4th and 5th panels up) used to stamp the gravity and magnetic data streams (bottom), compared with the Ocean-Bottom Instrumentation Facility's three GPS reference clocks that can also provide a location (top). Individual panels are labelled. Note in the *bestnav* the large deviations in speed, course and heading that are not apparent in any of the other navigation data. All across-axis WA profiles are plotted for comparison.

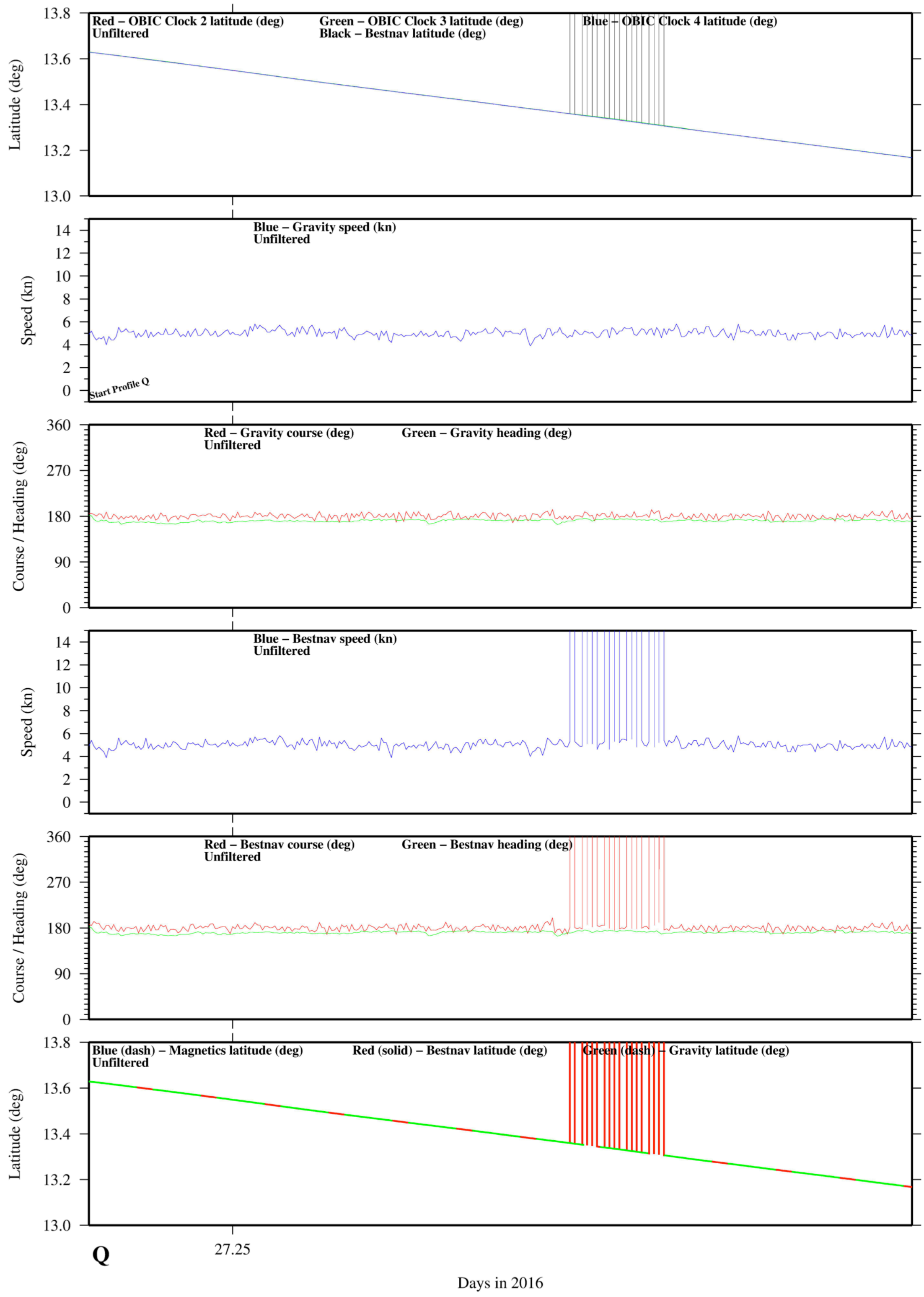

Figure 53: *Bestnav* navigation data (2nd and 3rd panels up) for southbound WA Profile Q compared with the output of the Appalanax receiver (4th and 5th panels up) used to stamp the gravity and magnetic data streams (bottom), compared with the Ocean-Bottom Instrumentation Facility's three GPS reference clocks that can also provide a location (top). Individual panels are labelled. Note in the *bestnav* the large deviations in speed, course and heading that are not apparent in any of the other navigation data.

The JC132 dive pattern was, consequently, planned to compliment the existing data and broaden the footprint around and over the 1320 OCC. Due to a series of instrumentation failures, primarily the swath bathymetry system, only dives M103 to M112 from the pre-cruise plan were completed. The dives are summarised in Appendix 5.

Dives M103 to M106 were designed to extend east-west between the likely positions of the Jaramillo anomaly (0.99 – 1.07 Ma, 13 km off-axis). M103 was located in the centre of the 1320 OCC, while M104 and the northern leg of M105 were located in the inter-OCC region between the 1320 OCC and the 1330 OCC to the north. Part of M106 and all remaining dives were designed to provide high-resolution bathymetry, and denser magnetic coverage over and around the1320 OCC.

The bathymetry data acquired during dives M103 to M106 showed that Autosub could not reliably keep within acoustic contact of the seafloor along east-west tracks (along strike to the ridge-related topography), so subsequent dives had to be redesigned to run as parallel to the topography (ridge-parallel) as possible.

Dives M103 and M104 were programmed for a nominal 150 m height above the seafloor. The acquired swath coverage was poor in extent, and so different vehicle survey altitudes were programmed for subsequent dives in the hope of improving the multi-beam coverage. M105 to M109 were programmed at 120 m, and 115 m programmed for M110 to M112. The result was that dives with grids track 500 m apart, which should have provided overlapping bathymetric coverage, have gaps in data coverage in between. In practice, swath widths of between 250 m and (very rarely) 600 m, and mostly around 400 m, were achieved. This meant that dive programmes needed to have track lines closer together and, consequenty, that smaller areas of coverage could only be obtained during each dive, as total dive duration is determined by maximum battery life.

Autosub's position during each dive was estimated by ADCP (Acoustic Doppler Current Profiler) bottom tracking, initialised to GPS fixes whilst the vehicle was at the surface at dive start. The dead-reckoning position was updated from USBL (ultra-short baseline) acoustic fixes sent from the vessel once Autosub reached the vicinity of the bottom. Throughout each dive, the vehicle depth was measured using its depth sensor, and its altitude above seabed was measured when the vehicle was within range of the bottom.

Figure 54: Magnetometer mounted athwartships in Autosub's nose, with red connector on left, attached to the frame, middle-top.

3.8.1 Magnetic data

Autosub is fitted with an Applied Physics Systems model 1540 24-bit digital three-axis miniature fluxgate magnetometer, mounted in the nose (Fig. 54). The data are internally calibrated within the unit itself and output in Gauss. The three magnetic field components were logged, together with other data, at the common interval of 0.4 s and, additionally by scientific request, at 0.2 s. The three axes are orthogonal but are not aligned with Autosub or its attitude sensor axes, due to where and how the magnetometer is mounted. Consequently, all data acquired needs to be first corrected to the vehicle alignment, and then corrected to the track orientation relative to the ridge-axis to be usable. Moreover, the magnetometer was also removed and replaced between dives M106 and M107 to access the EM2040, but was not precisely re-aligned to its original position. The magnetic data acquired during dive sets M103 to M105 and M106 to M112 are therefore not directly comparable, since the exact alignment of the sensor axes was not recorded before removal or after reinstatement to allow correction to be made. 'Figure of eight' calibration turns were made at 1000 m depth on all dives during the vehicle's descent and ascent, for all dives except M104, M105, M108, and M111. Additional circles (at the same depth) with strong pitching were also conducted on dives M107, M109, M110 and M112.

Despite sensor alignment and orientation issues, the magnetometer apparently worked well throughout the cruise and recorded data throughout all the dives. However, the data contained a large number of spikes and some major instantaneous offsets (~1000 nT) whose origins are still being examined. Nevertheless, major anomalies can be seen, they are robust and identifiable in age terms, and appear to be adequate for the purposes of geophysical interpretation and determination of spreading rate.

The three magnetic components were initially combined into the total magnetic field that clearly shows large variations, apparently correlated with heading (Fig. 55). To remove these, we analysed the 'figure-of-eight' data (Fig. 56). Plotting total magnetic field against heading shows variation ~ 6000 nT. We removed most of this by fitting a two-term sine function, leaving a small ($\pm$200 nT) variation that is roughly linearly correlated with pitch. This was also removed by de-linear trending the data, and only slightly affects the amplitude of the total magnetic variation, at just under $\pm$200 nT, similar to the reductions achieved using the Isezaki matrix correction method. All 'figure-of-eights' were analysed, and the variations of the parameters between them were mostly within expected statistical fluctuation. We applied the values from each descending turn to its own dive. So far we have not considered corrections based on the ascending 'figure-of-eights', although they will be considered during post-cruise processing.

Once these corrections for heading and pitch had been made, most of the large variations in the observed field were removed. However, there remained two issues. The first is on dive M105, where a sudden decrease in the total field of 23701 nT occurred at sample 36207 (January 29, 2016, 09:22:42 UTC). At the following sample the field returned to its previous level, and then on the next sample (36210) it again fell by 24558 nT and retained this offset for the rest of the dive. It is believed that this may have been associated with the EM2040 echo sounder switching off, although that event was logged slightly later at 09:23:20 UTC. A 'correction' of 24558 nT has had to be added to all samples from 36210 onwards and to sample 36208, which is far from ideal.

The second set of jumps occurred on dive M106. There is one, at sample 26048 (January 30, 2016, 21:58:00 UTC, +2783 nT) that is instantaneous. This correlates exactly with a switch-off of the EM2040. Subsequent values of total field were adjusted as described above for M105. The other 'jumps' on dive M106 all occur at course changes, and are clearly places where the heading correction described above has failed. We do not know the cause of these jumps, and they have not been observed on any other dive. These jumps were all 'fixed' by adjusting the subsequent samples for the value of each jump.

Finally, prior to plotting, the corrected values of total magnetic field for each dive were normalised by subtracting the mean corrected value for the time the vehicle was near the ocean bottom during that dive. Fig. 57 shows the anomaly patterns along track.

A set of positive anomalies are observed at the eastern edge of the work area (around 44º42'W to 44º46'W), which are possible candidates for the Jaramillo anomaly. A possible Brunhes anomaly (0.78 Ma, +/-10 km) is harder to define. When measured this close to the seafloor, a sharp peak on its eastern side and a sharp trough on its western margin would be expected as shown by modelling (Fig. 58). There are high-amplitude positive anomalies at the right position east of the 1320 OCC, but not clearly elsewhere. Similarly, there are troughs to the west of the 1320 OCC, but only a confused pattern elsewhere. Perhaps the most obvious feature is the very low amplitude of the anomalies over the smooth dome of the 1320 OCC itself, coupled with the ring of high amplitude anomalies surrounding it. Such low-amplitude anomalies could reflect low magnetisation in the smooth dome, perhaps indicating a dominant gabbroic (or possibly serpentinite) lithology.

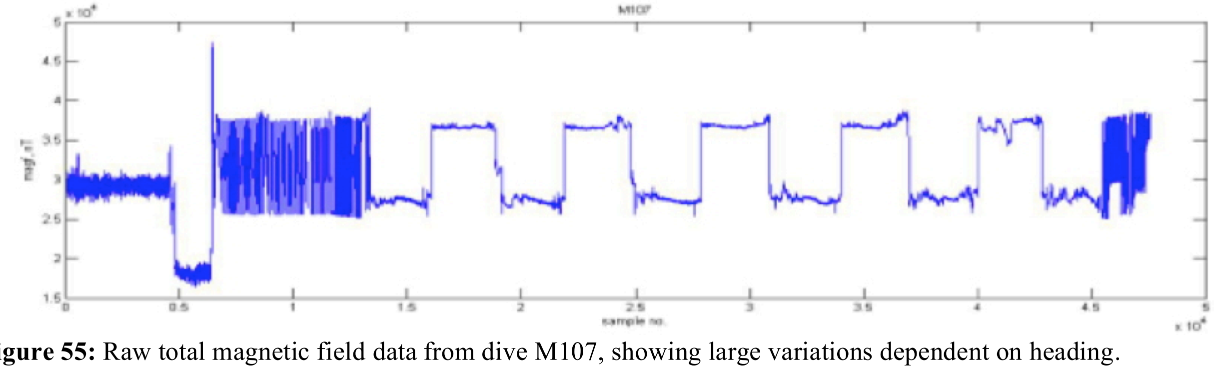

Figure 55: Raw total magnetic field data from dive M107, showing large variations dependent on heading.

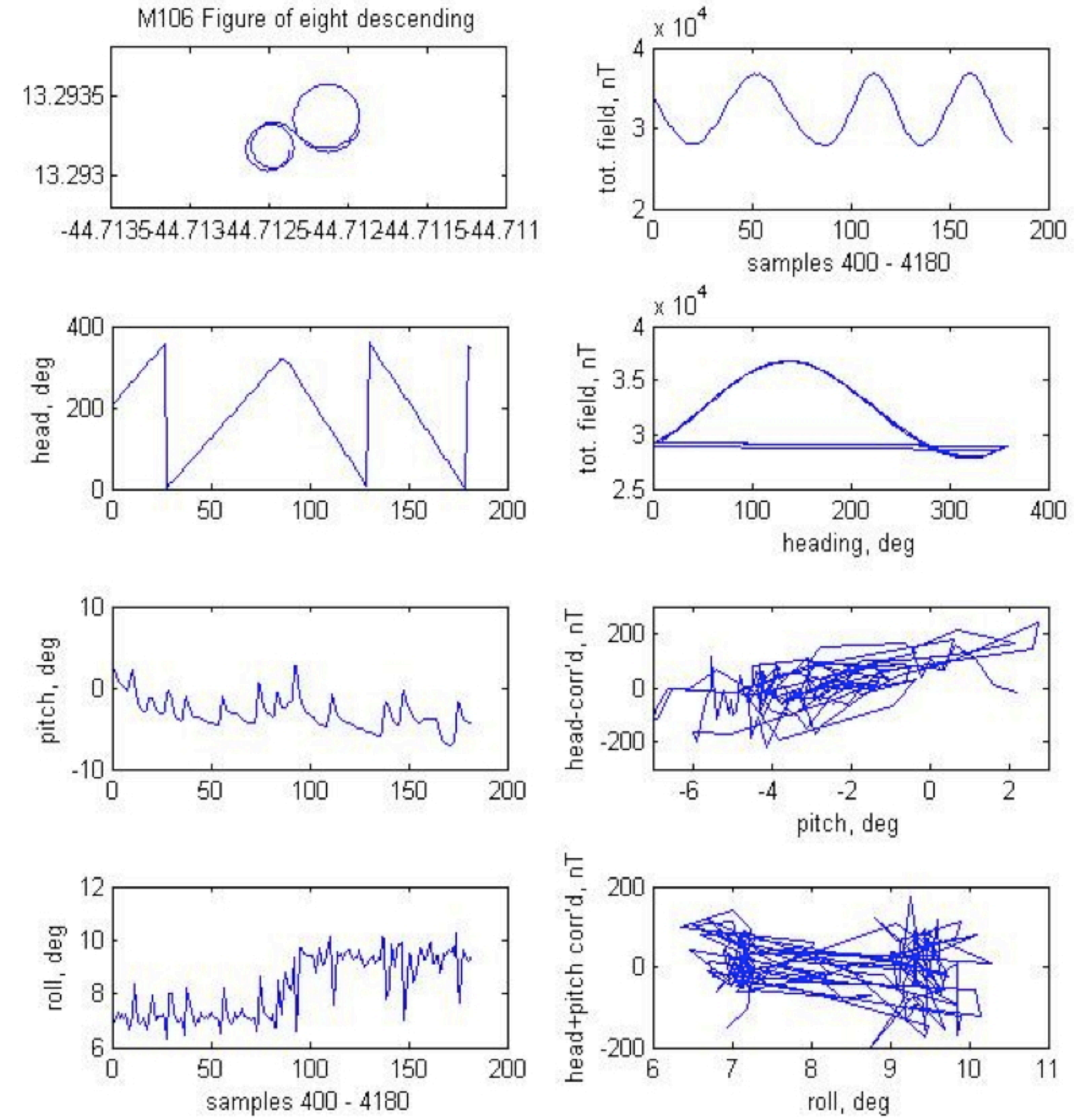

Figure 56: Analysis of the descending 'figure-of-eight' turns for M106.

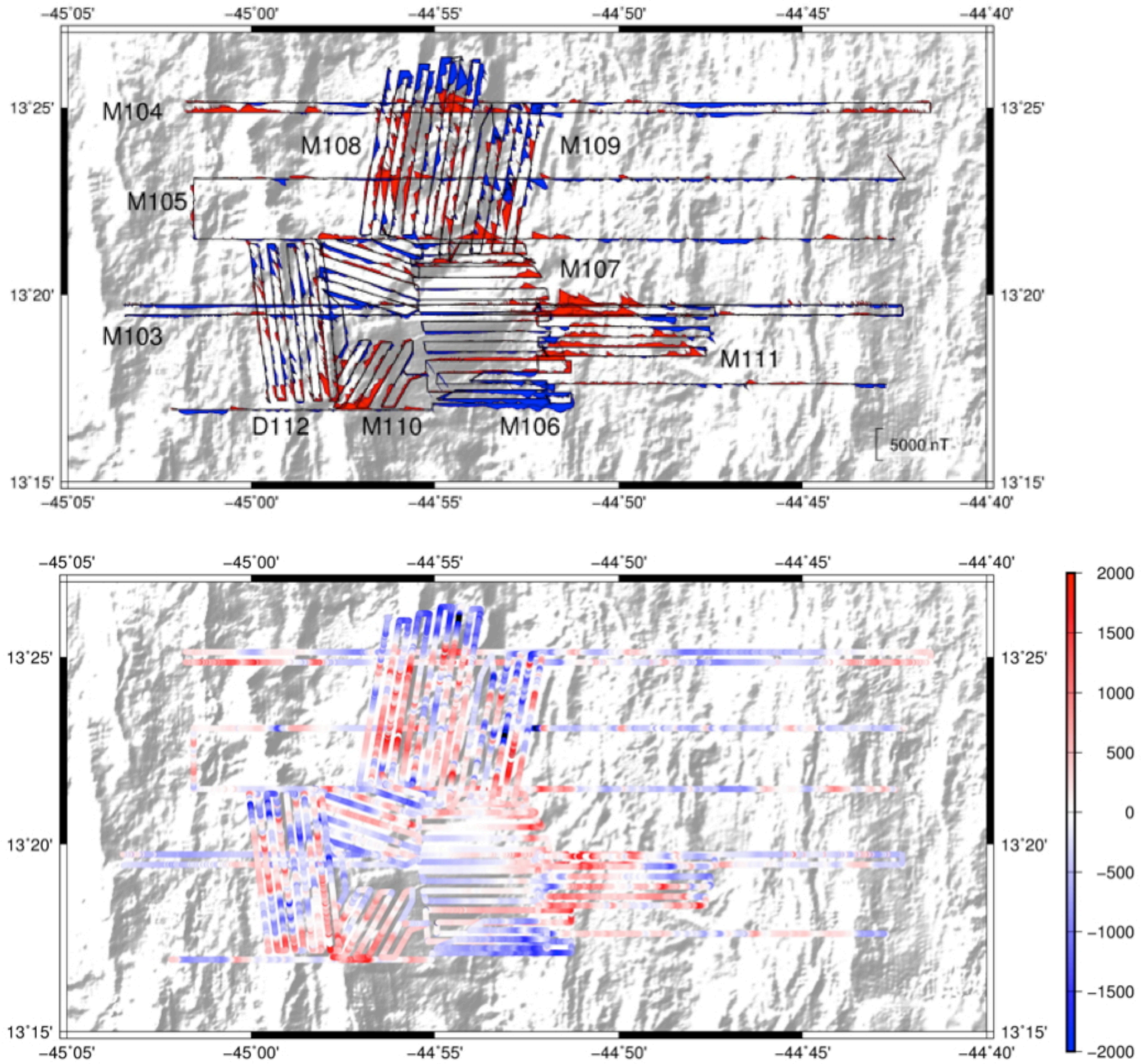

Figure 57: Preliminary plots of total magnetic field anomaly along track (nT). Top – wiggle display. Bottom – polarity display.

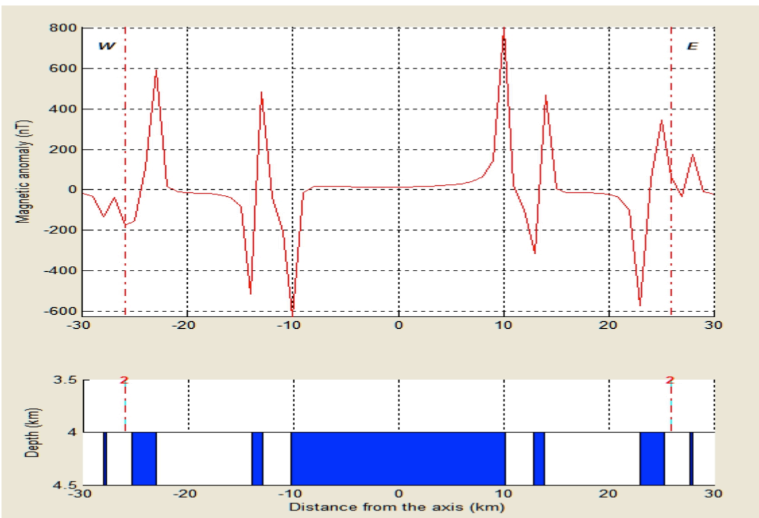

Figure 58: Modelled total magnetic field (red line) for observations 150 m above a crust magnetised according to the reversal model in blue.

3.8.2 Bathymetry data

Swath bathymetry data were acquired with an EM2040 multi-beam echo sounder during dives M103 and M107 to M112. The raw data from these dives had to be first “re-navigated” by matching up common features on neighbouring or overlapping swathes, rather using the Autosub navigation data itself as should be the case, and then these swathes matched to the same bathymetric features imaged with the vessel’s swath system to locate them absolutely in latitude and longitude. This absolute location process was undertaken using the multi-pass over the same seabed, <50 m node-spacing swath grid achieved using the combined dataset from JC007, JC102, JC109 and JC132.

An ~700 m mismatch in Autosub location between swathes was observed, in swath widths of ~ 400 m on average. The location adjusted data were then gridded with a node spacing of 4 m. All acquired data are shown in Fig. 59. An indication of the resolution achieved is demonstrated in the zoom-in shown in Fig. 60.

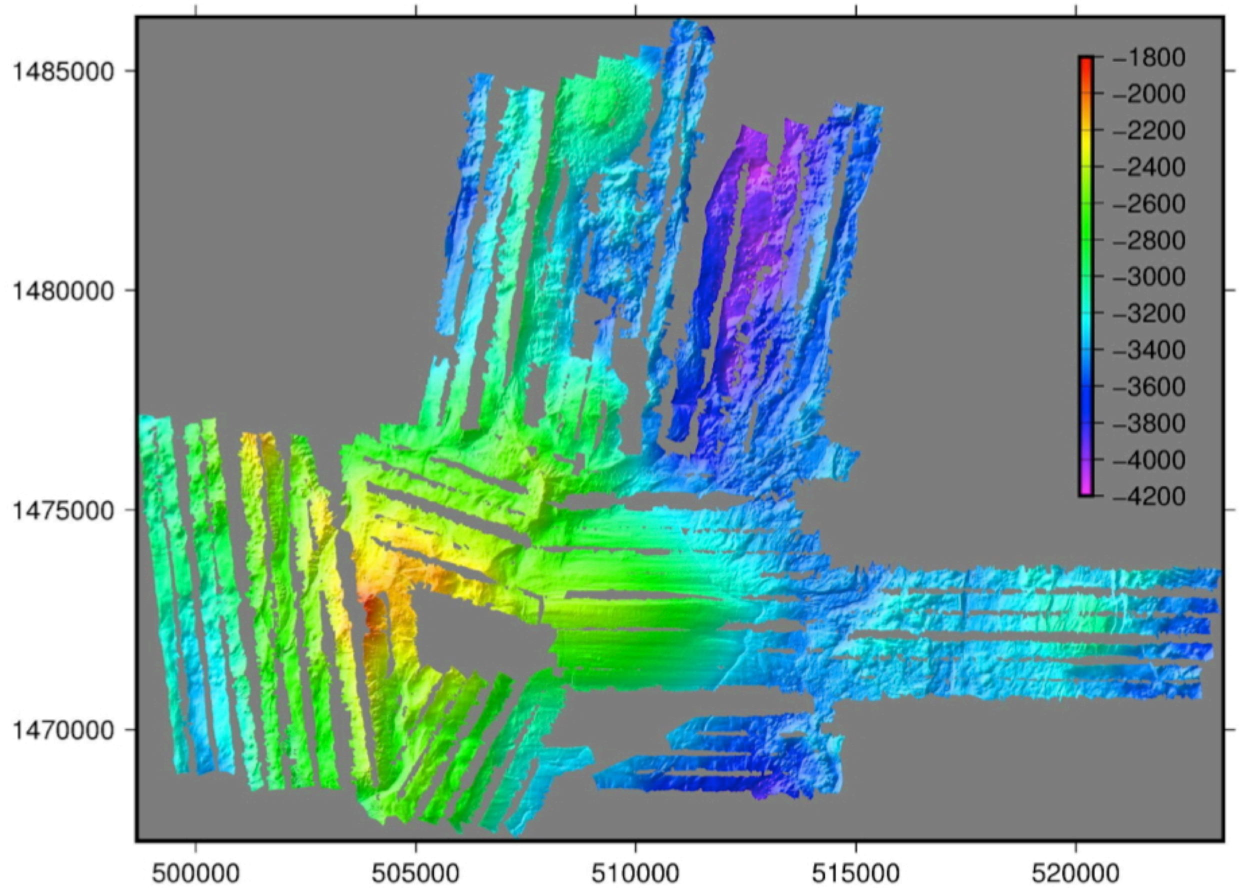

Figure 59: Re-navigated Autosub EM2040 data from the vicinity of the 1320 OCC. Note the large gaps between the individual swathes due to a combination of Autosub system navigation and Autosub swath data coverage issues.

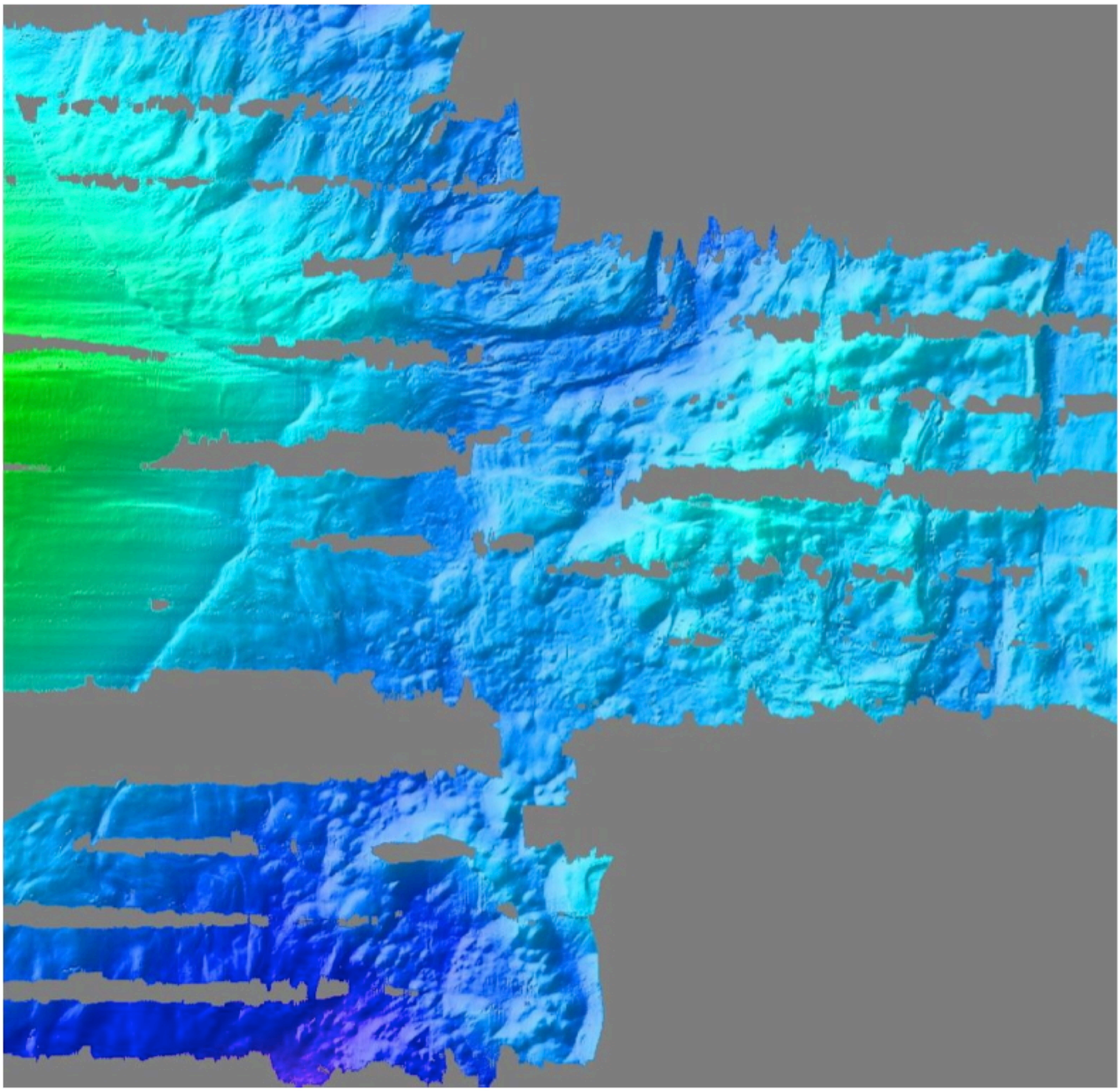

Figure 60: Detail of the re-navigated Autosub EM2040 bathymetry. Note the large gaps between the individual swathes due to a combination of Autosub system navigation and Autosub swath data coverage issues.

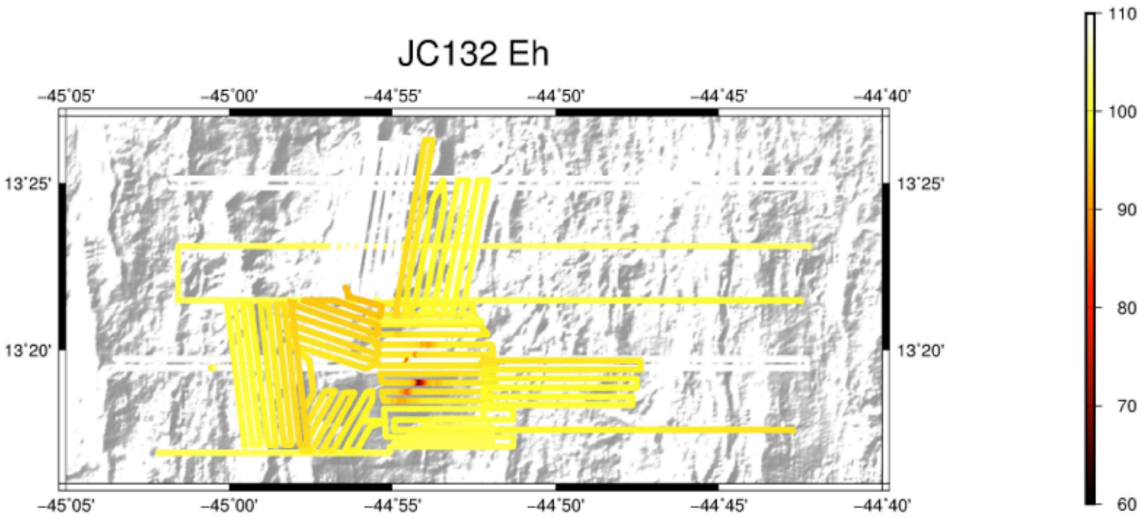

Figure 61: Plot of redox potential Eh (V) across the 1320 OCC dome acquired during M103 and M107.

3.8.3 Water column data

Autosub carried a CTD measuring temperature, depth and salinity, and a water turbidity meter supplemented these. It also carried an Eh meter supplied by Dr. Ko-ichi Nakamura of the National Institute for Industrial Science and Technology, Japan. We used the Eh and turbidity measurements to investigate the presence of hydrothermal plumes. A cluster of signals were observed over the 1320 OCC dome during M103 and M107, all apparently from the previously known Irinovskoe vent site (Fig. 61). No other signals were observed.

3.8.4 Sidescan sonar and sub-bottom profiler data

Autosub was also fitted with an Edgetech 200 kHz sidescan sonar and chirp sub-bottom profiler. These instruments were run during dive M105 but not the subsequent dives, because of suspected interference with the EM2040. The data were only available in a proprietary format (.jsf or Jstar), and as we had not been advised of this we did not have the capability on board to examine this data, or software to convert it into a more useful and usable data format. A far better approach would be to not use a proprietary format for a data product at all, and instead as part of the acquisition process convert it to something standard (e.g. ASCII, or netCDF grid format) that software available in the public domain can read.

4. Cruise narrative

The duration of the cruise was 42 days and 6 hours. Of this, ~10 days were spent on passage to and from port calls to the work area, leaving a total of ~32 days in the work area. Of the latter ~ 6 days were dedicated to MCS acquisition (including streamer and airgun array deployment and recovery and repairs), with all shots also recorded by OBSs, 6 days of shooting solely into OBSs, and ~6 days for OBS deployment (2) and recovery (4). All OBS deployments and recoveries were interleaved with Autosub deployments and recoveries so that OBS work took place during Autosub surveys and during Autosub turnaround recharging time.

The sequence of acquisition was partly planned and partly determined by events and weather. It was initially planned to interleave more Autosub deployments during OBS deployments but the speed of OBS deployment meant that the OBSs were all deployed ahead of schedule.

As the weather conditions were considered borderline for deployment by the Autosub team, it was decided to shoot the wide-angle survey. Two more Autosub deployments were completed after this survey (M105 and M106), but on-going problems with the Autosub multi-beam bathymetry system meant that these were focused on magnetics only, and further Autosub deployments were delayed until the problem was resolved.

As a result, MCS deployment was moved up the schedule. During the MCS shooting the problem with the Autosub multi-beam bathymetry was identified and fixed. After recovery of the MCS instrumentation, a fifth Autosub deployment (M106 – dive 4 in the original plan) was carried out and OBS recovery begun. Two more Autosub deployments (M107 and M108 – dives 6 and 7) were completed interleaved with OBS recovery but a planned 8th dive (M109) was delayed by poor weather.

Four OBSs had been deliberately left deployed to facilitate the possibility of a north-south long seismic profile, and five more OBSs were re-deployed when weather delayed deployment of Autosub for dive 8 (M109) and a further five during Autosub dive 8. An additional 190 km long wide-angle profile was acquired at 60 s shot interval over these 14 instruments between Autosub dives M109 and M110 (8 and 9), when a moderate swell temporarily precluded Autosub deployment.

As it was too late on February 14, 2016 to deploy the airguns and start shooting before nightfall, and as we wished to be close to the next Autosub deployment (weather permitting) at the end of the profile, we decided to begin Profile R in the south and so transited there in the night of the February 14, 2016. Streamer and airgun deployment started before daybreak and the full airgun array was firing just over one hour after daybreak, following the JNCC regulations. The streamer data were recorded with a trace length of 45 s to monitor noise and multiples as well as crustal structure. After airgun array and streamer recovery at the north end of Profile R, the two remaining Autosub dives (M110 and M112) were then interleaved with the recovery of the 14 OBSs, with both completed on February 19, 2016. The remaining cruise science time was used to fill in gaps in the existing swath coverage before setting course for Port of Spain on Saturday February 20, 2016 at 17:00 UTC.

JD	Date	Main Activity
14	14 Jan, 2016	Depart Mindelo.
15	15 Jan, 2016	SVP and 4 acoustic release dip tests; Autosub beacon test.
16	16 Jan, 2016	Autosub test deployment 101. Transit.
17	17 Jan, 2016	Transit to work area.
18	18 Jan, 2016	Transit to work area.
19	19 Jan, 2016	Autosub 102 deployment, recovery. OBS BB test deployments (4 instruments). Autosub 103 deployment.
20	20 Jan, 2016	Recover 4 BB OBS. Recover Autosub 103, Standard OBS deployment.
21	21 Jan, 2016	Deploy Autosub 104. Continue OBS deployment.
22	22 Jan, 2016	Recover Autosub 104. Begin OBS shooting at 16:30 UTC.
23	23 Jan, 2016	OBS shooting.
24	24 Jan, 2016	OBS shooting.
25	25 Jan, 2016	OBS shooting.
26	26 Jan, 2016	OBS shooting.
27	27 Jan, 2016	OBS shooting.
28	28 Jan, 2016	OBS shooting, until 13:00. UTC Autosub Deployment 105.
29	29 Jan, 2016	Recovery 4 OBS. Deployment of 8 OBS. Autosub 105 recovery.
30	30 Jan, 2016	Autosub 106 launch. Magnetometer test.
31	31 Jan, 2016	Autosub 106 recovery. Deployment of streamer and guns. Start shooting at 15:30 UTC.
32	1 Feb, 2016	Shooting MCS.
33	2 Feb, 2016	Shooting MCS.
34	3 Feb, 2016	Shooting MCS.
35	4 Feb, 2016	Shooting MCS.
36	5 Feb, 2016	Shooting MCS.
37	6 Feb, 2016	Finish shooting MCS. Autosub 107 launch. OBS recovery.
38	7 Feb, 2016	OBS recovery. Autosub 107 recovery.
39	8 Feb, 2016	OBS recovery. Autosub 108 launch.
40	9 Feb, 2016	OBS recovery. Autosub 108 recovery.
41	10 Feb, 2016	OBS recovery, Autosub 109 launch.
42	11 Feb, 2016	OBS recovery. Autosub 109 recovery.
43	12 Feb, 2016	OBS redeployment (61-65), swath-bathymetry of Ashadze Massif.
44	13 Feb, 2016	Autosub deployment 110. Transit swath and redeployment of OBS (66-70).
45	14 Feb, 2016	Autosub recovery 110. Transit and swath to beginning of WA Profile R.
46	15 Feb, 2016	Deploy streamer and guns. Start collection of Profile R.
47	16 Feb, 2016	Complete Profile R. Deploy Autosub 111. Recover OBS.
48	17 Feb, 2016	Recover OBS. Recover Autosub 111.
49	18 Feb, 2016	Recover OBS, Deploy Autosub 112, Swath, recover OBS.
50	19 Feb, 2016	Recover last OBS, Recover Autosub 112. Swath.
51	20 Feb, 2016	Swath. Transit to Port of Spain.
52	21 Feb, 2016	Transit to Port of Spain.
53	22 Feb, 2016	Transit to Port of Spain.
54	23 Feb, 2016	Transit to Port of Spain.
55	24 Feb, 2016	Arrival in Port of Spain.

5. Demobilisation

A five-day period of demobilisation was planned for arrival in Port of Spain (Trinidad). The entire multichannel seismic system was dismantled prior to arrival and simply required packing into shipping containers for sea freight back to the UK. Parts of this system, hired from Exploration Electronics Ltd, would return to the UK on the *RRS James Cook*, and these were packed into boxes and crates and stored in the hold. The multichannel streamer and winch would return to the UK in the same manner, and were left on the stern working deck and covered with a tarpaulin to protect the streamer sections from the sun.

Similarly, all instrumentation and lab-based equipment from the OBIF were packed and ready for loading into OBIF's own sea freight shipping containers on arrival in port. These containers had been stored, since departure of the *RRS James Cook* from Southampton in December, on the Mezzanine deck and were thus not accessible at sea. Consequently, the day after arrival and once some space had been created on the stern working deck, these containers were relocated from the Mezzanine and packed. Once packed, they were returned to their Mezzanine storage location for return to the UK on the *RRS James Cook*.

The re-establishment of an absolute gravity station was also undertaken during the port call. Apart from a minor adjustment immediately after installation, the meter functioned without issue and measurements were taken over a period of two days. We planned to take measurements for five days given the inherent background vibrational noise revealed after installation, due to its location near the port and near a busy road. However, the *RRS James Cook* had experienced failure of one of its rudder's a few days before departure from the work area, and plans were being made for repairs that could involve early departure from Port of Spain for a dry dock elsewhere in the Caribbean. Consequently, the measurement period had to be curtailed to the minimum required to achieve the necessary accuracy, rather than the ideal period required to achieve the optimum accuracy, which is what had been planned. The temporary relative station established at the Customs House during JC102, and revisited during JC109, was tied to this newly established absolute base station. In this way the gravity data from all three cruises to the 13N work area can now be tied to an absolute gravity base station, at both the beginning and end of each cruise, and the data jointly analysed, creating quite dense coverage in the 13N work area.

Acknowledgements

We would like to thank the master, deck officers, engineers and crew of the *RRS James Cook* and the support staff and sea-going technicians of NERC's National Marine Facility (NMF) and NERC's Ocean-Bottom Instrumentation Facility (OBIF) for their efforts and good humour throughout a long, complex and crowded cruise. The U.K.'s Natural Environment Research Council, standard grant numbers NE/J02029X/1, NE/J022551/1 and NE/J021741/1, funded this research. In particular we would like to thank the Cruise Manager Jon Short, Vicki Smith from the SGF for travelling to Port of Spain and operating the absolute gravity meter, and Mark Maltby and Juan Ward from NMF Platform System Group for assisting her, and for taking great care of the meter during its long transit from the UK.

References

Baines, G.B., et al., 2008. *EPSL*, **273,** 105-114**.**
Buck, W.R., et al., 2005. *Nature,* **434**, 719-723
Bullard, E.C., & R.G. Mason, 1961, *Deep-Sea Research*, *8*, 20-27.
Canales, J.P., et al., 2008. *G^3,* **9**, Q08002
Cann, J.R. et al., 1997. *Nature,* **385**, 329-332
Cannat, M., et al., 2010. *AGU Geophys. Mono. Series,* **188**, 241-264.
Connelly, D., et al., 2011. *Nature Comms*., **3**, 620.
deMartin, B, et al., 2007. *Geology*, **35**, 711-714.
Dick, H.J.B., et al., 2008. *G^3*, **9**, Q05014.
Escartin, J. et al., 2008. *Nature,* **455**, 790-795.
Escartin, J & Canales, J-P, 2011, *EOS Trans. AGU* ***92***(4), 31-32.
Grimes, C.B., et al. 2008. *G^3*, **9**, Q08012.
Ildefonse, B., et al., 2007. *Geology,* **35**, 623–626.
Isezaki, N., 1986, *Geophysics*, *51*, 1992-1998.
Lavier, L.L., et al., 1999. *Geology*, **27**, 1127-1130.
MacLeod, C.J., et al., 2002. *Geology,* **30**, 879-882.
MacLeod, C.J., et al., 2009. *EPSL,* **287**, 333-344.
MacLeod, C.J., et al., 2011. *G^3*, 12, Q0AG03.
Mallows C. & Searle R., 2012, *G^3*, **13**, Q0AG08.
Mallows, C. 2011. Unpubl PhD thesis, U. Durham
Mendel, V. et al., 2005, *Computers & Geosciences*, *31*(5), 589-597.
Morris, A., et al., 2009. *EPSL*, **287**, 217–228.
Okino, K., et al., 2004. *G^3*, 5, Q12012.
Olive, J.A., et al., 2010. *Nature Geoscience***, 3,** 491-195.
Peirce, C. & Day, A.J., 2002. *Geophys. J. Int*., **151**, 2, 543-566.
Reston, T.J. & Ranero, C.R. 2011 *G^3*, **12**, Q0AG05..
Reston TJ et al., 1999. *JGR*, **104**, 629-644.
Schouten, H., et al., 2010. *Geology,* **38**, 615-618.
Searle, R. C. et al., 2003. *G^3*, **4**, 9105, doi:10.1029/2003GC000519.
Searle, R.C., et al., 2007. RRS James Cook Cruise JC007: Cruise Report, Durham University, 59pp.
Searle, R. C., et al., 2008, RRS James Cook Cruise JC024: Cruise Report, Durham University, 134pp.
Smith, D.K., et al., 2008. *G^3,* **9**, Q03003
Tucholke, B.E. & Lin, J., 1994. *JGR*, **99**, 11,937-11,958.
Tucholke, B.E., et al., 1998. *JGR,* **103**, 9857- 9866.
Tucholke, B.E., et al., 2008. *Geology,* **36**, 455-4

Appendix 1: Framework waypoints

Survey	Latitude (N)	Longitude (W)
Transit inT1	14° 04.314’	44° 20.500’
T2	14° 00.000’	44° 21.600’
Ashadze Chevrons	12° 55.000’	44° 50.000’
Feb 12 – Feb 13	13° 05.000’	45° 00.000’
waiting for calmer	12° 58.000’	45° 05.000’
seas for Autosub dive M110	12° 58.000’	44° 50.000’
	13° 08.000’	45° 00.000’
	13° 01.000’	45° 05.000’
Transit to beginning of	13° 10.000’	44° 55.000’
Profile R, Feb 14 – Feb 15	12° 50.000’	44° 55.000’
	12° 30.000’	44° 55.000’
	12° 24.500’	44° 58.200’
	12° 20.250’	44° 58.200’
	12° 04.060’	44° 58.200’
	12° 04.060’	45° 01.200’
	12° 34.000’	45° 01.200’
	12° 34.000’	45° 04.200’
	12° 04.060’	45° 04.200’
	11° 50.000’	45° 27.000’
Transit south to pick up	13° 15.000’	45° 01.000’
OBSs 67-70, Feb 17	12° 29.000’	45° 01.000’
Transit south to pick up	13° 15.000’	44° 51.000’
OBSs 63-66, Feb 18	12° 50.000’	44° 51.000’
Transit out of area	13° 10.000’	45° 04.000’
Feb 19 – Feb 20	13° 10.000’	45° 04.000’
	12° 30.700’	45° 01.000’
	12° 03.700’	45° 01.000’
	12° 03.700’	44° 53.800’
	12° 16.000’	44° 53.800’
	12° 26.000’	44° 54.400’
	12° 26.000’	45° 07.500’
	12° 36.000’	45° 07.500’
	12° 36.000’	45° 11.000’
	12° 25.500’	45° 11.000’
	12° 25.500’	45° 14.500’
	12° 38.000’	45° 14.500’
	12° 38.000’	45° 18.000’
	12° 25.000’	45° 18.000’
	12° 25.000’	45° 27.500’
	12° 30.000’	45° 27.500’
	12° 30.500’	45° 30.500’
	12° 45.500’	45° 30.500’
	12° 45.500’	45° 39.500’
	12° 38.500’	45° 39.500’
	12° 38.500’	45° 42.500’
	12° 50.500’	45° 42.500’
	12° 50.500’	45° 46.200’
	12° 41.500’	45° 46.200’
	12° 41.500’	45° 50.500’
	12° 47.500’	45° 50.500’
Trinidad-Barbados Border	12° 19.600’	60° 16.600’

Appendix 2: OBS locations

OBS No.	Latitude (N)	Longitude (W)	Depth (m)	Latitude (Deg)	N (Min)	Longitude (Deg)	W (Min)	Longitude (Deg)	E (Min)	Longitude E (Deg)
FRANK	13.2917	45.0333	2869	13	17.504	45	02.000	314	58.000	314.9667
BB001	13.2874	45.0333	2889	13	17.241	45	01.999	314	58.001	314.9667
BB002	13.2827	45.0333	2821	13	16.963	45	01.998	314	58.002	314.9667
Grid										
OBS_WA_1	13.4754	45.0091	2884	13	28.521	45	00.547	314	59.453	314.9909
OBS_WA_2	13.4299	45.0091	3221	13	25.794	45	00.547	314	59.453	314.9909
OBS_WA_3	13.3895	45.0094	2847	13	23.371	45	00.561	314	59.439	314.9907
OBS_WA_4	13.3490	45.0092	3020	13	20.940	45	00.550	314	59.450	314.9908
OBS_WA_5	13.2953	45.0093	3111	13	17.720	45	00.560	314	59.440	314.9907
OBS_WA_6	13.5247	44.9703	2690	13	31.480	44	58.220	315	01.780	315.0297
OBS_WA_7	13.4748	44.9704	2798	13	28.490	44	58.223	315	01.777	315.0296
OBS_WA_8	13.4300	44.9703	3635	13	25.797	44	58.219	315	01.781	315.0297
OBS_WA_9	13.3898	44.9707	3518	13	23.387	44	58.241	315	01.759	315.0293
OBS_WA_10	13.3492	44.9698	2564	13	20.950	44	58.190	315	01.810	315.0302
OBS_WA_11	13.3222	44.9702	2259	13	19.330	44	58.210	315	01.790	315.0298
OBS_WA_12	13.2955	44.9707	3039	13	17.730	44	58.240	315	01.760	315.0293
OBS_WA_13	13.2593	44.9703	3426	13	15.557	44	58.216	315	01.784	315.0297
OBS_WA_14	13.3493	44.9497	2592	13	20.960	44	56.980	315	03.020	315.0503
OBS_WA_15	13.3222	44.9500	2131	13	19.330	44	57.000	315	03.000	315.0500
OBS_WA_16	13.2953	44.9498	2587	13	17.720	44	56.990	315	03.010	315.0502
OBS_WA_17	13.5252	44.9308	2806	13	31.510	44	55.850	315	04.150	315.0692
OBS_WA_18	13.4750	44.9304	2865	13	28.502	44	55.825	315	04.175	315.0696
OBS_WA_19	13.4300	44.9307	3252	13	25.802	44	55.839	315	04.161	315.0694
OBS_WA_20	13.3897	44.9308	3042	13	23.383	44	55.847	315	04.153	315.0692
OBS_WA_21	13.3490	44.9303	2555	13	20.940	44	55.820	315	04.180	315.0697
OBS_WA_22	13.3222	44.9305	2492	13	19.330	44	55.830	315	04.170	315.0695
OBS_WA_23	13.2952	44.9307	3296	13	17.710	44	55.840	315	04.160	315.0693
OBS_WA_24	13.2591	44.9306	3665	13	15.548	44	55.838	315	04.162	315.0694
OBS_WA_25	13.3490	44.9100	3059	13	20.940	44	54.600	315	05.400	315.0900
OBS_WA_26	13.3222	44.9102	2550	13	19.330	44	54.610	315	05.390	315.0898
OBS_WA_27	13.2953	44.9104	3311	13	17.715	44	54.621	315	05.379	315.0897
OBS_WA_28	13.5247	44.8845	2957	13	31.483	44	53.067	315	06.933	315.1156

OBS_WA_29	13.4750	44.8843	3326		13	28.501	44	53.058		315	06.942		315.1157
OBS_WA_30	13.4302	44.8846	3933		13	25.813	44	53.075		315	06.925		315.1154
OBS_WA_31	13.3899	44.8840	3947		13	23.393	44	53.040		315	06.960		315.1160
OBS_WA_32	13.3492	44.8842	3474		13	20.950	44	53.050		315	06.950		315.1158
OBS_WA_33	13.3223	44.8843	3072		13	19.340	44	53.060		315	06.940		315.1157
OBS_WA_34	13.2952	44.8843	3586		13	17.711	44	53.057		315	06.943		315.1157
OBS_WA_35	13.2593	44.8845	4018		13	15.559	44	53.067		315	06.933		315.1156
OBS_WA_36	13.3222	44.8670	3482		13	19.334	44	52.017		315	07.983		315.1331
OBS_WA_37	13.2952	44.8670	3339		13	17.713	44	52.021		315	07.979		315.1330
OBS_WA_38	13.5245	44.8503	3185		13	31.472	44	51.015		315	08.985		315.1498
OBS_WA_39	13.4750	44.8501	3023		13	28.501	44	51.005		315	08.995		315.1499
OBS_WA_40	13.4302	44.8503	3433		13	25.814	44	51.019		315	08.981		315.1497
OBS_WA_41	13.3902	44.8502	3611		13	23.409	44	51.014		315	08.986		315.1498
OBS_WA_42	13.3491	44.8504	3372		13	20.948	44	51.022		315	08.978		315.1496
OBS_WA_43	13.3224	44.8502	3276		13	19.345	44	51.014		315	08.986		315.1498
OBS_WA_44	13.2951	44.8502	3399		13	17.705	44	51.011		315	08.989		315.1498
OBS_WA_45	13.2592	44.8503	3513		13	15.554	44	51.016		315	08.984		315.1497
OBS_WA_46	13.4751	44.8104	3518		13	28.508	44	48.623		315	11.377		315.1896
OBS_WA_47	13.4303	44.8105	3496		13	25.815	44	48.627		315	11.373		315.1896
OBS_WA_48	13.3899	44.8101	3201		13	23.391	44	48.607		315	11.393		315.1899
OBS_WA_49	13.3493	44.8106	3077		13	20.957	44	48.637		315	11.363		315.1894
OBS_WA_50	13.2954	44.8106	3412		13	17.726	44	48.634		315	11.366		315.1894
OBS_MCS_51	13.3695	44.9175	2990		13	22.167	44	55.050		315	04.950		315.0825
OBS_MCS_52	13.3695	44.8985	3545		13	22.167	44	53.910		315	06.090		315.1015
OBS_MCS_53	13.3695	44.8798	3592		13	22.167	44	52.790		315	07.210		315.1202
OBS_MCS_54	13.3490	44.8673	3412		13	20.940	44	52.040		315	07.960		315.1327
OBS_MCS_55	13.3696	44.8543	3384		13	22.178	44	51.260		315	08.740		315.1457
OBS_MCS_56	13.3691	44.8306	3269		13	22.146	44	49.835		315	10.165		315.1694
OBS_MCS_57	13.3493	44.8305	3186		13	20.958	44	49.830		315	10.170		315.1695
OBS_MCS_58	13.3220	44.8305	3303		13	19.320	44	49.830		315	10.170		315.1695

Passive test II													
OBS_WA_E	13.5249	44.9266	2852		13	31.493	44	55.594		315	04.406		315.0734
OBS_WA_F	13.5247	44.8887	2939		13	31.480	44	53.324		315	06.676		315.1113
OBS_WA_59	13.5246	44.8107	3063		13	31.478	44	48.640		315	11.360		315.1893
OBS_WA_60	13.5245	45.0093	2398		13	31.470	45	00.560		314	59.440		314.9907
Profile R													
OBS_WA_61	13.2030	44.9702	2965		13	12.180	44	58.210		315	01.790		315.0298
OBS_WA_62	13.1288	44.9703	2867		13	07.730	44	58.220		315	01.780		315.0297
OBS_WA_63	13.0703	44.9702	2808		13	04.220	44	58.210		315	01.790		315.0298
OBS_WA_64	13.0123	44.9705	2575		13	00.740	44	58.230		315	01.770		315.0295
OBS_WA_65	12.9175	44.9703	3014		12	55.050	44	58.220		315	01.780		315.0297
OBS_WA_66	12.8412	44.9707	3154		12	50.470	44	58.240		315	01.760		315.0293
OBS_WA_67	12.7648	44.9705	3441		12	45.890	44	58.230		315	01.770		315.0295
OBS_WA_68	12.6972	44.9703	3712		12	41.830	44	58.220		315	01.780		315.0297
OBS_WA_69	12.5625	44.9703	3670		12	33.750	44	58.220		315	01.780		315.0297
OBS_WA_70	12.4858	44.9702	2938		12	29.150	44	58.210		315	01.790		315.0298

Appendix 3: Wide-angle profiles

Name	Order	Shooting direction	Profile Start (UTC) JD	Time	Profile End (UTC) JD	Time	Waypoint Number Start	End	Number of shots	Profile length (km)	Shot interval	Profile Start Lat (N)	Lon (W)	Profile End Lat (N)	Lon (W)
A	1	E → W	23	00:10	23	04:48	W1	W2	279	41.610	60	13.5653	44.7507	13.5650	45.1353
B	2	W → E	23	06:52	23	12:00	W3	W4	308	44.357	60	13.5244	45.1354	13.5242	44.7261
C	3	E → W	23	14:52	23	19:59	W5	W6	308	45.790	60	13.4751	44.6986	13.4751	45.1219
D	4	W → E	23	22:09	24	03:24	W7	W8	315	46.369	60	13.4301	45.1293	13.4297	44.7008
E	5	E → W	24	05:06	24	10:25	W9	W10	320	47.987	60	13.3896	44.6960	13.3897	45.1394
F	6	W → E	24	13:00	24	19:14	W11	W12	374	56.277	60	13.3495	45.2236	13.3491	44.7039
G	7	E → W	24	20:43	25	01:54	W13	W14	312	47.218	60	13.2946	44.6988	13.2954	45.1349
H	8	W → E	25	03:30	25	09:04	W15	W16	334	51.735	60	13.2597	45.1758	13.2590	44.6981
I	9	E → W	25	10:35	25	16:09	W17	W18	334	50.009	60	13.2226	44.6730	13.2232	45.1348
J	10	S → N	25	21:23	26	02:57	W19	W20	334	50.760	60	13.1718	45.0506	13.6299	45.0509
K	11	N → S	26	04:30	26	10:21	W21	W22	352	53.748	60	13.6431	45.0089	13.1580	45.0090
L	12	S → N	26	12:10	26	17:48	W23	W24	339	52.527	60	13.1546	44.9700	13.6286	44.9702
M	13	N → S	26	19:27	27	01:09	W25	W26	343	51.923	60	13.6309	44.9305	13.1622	44.9307
N	14	S → N	27	02:46	27	08:14	W27	W28	328	51.507	60	13.1641	44.8834	13.6290	44.8842
O	15	N → S	27	13:45	27	19:42	W29	W29	358	53.325	60	13.6478	44.8494	13.1665	44.8503
P	16	S → N	27	21:29	28	03:06	W31	W32	338	51.145	60	13.1679	44.8105	13.6295	44.8106
Q	17	N → S	28	05:02	28	10:34	W33	W34	332	51.074	60	13.6280	44.7680	13.1670	44.7689
R	18	S → N	46	10:37	47	13:47	W35	W36	1629	236.915	60	11.8493	45.2515	13.7788	44.9704
								TOTAL	7237	1084.275 km					

Appendix 4: MCS profiles

Profile name	Profile order	Shooting direction	Profile Start (UTC) JD	Profile Start (UTC) Time	Profile End (UTC) JD	Profile End (UTC) Time	Waypoint No. Start	Waypoint No. End	Number of shots	Length (km)	Shot interval (s)	First offset (m)	Depth (m) Guns	Depth (m) Streamer	Profile Start Lat (N)	Profile Start Lon (W)	Profile End Lat (N)	Profile End Lon (W)
L1.1	1	W → E	31	15:20	31	22:25	M1	M2	1276	64.55	20	145	8	10	13.5082	45.3340	13.5086	44.7381
L2.2	2	N → S	31	23:13	32	00:29	M3	M4	231	11.52	20	145	8	10	13.4682	44.6936	13.3656	44.6950
L3.1	3	E → W	32	01:01	32	05:54	M5	M6	875	44.64	20	145	8	10	13.3433	44.7291	13.3437	45.1410
L4.4	4	W → E	32	07:29	32	14:43	M7	M8	1299	64.77	20	145	8	10	13.4304	45.1318	13.4299	44.5343
L5.5	5	N → S	32	15:33	32	15:41	M9	M10	26	1.17	20	145	8	10	13.3771	44.4999	13.3665	44.5000
L6.6	6	E → W	32	16:30	33	01:21	M11	M12	1590	80.15	20	145	8	10	13.3193	44.5376	13.3222	45.2761
L7.7	7	W → E	33	03:08	33	09:41	M13	M14	1176	59.05	20	145	8	10	13.4099	45.2751	13.4100	44.7300
L8.8	8	N → S	33	10:31	33	11:09	M15	M16	113	5.63	20	145	8	10	13.3655	44.6911	13.3149	44.6919
L9.9	9	E → W	33	11:55	33	16:43	M17	M18	858	44.09	20	145	8	10	13.2760	44.7317	13.2775	45.1384
L10.10	10	W → E	33	21:41	34	04:56	M19	M20a	1302	65.78	20	145	8	10	13.3693	45.3342	13.3693	44.7274
L11.11	11	N → S	34	05:45	34	07:14	M21	M22	533	13.51	10	145	8	10	13.3272	44.6893	13.2063	44.6916
L12.12	12	E → W	34	08:01	34	09:48	M23	M24	641	16.38	10	145	8	10	13.1672	44.7338	13.1669	44.8847
L13.13	13	S → N	34	10:35	34	15:13	M25	M26	1667	42.70	10	145	8	10	13.2106	44.9225	13.5933	44.9079
L14.14	14	N → S	34	16:34	34	21:24	M27	M29	1737	43.37	10	145	8	10	13.5921	44.8304	13.2059	44.8584
L15.15	15	S → N	34	22:55	35	04:04	M30	M31	925	47.56	20	145	8	10	13.2039	44.9405	13.6307	44.9416
L14a.16	16	N → S	35	06:12	35	11:10	M27	M29	894	43.22	20	145	8	10	13.5911	44.8269	13.2053	44.8585
L15a.17	17	S → N	35	12:50	35	17:57	M30	M31	1825	47.01	10	145	8	8	13.2105	44.9424	13.6322	44.9418
L16.18	18	N → S	35	19:33	36	00:41	M32	M33	1841	47.10	10	145	8	10	13.6274	44.8598	13.2070	44.9004
L17.19	19	E → W	36	01:28	36	02:53	M34	M35	511	12.91	10	145	8	10	13.1668	44.9402	13.1665	45.0592
L18.20	20	S → N	36	03:47	36	05:31	M36	M37	625	15.82	10	145	8	10	13.2101	45.1081	13.3511	45.0999
L19.21	21	W → E	36	06:21	36	10:29	M38	M39	1484	35.55	10	145	8	10	13.3927	45.0589	13.3902	44.7314
L20.22	22	E → W	36	12:03	36	15:56	M40	M41	1397	35.27	10	145	8	10	13.3075	44.7348	13.3065	45.0601
L7a.23	23	W → E	36	17:49	36	21:54	M46	M47	1462	35.81	10	145	8	8	13.4075	45.0571	13.4093	44.7271
L23.24	24	N → S	36	22:38	36	23:47	M51	M52	413	10.37	10	145	8	10	13.3672	44.6922	13.2744	44.6915
L24.25	25	E → W	37	00:35	37	04:32	M53	M54	1415	35.35	10	145	8	10	13.237	44.7355	13.2367	45.0616
L6a.26	26	W → E	37	06:26	37	10:25	M49	M48	1434	35.49	10	145	8	8	13.3224	45.0570	13.3222	44.7297
R	27	S → N	46	11:01	47	13:47	WA-R2	WA-R1	1605	236.00	60	145	8	10	11.8570	45.2240	13.7788	44.9704

Appendix 5: Autosub dives

Dive	Start time[1]		End time[2]		Start position		Planned end		Actual end[2]		
	Date	Time	Date	Time	Lat (N)	Lon (W)	Lat (N)	Lon (W)	Lat (N)	Lon (W)	Prime objective
M103	19-Jan-16	20:33:14	20-Jan-16	19:48:58	13.3240	45.0580	13.3290	45.0580	N/A	N/A	Long EW magnetic lines across OCC
M104	21-Jan-16	15:40:56	22-Jan-16	14:32:06	13.4190	45.0300	13.4140	45.0300	13.4164	45.0367	Long EW magnetic lines across inter-OCC basin
M105	28-Jan-16	15:50:04	29-Jan-16	16:15:48	13.3580	44.7080	13.3850	44.7040	13.3801	44.7064	Pair of long magnetic lines between M103 and M104
M106	30-Jan-16	08:44:24	31-Jan-16	05:04:04	13.2935	44.7120	13.2820	45.0360	13.2883	45.0567	Long magnetic line + grid on SE apron of OCC
M107	06-Feb-16	20:02:38	07-Feb-16	18:29:46	13.3080	44.8670	13.3560	44.9270	13.3485	44.9312	EW grid over OCC dome for magnetics
M108	08-Feb-16	18:18:30	09-Feb-16	18:40:48	13.4390	44.9050	13.4340	44.9380	13.4301	44.9392	NNE-SSW bathymetry grid over inter-OCC basin & ridge
M109	10-Feb-16	16:03:10	11-Feb-16	15:24:32	13.3520	44.9150	13.3475	44.9250	13.3546	44.9195	NNE-SSW bathymetry grid over inter-OCC basin & ridge
M110	13-Feb-16	12:49:24	14-Feb-16	12:34:04	13.3600	44.9390	13.2980	44.9300	13.2952	44.9327	Bathymetric grid over top of OCC
M111	16-Feb-16	21:42:34	17-Feb-16	22:37:56	13.3280	44.8700	13.2870	44.8660	13.2874	44.8661	Bathymetric and magnetic grid on SE apron of OCC
M112	18-Feb-16	14:44:26	19-Feb-16	13:36:52	13.3560	44.9680	13.2860	44.9920	13.2887	45.0035	Bathymetric and magnetic grid on W flank of OCC

[1] Vehicle begins dive, UTC
[2]Return to sea surface, via USBL

Appendix 6: Gravity base ties

	Latitude, N (Deg)	(Min)	Longitude, W (Deg)	(Min)
Southampton, UK				
Absolute base station	50	53.5000	1	23.6000
Quayside *RRS Cook* – pre-cruise	50	53.8278	1	23.6908
Mindelo, Cape Verde				
Bollard 3, Porto Grande	16	53.385	24	59.962
Port of Spain, Trinidad				
Quayside *RRS James Cook* - between bollard 37 and 38	10	39.1610	61	31.2780
SE corner customs warehouse – relative station, JC102 & JC109	10	39.1500	61	31.2800
Absolute base station	10	39.1362	61	31.0080

Appendix 7: Sound velocity profiles and acoustic tests

JD	Depth (m)	Latitude, N (Deg)	(Min)	Longitude, W (Deg)	(Min)
15	1000	16	17.492	29	14.538
19	1000	13	25.800	44	52.799
42	4000	13	15.000	44	53.600

Appendix 8: Personnel

The *RRS James Cook* carried a total crew of 52 people for cruise JC132 as named below:

Master	James Gwinnell
Chief Officer	Philip Gauld
2nd Officer	Malcolm Graves
3rd Officer	Declan Morrow
Chief Engineer	Robert Inglis
2nd Engineer	Michael Murray
3rd Engineer	Angus Hamilton
3rd Engineer	Michael Murren
ETO	Martin Ulbrecht
ERPO	Brian Conteh
CPO (Science)	Martin Harrison
CPO (Deck)	Philip Allison
PO (Deck)	David Price
Seaman	Steve Day
Seaman	Brian Burton
Seaman	Andrew Dwyer
Seaman	Scott Aspland
Purser	Michael Ripper
Head Chef	Darren Caines
Chef	Christopher Keithley
Steward	Kevin Mason
Assistant Steward	Thomas Docherty
Cadet	Robert Hoyland
Cadet	Christina Coates
Principal Scientist	Tim Reston
Co-chief Scientist	Christine Peirce
Scientist	Roger Searle
Scientist	Matthew Funnell
Scientist	Adam Robinson
Scientist	Nuno Mendez Simao
Scientist	Matthew Falder
Scientist	Murray Hoggett
Scientist	Gael Lymer
Scientist	Geraud Vilaseca
Teacher-at-sea	Angela Bentley
OBS Technical Support (Lead)	Ben Pitcairn
OBS Technical Support	Andrew Clegg
MMO (Lead)	Anna Bird
Technical Liaison Officer	Andrew Henson
Ship systems (Lead)	Mark Maltby
Ship systems	Juan Ward
Autosub (Lead)	James Burris
Autosub	James Perrett
Autosub	Rachel Marlow
Autosub	David Paxton
Seismics (Lead)	Jason Scott
Seismics	Will Richardson
Seismics	Andrew Leadbeater
Seismics	Ian Murdoch
Seismics	Dean Cheeseman
Contractor – Exploration Electronics Ltd	Stefan Paterson
Contractor – Exploration Electronics Ltd	Martin Weeks

Appendix 9: Project 13N Principal Scientists, Project Partners and Consultants

The Principal Scientists, Project Partners and Consultants for the 13N MAR project are:

Principal Scientists:	Professor Tim Reston (Birmingham University) Professor Christine Peirce (Durham University) Professor Chris MacLeod (Cardiff University)
Project Partners:	Dr Robert Sohn (Woods Hole Oceanographic Institution) Dr Juan Pablo Canales (Woods Hole Oceanographic Institution) Dr Javier Escartin (Institute de Physique de Globe, Paris)
Consultants:	Professor Roger Searle (Emeritus, Durham University) Professor Joe Cann (Emeritus, Leeds University)